Connecting Topology, Mechanical Behavior, and Hydrogen Interaction Dynamics in Nanoporous Nb and Pd

Vom Promotionsausschuss der
Technischen Universität Hamburg

zur Erlangung des akademischen Grades

Doktor-Ingenieurin (Dr.-Ing.)

genehmigte Dissertation (Monografie)

von

Seoyun Sohn

aus

Daejeon, Republik Korea

2025

Erstgutachter: Prof. Dr.-Ing. Jörg Weissmüller

Zweitgutachter: Prof. Dr.-Ing. habil. Thomas Klassen

Vorsitzender: Prof. Dr. sc. nat. Franziska Lissel

Tag der mündlichen Prüfung: August 22, 2025

Acknowledgments

First and foremost, I would like to express my sincere gratitude to my supervisor, Prof. Jörg Weißmüller, for giving me the opportunity to work on this topic and for his invaluable guidance, encouragement, and patience throughout the course of my doctoral research. His expertise and support have been a constant source of inspiration.

I am deeply grateful to Dr. Jürgen Markmann for his support, ranging from help with lab facilities to insightful scientific guidance, both of which were indispensable throughout my research journey.

I would also like to thank my second reviewer, Prof. Thomas Klassen, for taking the time to carefully evaluate my work and for providing constructive feedback. My sincere thanks also go to Prof. Franziska Lissel, whose leadership and perspective broadened my understanding of the field.

Special thanks are due to Prof. Shan Shi, who warmly welcomed me and offered guidance from the very first day I arrived here. I am also thankful to Prof. Norbert Huber, with whom I had the privilege of collaborating on a fascinating research topic and who guided the team as the leader of the institute. This collaboration was not only a valuable learning experience but also an important milestone in my doctoral studies.

I would like to extend my heartfelt appreciation to Haide Alfort-Springer, Stephanie Kropf-Eilers, and Sabine Schrader, whose administrative support and assistance were essential in many organizational aspects of my doctoral work.

To my colleagues with whom I had the pleasure of working over the past few years–including Olga Matts, Dr. Stefan Berger, Dr. Nadiia Mameka, Lukas Riedel, Zhongyang Li, Dr. Marine Bossert, Dr. Yong Li, Dr. Xinyan Wu, and Dr. Claudia Richert–I am deeply thankful for their companionship, expertise, and generous assistance. I truly appreciate not only our insightful discussions but also the daily conversations which brightened my days and kept me motivated. I would also like to thank all my team members at Helmholtz-Zentrum Hereon and Technische Universität Hamburg for their support and the positive working atmosphere, which made the challenging moments more manageable and the successes more rewarding.

Finally, I am profoundly grateful to my family and my fiancé for their unconditional love, understanding, and encouragement. Their support has been my greatest source of strength, and I could not have reached this point without them.

The financial support from the Deutsche Forschungsgemeinschaft (DFG, German Research Foundation) through the Collaborative Research Initiative SFB 986 "Tailor-Made Multi-Scale Materials Systems: M3" (Project No. 192346071) is greatly acknowledged.

Abstract

Studying the mechanical performance of nano- and microscale porous materials enhances our understanding of small-scale solids and improves materials design for functional applications. This study investigates the microstructure and mechanical behavior of millimeter-sized samples with a nanoscale random network structure, integrating metal hydrides to expand their functionality. Notably, metals such as Nb and Pd can form solid solutions with hydrogen across a broad concentration range at relatively low temperatures. Therefore, nanoporous (np) Nb and np Pd, representing body-centered cubic (BCC) and face-centered cubic (FCC) crystal structures respectively, are fabricated and studied, with np Au serving as a benchmark.

In the first part of the thesis, the mechanical behavior of np material is investigated with a focus on the role of its microstructure size and topology. Results from macro-compression tests and X-ray nanotomography of np Nb confirm that coarsening degrades yield strength and that its Young's modulus deviates from scaling laws developed for np Au, a widely-investigated model system produced via aqueous dealloying. The scaled genus, a measure of the network's connectivity, of np Nb is lower than that reported for np Au, and this reduced connectivity provides an obvious explanation for the low modulus. From these observations, a novel scaling law that explicitly involves the scaled genus is established. Furthermore, the comparison between np Au and np Nb implies that structural dispersion should be acknowledged as an additional structural descriptor to draw an analogy between liquid-metal dealloyed and electrochemically dealloyed materials.

The second part of the thesis focuses on the interaction dynamics between np Pd and hydrogen. Compared to np Nb, np Pd demonstrates significantly higher hydrogen absorption efficiency. The study aims to understand the role of geometry on the hydrogen charging kinetics by tuning the ligament size of np Pd and to understand the limiting subprocess. Hydrogen ad/absorption and desorption kinetics are analyzed using electrochemical impedance spectroscopy and potential jump tests. The results suggest that the interfacial injection of hydrogen is the controlling factor of the sorption rate. This injection process is analyzed from a thermodynamic perspective, with the Pd-H miscibility gap taken into account. The Butler-Volmer equation is adapted to model the injection rate consistent with the equation of state for the composition-dependent chemical potential at equilibrium in an interacting solid solution. The model successfully predicts the characteristic charging time observed in the np Pd-H system.

Overall, this thesis establishes a coupled relationship between mechanics, microstructure, and hydrogen absorption kinetics, providing insights into the optimization of structural design in np materials, thereby paving the way for their applications as integrated material systems.

Contents

List of Figures

List of Tables

Chapter 1

Introduction

1.1 Network nanomaterials

Materials with random network microstructures appear in a variety of forms across different systems. In biological contexts, they form the cytoskeleton of cells and collagen in connective tissue. In non-living systems, these structures can exist as molecular-scale scaffolds, as in rubber or gels, and can also scale up to micron or millimeter-sized structures, such as those in polymer products and low-density metallic open-cell foams [1–4]. Often, one of their key functions is to bear the load. In this respect, network nanomaterials are attractive, since the strengthening that comes with reducing the size of the network struts may partly compensate for the weakening due to the low solid fraction [5–9]. Interpolation of the experimentally measured yield strength in Fig. 1.1 suggests that reducing the diameter of network struts to approximately 10 nm could allow the material to achieve its theoretical strength [10, 11]. Thus, network nanomaterials may combine high mass-specific strength or stiffness with low density [9, 12–15]. Ordered network nanomaterials can be made in the form of 3D manufactured periodic lattices with unit cells engineered for optimum performance [9, 12–14]. Cellular materials can also be designed as shell structures with exceptionally low density, where the load-bearing function is concentrated to the interfacial region between two void phases [16–18]. Yet, nanoscale structuring also brings a dramatic increase in the number of structural elements per volume, favoring preparation by nature's self-organization processes over controlled 3D manufacturing [15]. Then the microstructure typically remains random, as in the wider class of materials addressed at the outset.

A conventional approach to fabricating random network nanomaterial is through chemical or electrochemical dealloying. Here, the atoms in the alloy are selectively etched and reorganized, driven by differences in standard electrode potentials or an external electrochemical potential in an aqueous environment (See Sec. 2.1.1 for more details). During the dealloying process, interfacial instabilities may arise as the components migrate along the metal–liquid interface [19]. Rather than maintaining a planar interface, the mobile atoms reorganize into a three-dimensionally complex morphology. This leads to the formation of an open, porous structure with characteristic feature sizes in the nanometer range. This pattern formation process is schematiaclly illustrated in Fig. 1.2.

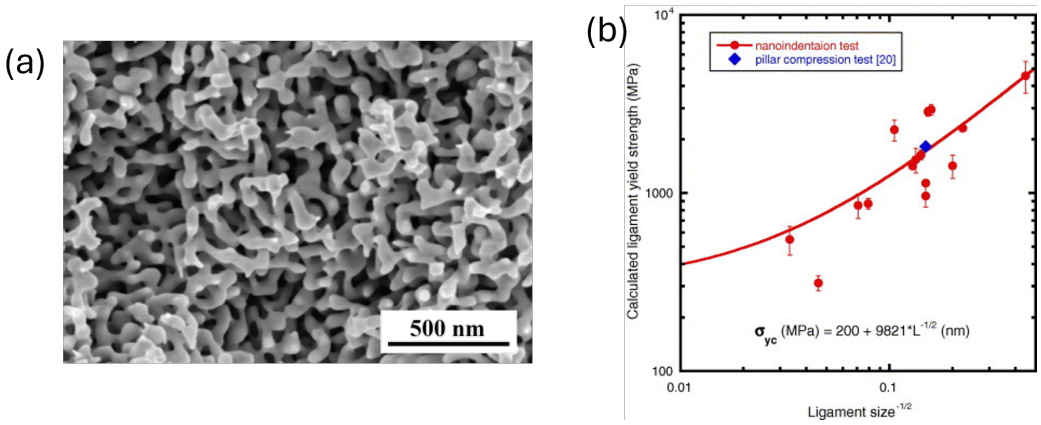

Figure 1.1: (a) A typical SEM micrograph of nanoporous Au produced through electrochemical dealloying. Adapted from [10] with permission. (b) Ligament yield stress of nanoporous gold foams plotted against the inverse square root of ligament size. The solid line represents the fit to the data (red circles) based on the equation displayed in the plot. Adapted from [11].

Nanoporous gold (np Au) [20] is a standard example of a network nanomaterial that can be reliably produced via aqueous dealloying. The microstructure of np Au is well represented [21] by the leveled-wave model [22], which also underlies the random microstructures of a wider range of materials, including spinodally decomposed solid solutions, porous glasses such as vycor, as well as some microemulsions and polymer blends [23–28]. Uniform macroscopic bodies of np Au then can be mechanically tested with reliable macroscale schemes [29–33]. This qualifies np Au as a model material for nanoscale random networks in general, and specifically for studies of their mechanics. This thesis will begin with a discussion of np Au and will extend the elemental choice of network nanomaterials for their mechanical stiffness, cost-efficiency, and functionalization. Detailed research objectives are provided in the following section.

1.2 Motivation and research objectives

Studying the mechanical performance of nano- and microscale porous materials allows us to understand small-scale solids and to enhance their materials design for functional applications [35]. Nanoporous materials with a bicontinuous network structure have previously shown potential as light-weight structural materials [36], catalysts [37, 38], actuators [39–41], semiconductor interconnects [42] and sensors [43–46]; they have demonstrated recoverable tuning of mechanical properties [47] and even enhanced radiation resistance [48]. As load-bearing capability is typically a prerequisite for operation as a functional material, the mechanical behavior of nano- and microporous metals have been intensely investigated, using testing schemes both at the macro- [33, 49–53] and at the microscale [54–58].

As outlined above, np Au has been the most widely investigated model material for nanoporous materials. Understanding the mechanics of np Au, as a standard model of random networks, requires the relevant statistical microstructure parameters to be identified and their impact on the mechanics analyzed. During the past decade, ex-

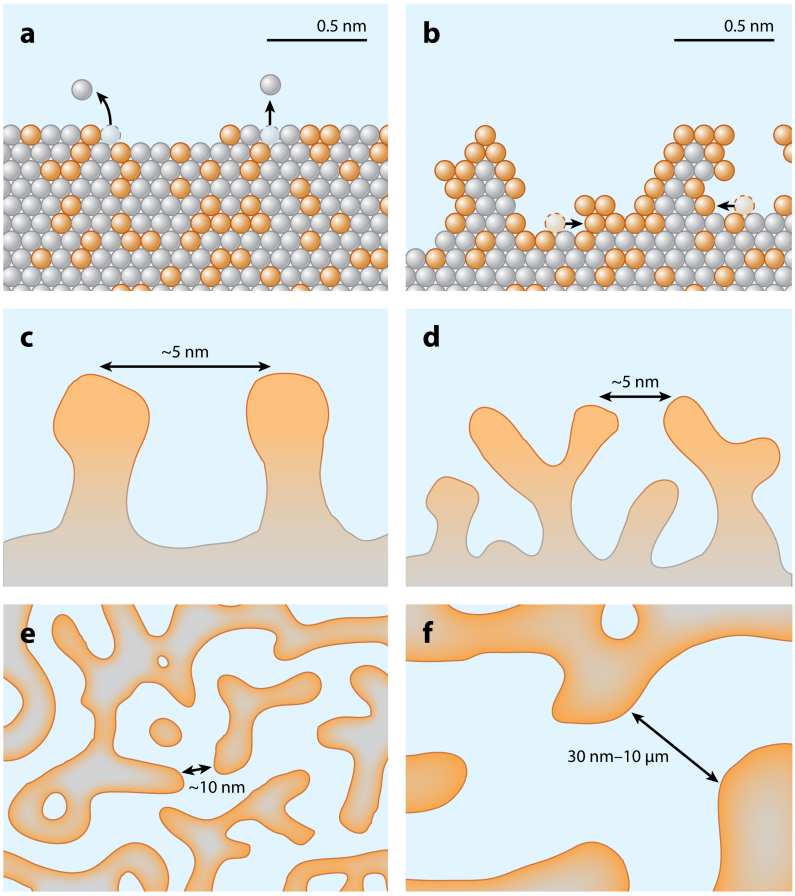

Figure 1.2: A working model illustrating the porosity evolution during dealloying of the Ag (gray)-Au (orange) alloy system. (a) Dissolution of Ag and (b) surface diffusion of Au atoms. (c), (d) Undercutting and bifurcation of ligaments as Au atoms become insufficient to totally passivate the increasing surface area. (e) A bicontinuous porous structure formed as a result of dealloying. (f) A coarsened structure with an increased length scale compared to (e). Adapted from [34].

periments have established a consistent picture of np Au's mechanical behavior [8]. There, microstructural metrics, such as solid volume fraction (or, in other words, relative density), and ligament size, are frequently highlighted as the primary factors influencing the material's stiffness, yield strength, and deformation behavior. The solid volume fraction has been a central parameter in related predictive theory [59] for the mechanics of crystalline networks as well as in the context of np Au [60, 61]. In addition, recent research advertises network connectivity as an additional microstructural metric controlling the mechanics of np Au [32, 62–66]. Yet, the scaling between the effective Young's modulus, E_{eff}, as an elementary mechanical materials parameter and the connectivity in random network materials remains to be established. In the first part of the thesis, the aforementioned connection is explored, the observations are condensed into a novel scaling law. This part exploits existing experimental and simulation database on E_{eff} of the random network material. It adds novel simulation data for leveled-wave-like random networks with different connectivity.

As represented by np Au, most studies on nanoporous materials so far have been

confined to noble metals such as gold [20, 49], silver [67, 68], palladium [39, 40], or platinum [69], since their high electronegativity facilitates preparation by (electro)chemical dealloying in aqueous media. By contrast, liquid metal dealloying (LMD) relies on differences in enthalpy of mixing for dissolution selectivity [70, 71], thereby expanding the scope of elements to nearly the entire periodic table [19]. Over the last decade, porous materials composed of less-costly materials such as Ti [72] and its alloys [73], FeCr [74, 75], Nb [76], stainless steel [77], and high-entropy alloys [78] have been fabricated via LMD. Explanatory approaches to the mechanical behavior of LMD-fabricated metals have invoked similar concepts as those fabricated by aqueous dealloying. For instance, strength and elasticity relations of LMD-made porous FeCr are well compatible with the modified form of the Gibson-Ashby scaling equations [74], which also provide a basis for the mechanics of electrochemically dealloyed np Au [62]. However, it remains to be explored how details of the microstructural morphology or topology of LMD porous solids connect to their mechanical properties.

This issue is addressed experimentally in the section following the scaling of np Au. Nanoporous niobium (np Nb) is created through LMD, and using that, the mechanical properties are studied in relation to ligament size, solid fraction, and specifically its three dimensional microstructure information. It is observed that the elastic behavior of np Nb differs significantly from that of electrochemically dealloyed np Au, the benchmark for (electro)chemically dealloyed nanoporous metals. In connection with the outcome of the previous part, this discrepancy is attributed to structural connectivity. The notable contrasts between the structures of LMD-produced np Nb and electrochemically dealloyed np Au will be discussed.

Finally, the thesis extends the investigation of structural properties–particularly ligament size–to the hydrogen-involved functionalizaion of nanoporous materials. Not only have nanoporous metals proved their potential application on the hydrogen sorption actuator [40], they also offer an ideal platform for investigating the hydrogen–metal interactions in the near-surface region, as their nanoscale structure reduces the diffusion path of hydrogen and accentuates near-surface phenomena. However, little kinetic information is currently available on these interactions, which are essential for improving hydrogen uptake and release efficiency. To address this gap, the hydrogen sorption kinetics of nanoporous materials is explored in the context of optimizing hydrogen sorption rates.

Given the interstitial nature of hydrogen, Nb and Pd are first considered as representative elements of body centered cubic (BCC) and face centered cubic (FCC) crystal structures, respectively, both of which can form continuous solid solutions or hydride phases. They also have relatively high hydrogen sorption capacities of maximum H/M $\approx$ 0.7 for Pd and $\approx$ 0.4 for Nb near room temperature [79, 80], where H and M are the number of hydrogen atoms and metal atoms, respectively. Due to the hydrogen barrier created by the Nb oxide layer, however, the focus of this part shifts to np Pd-H system. Using np Pd as a model material, the objective is to optimize its microstruture size for applications in porous metal hydrides as integrated nanoporous material systems. The hydrogen charging dynamics are broken down into subprocesses occurring at each interface, and the characteristic time scales are estimated to identify the rate-limiting mechanism governing the hydrogen uptake rate. The kinetics of this limiting mechanism is then theoretically characterized. This in turn enables the prediction of

the hydrogen sorption rate of nanoporous metal, including the response time of np Pd-H-based actuators [40].

1.3 Outline of thesis

The thesis is structured as follows:

Chapter 2 provides the theoretical background necessary for interpreting the results of this thesis. It covers the fundamental physics of the dealloying process, as well as the structural and mechanical properties of nanoporous materials. The chapter concludes with the hydrogen electrosorption process in Pd, which serves as a model system to extend the functionality of nanoporous materials to hydrogenated porous structures.

Chapter 3 gives the details of the experimental procedures, including the material preparation and characterization techniques used in this study.

In Chapter 4, the results are presented, beginning with the new scaling relation between structural and mechanical properties of np Au. This is established based on the existing database and will serve as a guideline for the subsequent sections. The chapter then details the experimental results. It reports the synthesis of np Nb and the modulation of its microstructure sizes. Its mechanical properties under compression and structural connectivity are presented.

Afterwards, np Nb proved unsuitable for hydrogen insertion, thereby the focus moves to np Pd, where its hydrogen actuation properties are examined. Observations include hydrogen solubility and actuation response over time. The charging process is further examined using impedance spectroscopy, and basic elemental fitting is provided.

Chapter 5 presents an analysis and discussion of the results. The physical significance of the new scaling law is explored, followed by an evaluation of the experimental findings for np Nb in relation to this scaling law. The relevance of the scaling relation to liquid metal dealloying is assessed. This chapter continues by discussing the subprocesses involved in hydrogen actuation of np Pd, with particular attention to its microstructural features, specifically ligament size. It concludes by identifying the rate-limiting subprocess and examining it in the context of the miscibility gap in metal hydride systems.

Finally, Chapter 6 summarizes the findings of the thesis, providing general conclusions and perspectives for future research.

This thesis incorporates and expands upon the publications listed below.

- Sohn, S.; Richert, C.; Shi, S.; Weissmüller, J.; Huber, N. *Scaling between elasticity and topological genus for random network nanomaterials. Extreme Mechanics Letters* **2024**, *68*, 102147.

- Sohn, S.; Shi, S.; Markmann, J.; Berger, S. A.; Weissmüller, J. *Compressive behavior and connecting topology of monolithic nanoporous niobium. Materials Research Letters* **2024**, *1*, 1–10.

Chapter 2

Theoretical background

2.1 Synthesis of network nanomaterials by dealloying

Dealloying is a metallurgical process that involves the selective removal of one or more elements from an alloy, resulting in a bicontinuous network structure composed of the remaining element(s) [81]. It relies on the principle that different elements in an alloy have varying tendencies to dissolve when exposed to a certain environment. The dealloying process has evolved over the past few decades from being restricted to (electro)chemical corrosion to include liquid-mediated dissolution in general [71]. Categorized by their dissolution mechanisms, electrochemical dealloying (ECD) and liquid metal dealloying (LMD) are widely used techniques for fabricating nanoporous metals at a macroscale.

2.1.1 Electrochemical dealloying

Electrochemical dealloying, or aqueous dealloying, is a process where selective dissolution of one or more elements from an alloy occurs in an electrochemical environment, typically by applying an electric potential in an electrolyte. The selectivity stems from the differences in standard reduction potentials between the elements involved. The element with the lower standard potential undergoes corrosion, resulting in the formation of a porous structure composed of the more noble element. For example, in the commonly used Ag-Au alloy system, Ag is the less noble element that oxidizes and enters the acidic electrolyte as ions. The remaining more noble constituent, Au, remains and rearranges to form a bicontinuous porous structure with nanoscale ligaments and pores. A typical microstructure of electrochemically dealloyed Au alongside an optical image of a macroscopic sample are shown in Fig. 2.1.

During electrochemical dealloying, structure formation is driven by a kinetic competition between dissolution of the more active component and interface diffusion of the remaining atoms [83]. Initially, dealloying begins with preferential surface dissolution that progresses perpendicular to the surface, leading to surface roughening. The remaining component then reorganizes through diffusional kinetics, causing the clustering of atoms, which inhibits passivation and continuously exposes fresh surfaces to further dissolution, thus increasing the overall surface area [19, 84]. Simultaneously, surface diffusion driven by capillary energy promotes the coarsening of ligaments by

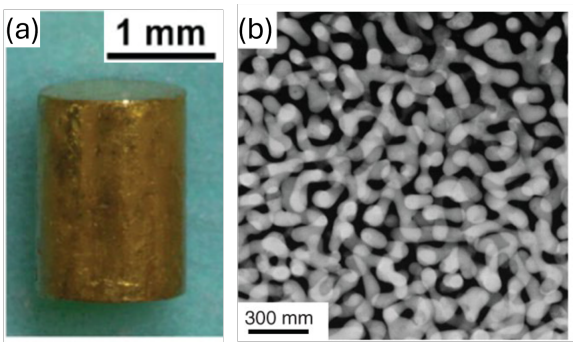

Figure 2.1: Images of a nanoporous gold fabricated by electrochemical dealloying. (a) Photograph of the sample. (b) Scanning electron microscopy image of the microstructure. Adpated from [82].

transporting atoms from regions of high positive surface curvature to regions of high negative curvature [19]. The final pore and ligament sizes are strongly influenced by factors such as the initial alloy composition, the choice of electrolyte, the applied potential, and the temperature.

Nanoporous metals produced via ECD typically exhibit ligament sizes ranging from 5 nm to over 500 nm upon thermal coarsening [85, 86]. This results in a high specific surface area, with reported values ranging from ≈ 2 to $7\,\mathrm{m^2/g}$ [87, 88], equivalent to about 4×10^4 to $1.4 \times 10^5\,\mathrm{mm^{-1}}$, qualifying them as ideal for various applications such as catalysis, chemical sensing, and energy storage. Their functional properties can be further optimized through nanocoating of the surface, or by creating bicontinuous composite materials through liquid infiltration into the nanoporous structure [89–94].

2.1.2 Liquid metal dealloying

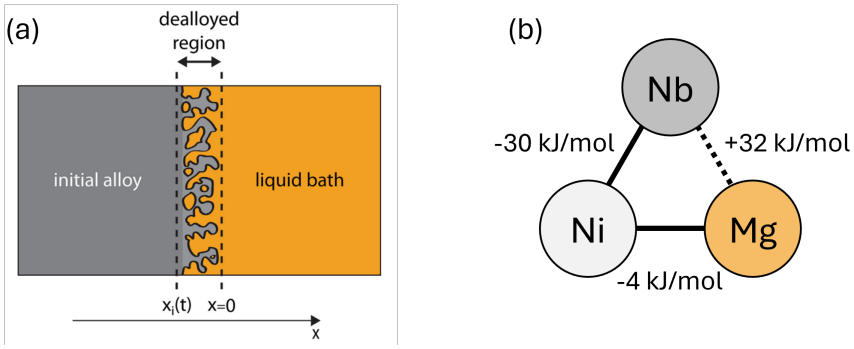

Figure 2.2: (a) Schematic of the interface between liquid and solid phases during liquid metal dealloying, Adapted from [95]. Initially at $x = 0$, the interface moves to $x_i(t)$ at time $t > 0$. (b) Example of a liquid metal dealloying atomic triplet, showing binary mixing enthalpies [96] for each atomic pair. Mg mixes with Ni but not with Nb, resulting in porous Nb from a Nb-Ni alloy. Solid and dotted lines indicate negative and positive mixing enthalpies, respectively.

The selective removal of elements during LMD is driven by miscibility relationships between the constituent elements. The repulsive or attractive force between

the elements creates dissolution selectivity, thus expanding the scope of materials beyond noble metals [70, 71]. Unlike conventional electrochemical dealloying, which uses an aqueous solution as the medium, LMD utilizes a molten metal as the dealloying medium. Figure 2.2(a) shows the schematic of the pore formation process at the interface between the liquid and solid metals. The structure formation mechanism of ECD–a balance between dissolution and interface diffusion–is applicable to LMD likewise.

LMD is not limited to noble elements, letting it to be a more viable alternative than ECD for producing cost-effective porous metals. Over the past decade, it has gained increasing attention due to its potential in a wide range of applications, particularly in energy storage [97] and biomedical fields [73]. For instance, porous Nb [97] can be fabricated by removing Ni from a Nb-Ni alloy in a molten Mg bath. The binary mixing enthalpies for each atomic pair involved are illustrated in Fig. 2.2(b). In contrast to the positive mixing enthalpy between Nb and Mg, the negative mixing enthalpy between Mg and Ni indicates that Ni can be selectively dissolved in Mg. The system has been the subject of several studies, particularly for possible application in supercapacitors [76, 97, 98].

2.2 Structural properties of nanoporous materials

2.2.1 Leveled-wave model for nanoporous gold

The leveled-wave configuration, as proposed by Soyarslan et al., effectively represents the random network microstructures [22, 66]. These structures include not only nanoporous metals produced by electrochemical corrosion [21], but also a broader spectrum of materials such as spinodally decomposed solid solutions, porous glasses like vycor, as well as various microemulsions and polymer blends [23–28].

The model is based on the approximation [22] that the composition field in the early stages of spinodal decompsition–diffusive spontaneous decomposition of thermodynamically unstable binary solutions–could be approximated by the superposition of plane waves of random wave vector orientation and with random phase shifts but with identical wavelength. A stochastic bicontinuous microstructure is then generated by applying a level-cut for binarizing with the required solid fraction, φ [22]. Figure 2.3 illustrates examples of microstructures with solid volume fractions ranging from 0.1 to 0.5. The leveled-wave model demonstrates a percolation-to-cluster transition at the solid fraction threshold $\varphi_{\mathrm{p}} \approx 0.159$ [66]. The microstructure in Fig. 2.3(a) shows this transition, where a solid fraction of 0.1 results in many disjoint regions.

As leveled-wave structures of different wavelengths are self-similar, the model has φ as the only determining parameter for its morphology. This suggests that the connectivity is dependent solely on φ and influenced strongly by that parameter. In typical experimental cases, φ is well measurable, and that parameter serves the microstructure variable in scaling laws. Consequently, the comparison between leveled-wave microstructures and experimental data involves no free parameters. It is therefore remarkable that the model's stiffness and strength closely align with experimental results for as-prepared np Au [36, 66].

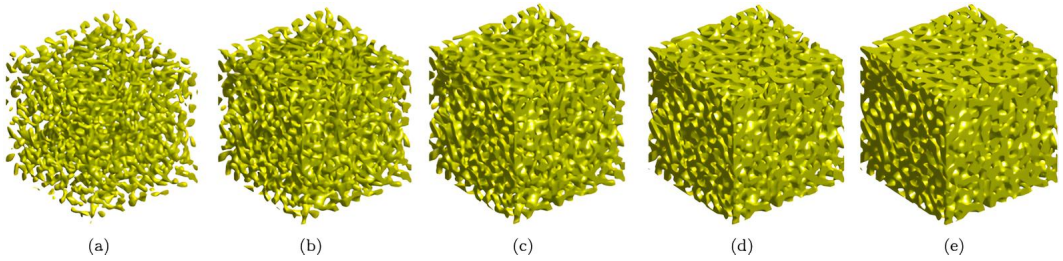

Figure 2.3: Examples of microstructures generated by leveled-wave approach. The volume size is 12 wavelengths and the solid fractions are (a) 0.10, (b) 0.20, (c) 0.30, (d) 0.40, and (e) 0.50. Adapted from [66].

2.2.2 Reaction kinetics and morphological evolution during liquid metal dealloying

During LMD, the reaction kinetics are governed by the surface diffusion of the dissolving element away from the dealloying interface. The speed of the dealloying front is controlled by the flux of the dealloyed element towards the liquid metal, which determines the dealloying depth, $x_i(t)$, at a given time t [95]. This relationship can be described by

$$x_i(t) = \sqrt{4pDt}\,, \tag{2.1}$$

where D is the diffusivity of the dissolving element in the liquid phase, and p is the dimensionless Péclet number. It has been observed that grain boundaries may dissolve first during LMD, and impede diffusion from the dealloying interface [95]. This suggests that grain size can also influence the global dealloying kinetics especially when the sample reaches a macroscale.

Simultaneously, interfacial diffusion promotes coarsening during dealloying, contributing to the evolution of topologically connected structures [100, 101]. The characteristic length scale, L, which in turn represents the ligament size, can be expressed as

$$L^m = ktD\,, \tag{2.2}$$

where k is a constant and m is the coarsening component typically ~ 4 for surface diffusion, as previously observed by [97]. This indicates that ligament size can be controlled by adjusting dealloying parameters such as dealloying time and temperature. Additionally, the choice of molten metal can influence the structure size by varying the temperature, directly affecting diffusion rates [102]. Suppressing surface diffusion is possible by adding components to the liquid bath. For instance, Ag and Bi in molten Cu [95] or Ce in molten Mg [76] have been shown to lower the melting points of the liquid bath and effectively limit the size of ligaments by restricting the diffusion of the dealloyed element.

While both dealloying techniques, electrochemical and liquid-metal dealloying, rely on similar microstructural evolution processes (See Sec. 2.1), structural differences in the product material have been noticed. Numerical simulation [19, 95, 99] and experimental 3D characterization have studied the morphological and chemical evolution [77, 103] during LMD. The most notable difference is the coarser microstructures generated by LMD. Furthermore, LMD features elongated ligaments at the dealloying front,

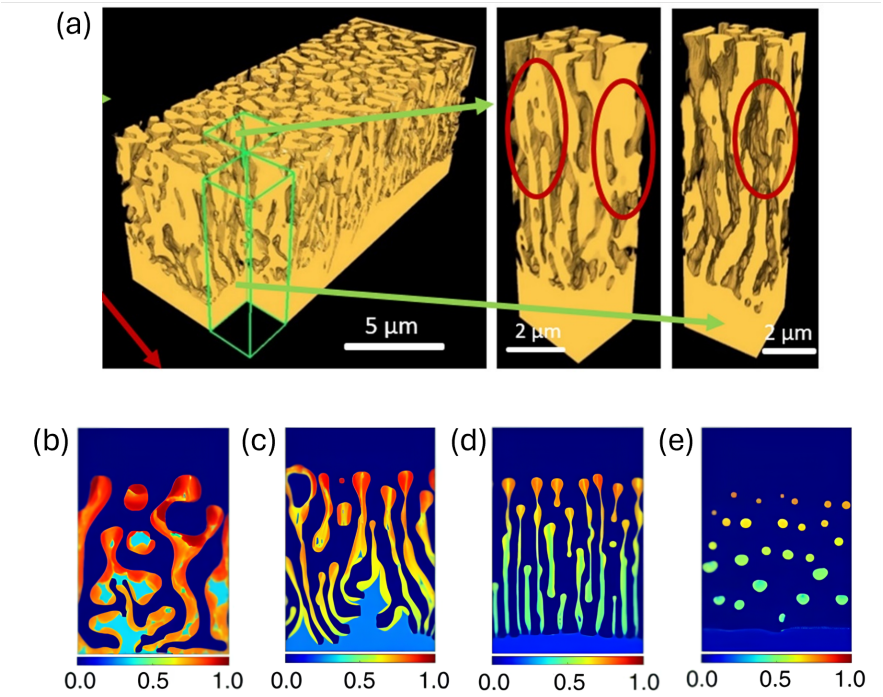

Figure 2.4: (a) X-ray nanotomography reconstruction of nanoporous stainless steel produced by liquid metal dealloying, showing elongated ligaments. Adapted from [77]. (b-e) Phase-field simulations showing morphology variations formed by liquid metal dealloying of an $A_{c_0}B_{1-c_0}$ alloy at different initial concentrations: (b) $c_0 = 35\%$, (c) $c_0 = 25\%$, (d) $c_0 = 15\%$, (e) $c_0 = 5\%$. Adapted from [99].

as shown in Fig. 2.4(a), a phenomenon not previously observed in aqueous dealloying [77]. Figure 2.4(b-e) presents a phase-field simulation illustrating the rich morphological variations created by LMD by varying the initial alloy composition. Notably, the filamentary structure and dispersed blobs shown in Fig. 2.4(d) and (e) do not have a direct analogue in electrochemical dealloying [99].

2.3 Mechanical properties of nanoporous materials

2.3.1 Gibson-Ashby law: a scaling relation for the Young's modulus of constant-connectivity network structures

For many classes of materials characterized by network-like microstructures, the solid fraction φ is adjustable while keeping the connectivity of the underlying skeleton unchanged. At small φ (typically <0.1), the Young's modulus, E_{eff}, of the structured material are related to φ, which follow the Gibson-Ashby scaling law [59, 105]

$$E_{\text{eff}} = \varphi^2 E_0 \,, \tag{2.3}$$

where E_0 is the Young's modulus of the cell-wall material, i.e., the base material.

The Gibson-Ashby law of Eq. 2.3 has been derived for a three-dimensional periodic lattice of unit cells consisting of struts connected in nodes (Fig. 2.5(a)). The solid

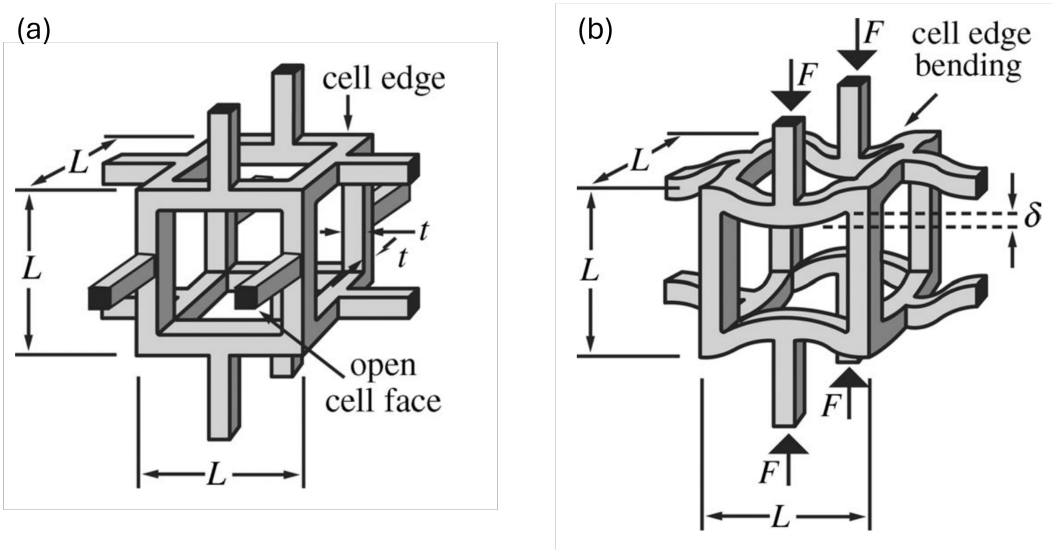

Figure 2.5: (a) An idealized unit cell in an open-cell foam structure. (b) The loaded cell, illustrating bending of the struts. Figures adapted from [104].

fraction, φ, of the model structure is a central parameter and is varied by changing the strut aspect ratio while maintaining the architecture and specifically the connection between the struts invariant. The struts are then assumed to be thin enough so that they are bent linear-elastically under compression. Figure 2.5(b) illustrates bending of the struts of the structure under load. This scheme is valid until the applied force reaches the collapse load, at which point the cell walls undergo plastic bending or elastic buckling [104].

In such a configuration, dimensional analysis is applied to obtain Eq. 2.3. For a cubic array of members with length L, and square cross-sections of side t, the relative density of the cell, i.e. the solid fraction φ is given by

$$\varphi \propto (t/L)^2 \,. \tag{2.4}$$

The second moment of area, I, of the cell edge of square cross-section t^2 is also related to the beam dimensions by [106]

$$I \propto t^4 \,. \tag{2.5}$$

Under linear-elastic conditions, the displacement of a beam of length L loaded at its midpoint with a force F is proportional to $FL^3/E_0 I$ [106]. Likewise, in a cellular material subjected to uniaxial stress, where each cell wall transmits a force F, the cell members undergo bending. The linear-elastic displacement of the entire structure follows the same proportionality, expressed as $FL^3/E_0 I$. The overall stress is F/L^2 by definition, while the strain is given by δ/L, where δ is the displacement. Consequently, the E_{eff} of the foam, defined as stress divided by strain, yields $E_{\text{eff}}/E_0 \propto \varphi^2$. This result returns to Eq. 2.3.

Although some observations of dealloying-made np Au are partly compatible with the predictions of Eq. 2.3, the general applicability of the scaling law to nanoporous structures remains debated. Fig. 2.6 demonstrates a systematic deviation for as-prepared np Au [8, 32, 52, 62, 107, 108]. Experimental data consistently show that np

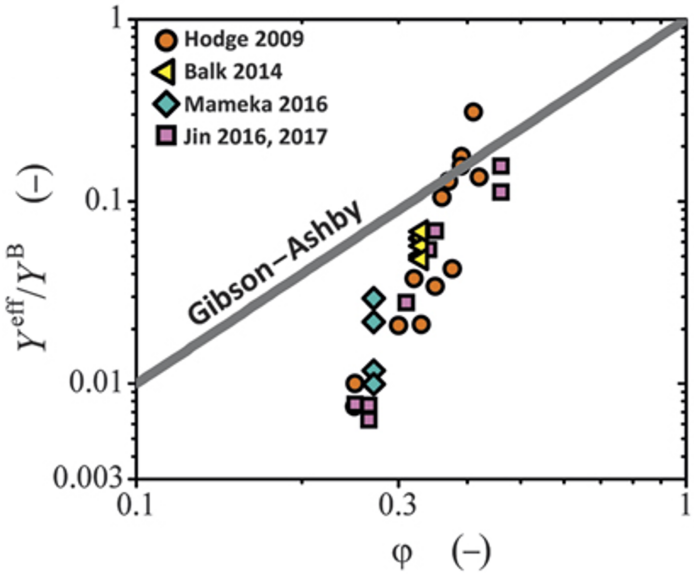

Figure 2.6: Effective Young's modulus, Y^{eff}, of macroscopic, as-prepared nanoporous Au normalized to the Young's modulus of massive Au, Y^{B}, versus solid volume fraction, φ, reported in [32, 52, 62, 107, 108]. Figure adapted from [8].

Au is generally more compliant–often more than an order of magnitude when $\varphi \lesssim 0.3$–than the model predicts. Molecular dynamics simulation by [109] also report anomalous compliance of np Au. This is to be expected, as Eq. 2.3 was originally derived from a low-density, open-cell foam structure. The discrepancy can be attributed to several factors: the solid fraction of np Au, which typically ranges between 0.25 and 0.4; microstructural disorder [109, 110]; and deformation modes including axial deformation of np Au ligaments [111, 112]. Systematic deviations from Eq. 2.3 to real np Au have been further linked to variations in connectivity with φ as will be discussed in Sec. 2.3.4.

2.3.2 Scaling law for the elastic properties of the leveled-wave model

For the elastic properties of random three-dimensional porous materials with highly interconnected pores and moderate to high densities, Roberts and Garboczi introduced a modification [26],

$$E_{\text{eff}} = \left(\frac{\varphi - \varphi_0}{1 - \varphi_0}\right)^n E_0\,, \tag{2.6}$$

to the classical Gibson-Ashby scaling law to more accurately describe the effective Young's modulus, E_{eff}, of realistic, random isotropic cellular solids. φ_0 and n in this relation are fitting parameters determined empirically.

For the leveled-wave model, the presence of a percolation threshold facilitated the correlation of its elastic property with the Roberts-Garboczi scaling law. This is expressed as

$$E_{\text{eff}} = C_{\text{R}} \left(\frac{\varphi - \varphi_{\text{p}}}{1 - \varphi_{\text{p}}}\right)^m E_0\,, \tag{2.7}$$

where E_0 is the Young's modulus of the base (constituent) material, as previously defined, and with the adjustable fitting parameters C_R and m without direct physical significance [113]. The numerical values of E_{eff} of the medium with leveled-wave microstructure shows an excellent fit to this modification, yet conceptually differs from the statement of Roberts and Garboczi, who explored structures over a restricted range and suggested that E_{eff} may approach zero at a solid fraction above the percolation limit, φ_p [66, 113]. The scaling law, fitted to the leveled-wave model for φ in the range of 0.2 – 0.50 with C_R = 2.03 and m = 2.56, shows good agreement with experiments reported in [52, 62, 107, 108, 114, 115]. While the stiffness of leveled-wave structures with $\varphi \approx 1/2$ is comparable to that of periodic network structures with the same φ, manifestations with $\varphi < \varphi_p$ lack contiguous load-bearing paths, resulting in vanishing stiffness (See Sec. 2.2.1). A detailed explanation on the number density of the structure's load-bearing connections is described in Sec. 2.3.4.

2.3.3 Size dependency of plasticity and the effect of crystal structure

In small-sized materials, dislocations can travel only short distances before annihilating at the free surface, reducing the probability of multiplication processes compared to bulk metals [116]. When the size of material is smaller than the length scale for dislocation multiplication, it may behave differently from bulk crystals. The high strength observed in micro- to nanosized materials, as in the case of Fig. 1.1(b), can be attributed to dislocation starvation, which is more probable in smaller volumes. The size dependence of the effective yield strength, σ_{eff}, at the sub-micrometer scale can be expressed as a power law: $\sigma_{eff} \propto L^{-n}$, where L represents either the pillar diameter or ligament size [51, 82, 117]. For example, observations on nanoscale gold reports a consistent value of n, ~ 0.6 by [10, 118, 119], 0.5 by [11], or 0.485 by [56].

This "smaller is stronger" trend observed in small-scale materials is primarily attributed to the behavior of dislocations, although the exact mechanisms are still being studied. Classically, material strength increases with dislocation density due to their interactions [119], a phenomenon known as Taylor hardening [120, 121]. However, in small-scale structures, dislocations can easily escape through the abundant surfaces. This loss of dislocations during plastic deformation increases the applied stress required to nucleate or activate new dislocation sources as the sample size decreases. This behavior is opposite to the formerly mentioned Taylor hardening and rather aligns with a dislocation source-limited model, as discussed by [119, 122]. In this scenario, deformation is controlled by the activation of dislocation sources, with two mechanisms under consideration: homogeneous dislocation nucleation and dislocation multiplication. Homogeneous nucleation generates dislocation loops in a nearly perfect crystal structure, thereby requiring significant external stress to overcome the high energy barrier. This has been the valid explanation for the high critical stresses observed in micron-scale whiskers [123]. The initially dislocation-free whisker can sustain higher stresses before dislocations nucleate. As the size of the material decreases, the probability of finding a defect-free region increases, leading to homogeneous nucleation being more likely. On the other hand, dislocation multiplication generates new dislocations from existing ones through mechanisms like the Frank-Read source, where anchored dislocations

expand and form loops under stress. In smaller materials, limited space restricts such expansion, reducing the number of active dislocations and thereby increasing strength. Observations by [122] supports such mechanism since the dislocation nucleation in micron-scale pillars occurs at stresses significantly lower than the theoretical shear strength of the crystal lattice. While both mechanisms are size-dependent, further study is needed to clarify their relative contributions to the observed size-dependent plasticity of nanoporous materials.

As the plastic deformation of sub-micron-sized material is governed by dislocation activity and interaction, the low mobility of screw dislocations in BCC metals may play a crucial role in determining their size sensitivity compared to FCC metals. Contrary to the FCC metals, such as gold, which exhibit comparably low Peierls stress and negligible temperature sensitivity, screw dislocations in BCC metals must overcome a moderate to high level of energy barrier. Thermal activation processes can assist dislocation motion, leading the yield strength to be sensitive to temperature. Above the critical temperature, where thermal energy overcomes the Peierls barrier, dislocations acquire sufficient energy to glide freely [124], and their mobility is no longer governed by thermal activation. For example, the critical temperatures for Nb, Ta, Mo, and W–BCC materials–are 350 K, 450 K, 480 K, and 800 K, respectively [125]. This implies that among those BCC materials, Ta, Mo, and W will experience weaker size sensitivity than Nb at room temperature, while the behavior of Nb may approach that of FCC metals at moderately high temperatures [126], where the influence of the low mobility of screw dislocations becomes negligible [125]. Overall, the size-dependency trend "smaller is stronger" generally holds for small-scale metals, with a positive value of n ranging between 0.22 and 1 [10, 11, 56, 118, 119, 127–130].

Additionally, the mobility of dislocations can be influenced by the core splitting phenomenon, which is particularly temperature-sensitive in BCC metals compared to FCC, to activate secondary mechanisms such as kink-pair nucleation and the kink migration [131]. In screw dislocations, the core can split into two or more partial dislocations. These split configurations may modify the lattice resistance to dislocation motion, which in turn affects the Peierls stress and, consequently, the material's plastic behavior. Earlier studies suggested that a split core structure anchors the dislocation to the lattice, contributing to high Peierls stress [132, 133]. However, recent calculations [134] proposed otherwise, showing that even non-split cores in Mo and Ta exhibit high Peierls stress. This indicates that while core splitting may influence Peierls stress, they are not necessarily the dominant factors. At this point, the extent and how the core splitting impacts the motion of screw dislocations is not yet clearly understood [135]. Furthermore, in materials like Nb, which have a relatively low critical temperature (or high homologous temperature), the influence of core splitting on dislocation motion and plastic behavior is expected to be small.

2.3.4 Topological consideration for mechanical behavior

Network connectivity and elasticity

The Gibson-Ashby model assumes that the entire structure participates in load-bearing, therefore, the solid fraction appears as the primary parameter in the scaling law. However, in experimental observations, including SEM and 3D FIB tomography, have re-

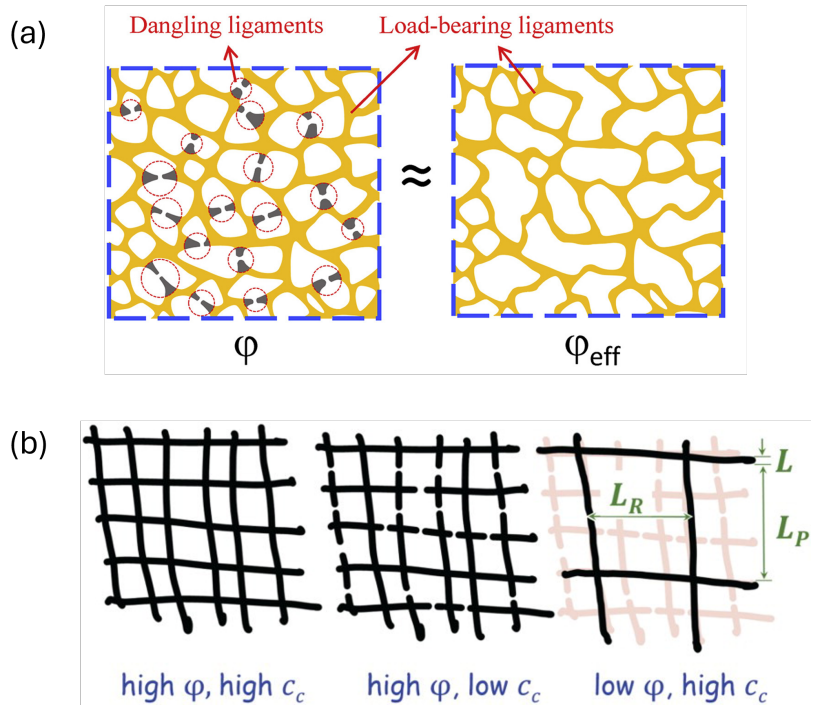

Figure 2.7: (a) Schematic illustration of a nanoporous structure with broken or dangling ligaments (left) and a mechanically equivalent structure with an effective relative density, φ_{eff}, obtained by removing the dangling ligaments (right). Adpated from [62]. (b) Networks with varying solid fraction, φ, connectivity, c_c, ligament diameter, L, pore diameter L_P, and load-bearing ring diameter L_R. One might anticipate similar mechanical behavior between the middle and right structures, while the middle structure is more fragile than the left, despite having a similar φ. Adapted from [32].

vealed that dealloyed nanoporous metals often contain a significant fraction of broken or "dangling" ligaments [62, 136]. They originate from pinch-off events during coarsening which minimizes overall surface energy [101]. Coarsening can occur during dealloying or post thermal annealing and the microstructure evolution during coarsening is explained further in the following section. As a result of this event, using φ alone tends to significantly overestimate the stiffness of nanoporous metals.

To address this discrepancy, Liu et al. proposed the concept of an effective solid fraction, φ_{eff}, to replace φ, thereby $E_{\text{eff}} = \varphi_{\text{eff}}^2 E_0$ [62], as schematically shown in Fig. 2.7(a). The effective reduction in φ on the other hand can be understood as the connectivity between the ligaments, as broken ligaments do not contribute to the overall mechanics. Mameka et al. further proposed that the average number density of load-bearing paths and their size serve as a key connectivity parameter [82], illustrated in Fig. 2.7(b). Similarly, Mangipudi et al. more explicitly incorporated the influence of ligament connectivity into their empirical scaling law by introducing an average number of connections [137]. These studies highlight the connectivity, a topological aspect of the microstructure, in the context of mechanical behavior of nanoporous networks.

Scaled genus

The topological genus, G, is a quantifiable metric for the connectivity of a structure. G denotes the maximum count of connections that can be cut while leaving the body contiguous. For instance, the genus values of a sphere, a doughnut, and a pretzel are 0, 1, and 3, respectively.

For a network with a given microstructure, the extensive property G scales with the volume, V. Structures, for example, with double the volume will contain twice the number of connections. Furthermore, structures with the same volume but a halved microstructural length scale will contain eight times as many microstructural elements and consequently, eight times as many connections. Thus, the relationship between G and the characteristic microstructural length scale, L, is such that G varies inversely with the cube of L. The scaled genus, denoted as g, serves as a volume- and scale-independent descriptor of the microstructural morphology; its physical meaning is therefore the mean number of connections in an elemental building block, of volume L^3, of the microstructure [64, 137–139],

$$g = \frac{GL^3}{V} \,. \tag{2.8}$$

In this context, a convention is adopted for the parameter L that establishes a connection between g and uniquely the skeleton topology, independent of the value of φ. This convention assigns L as the characteristic spacing, $\tilde{L}$, between microstructural elements. For the case of nanoporous materials, the characteristic structure size corresponds to the mean distance between the local centers of neighboring ligament. Practically, $\tilde{L}$ is embodied in the first maximum of the autocorrelation function or, equivalently, in the first maximum in the interference function [66].

For the leveled-wave configuration, the model implies that $\tilde{L} = \alpha\lambda$ with λ the wavelength and $\alpha \simeq 1.23$. The genus per unit volume of the structure, G_v, is expressed as

$$G_v = \frac{1}{12\pi^2}\frac{q_0^3}{\sqrt{3}}\left(1-\xi^2\right)\exp\left(-\frac{\xi^2}{2}\right) \tag{2.9}$$

with q_0 related to characteristic length scale by

$$q_0 = \alpha\frac{2\pi}{\tilde{L}} \tag{2.10}$$

and the level cut ξ

$$\xi = -\sqrt{2}\,\mathrm{erf}^{-1}\left(2\varphi - 1\right) \,. \tag{2.11}$$

The scaled genus of the leveled-wave model is therefore

$$g = \frac{2\pi\alpha^3}{3\sqrt{3}}\left(\xi^2-1\right)\exp\left(-\frac{\xi^2}{2}\right) \tag{2.12}$$

according to [66]. The prediction of Eq. 2.12 for $g(\varphi)$ is shown in Fig. 2.8 versus φ as it varies with φ. Note that the connectivity reaches zero at the percolation threshold, where the structure completely loses connectivity. Those percolation-to-cluster transitions are found at solid fractions $\varphi_\mathrm{p} = \frac{1}{2}(1 \pm \mathrm{erf}\, 2^{-1/2}) \approx \{0.159, 0.841\}$,

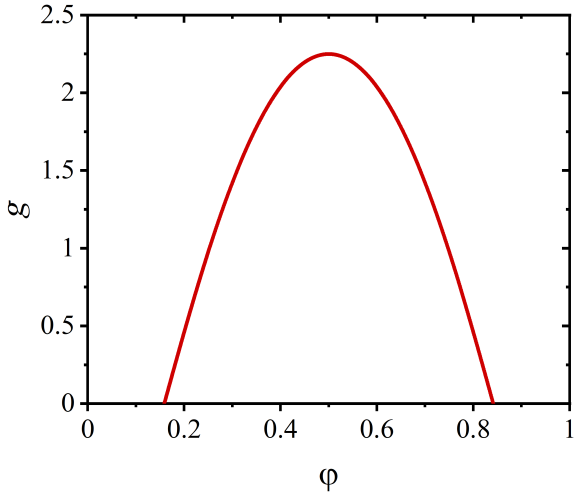

Figure 2.8: Scaled genus, g, versus solid fraction, φ, for the leveled-wave model, as embodied in Eq. 2.12. Note vanishing of g at percolation thresholds.

percolation thresholds for the solid and the pore space, respectively. At $\varphi = 1/2$, the solid and pore space of leveled wave microstructures are isomorphic [22].

While the scaled genus of the leveled-wave model is a valid representation of as-dealloyed np Au, the effect of coarsening on connectivity was captured by kinetic Monte Carlo simulations in [140]. As shown in Fig. 2.9, the characteristic spacing , $\tilde{L}$, increases from its initial value, $\tilde{L}_0$, as coarsening progresses. The scaled genera of the structures are plotted versus $\tilde{L}/\tilde{L}_0$ for $\varphi = 0.22 - 0.50$. For networks with $\varphi \geqq 0.3$, the scaled genus remains invariant, while networks with lower φ gradually lose connectivity, a trend more pronounced in cases with $\varphi = 0.25$ and 0.22. During coarsening, atoms are redistributed through surface diffusion, and thinner ligaments in low-φ structures are more likely to experience faster pinch-off events by Plateau-Rayleigh instability [101] driven by the surface tension. This leads to a faster reduction in connectivity in networks with lower solid fractions, which may alter the mechanical behavior.

Additionally, the scaled genus can be defined using an alternative convention. In the works of [137, 138], the characteristic length scale, L, is expressed as the inverse of the surface area per unit foam volume, S^{-1}. Following this convention, the representative volume of the microstructure is defined as S^{-3}. This leads us to another formulation of scaled genus,

$$\overline{g} = \frac{G}{VS^3}\,. \tag{2.13}$$

By its definition, $\overline{g}$ is then morphology-sensitive.

Based on their definition of $\overline{g}$, Mangipudi et al. have computed E_{eff} for a set of model microstructures, both periodic and random networks, using finite-element-modeling [137]. They suggest a linear relation between $\overline{g}$ and the geometric pre-factor, $C_{\text{E}} = E_{\text{eff}}/\varphi^2 E_0$, for the stiffness

$$C_{\text{E}} = 5\overline{g}\,. \tag{2.14}$$

This scaling relation will be further assessed and compared to the findings presented in this thesis.

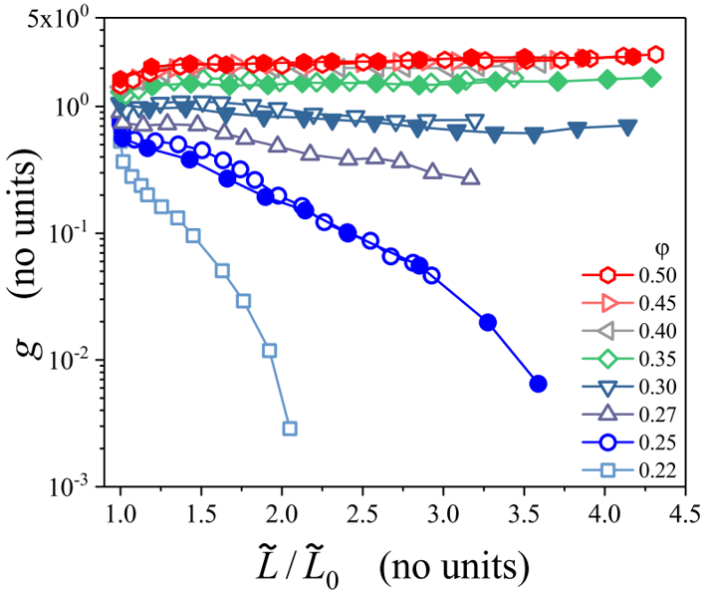

Figure 2.9: Scaled genus, g, versus characteristic spacing, $\tilde{L}$, in different stages of coarsening, for $\varphi = 0.22 - 0.50$. Adapted from [140].

2.4 Hydrogen electrosorption in palladium

2.4.1 Palladium-hydrogen system

Palladium is a unique material that has a strong affinity to hydrogen [144] and can readily absorb hydrogen, forming a metallic hydride under ambient conditions. Figure 2.10(a) presents the phase diagram of the Pd-H system. Here, the changes in the temperature of the hydride specimen lead to corresponding changes in its composition. Thus, the equilibrium hydrogen concentration is determined by the temperature and pressure of the surrounding H_2 gas, or equivalently, overpotential. The equilibrium composition as a function of pressure at constant temperature is plotted in Fig. 2.10(b), showing two distinct phases: an interstitial solid solution α phase with low hydrogen concentration of $\lessapprox 0.03$ [145] and a hydride α' phase (referred to as β in Fig. 2.10(b)) with higher concentration. The plateau in the isotherm indicates the coexistence of these two phases. As shown in the phase diagram, it is challenging to exceed the hydrogen charging capacity of 0.7 [143]. Higher H/Pd ratios are energetically unfavorable, and achieving them typically requires extreme conditions, such as 5 GPa of hydrogen pressure at 973 K for H/Pd = 1.33 [146], establishing 0.7 a practical upper limit in most experimental situations.

As briefly mentioned above, in electrochemical charging, the pressure of gas-phase hydrogen can be directly related to the applied electrode potential, E_{SHE}, measured against the standard hydrogen electrode (SHE) potential. The equivalence arises because both the gas pressure and the electrode potential alters the chemical potential, μ_{H}, of hydrogen atoms and thermodynamically drive the hydrogen to enter the metal lattice. The chemical potential of hydrogen with pressure $p_{\mathrm{H_2}}$ and at temperature T,

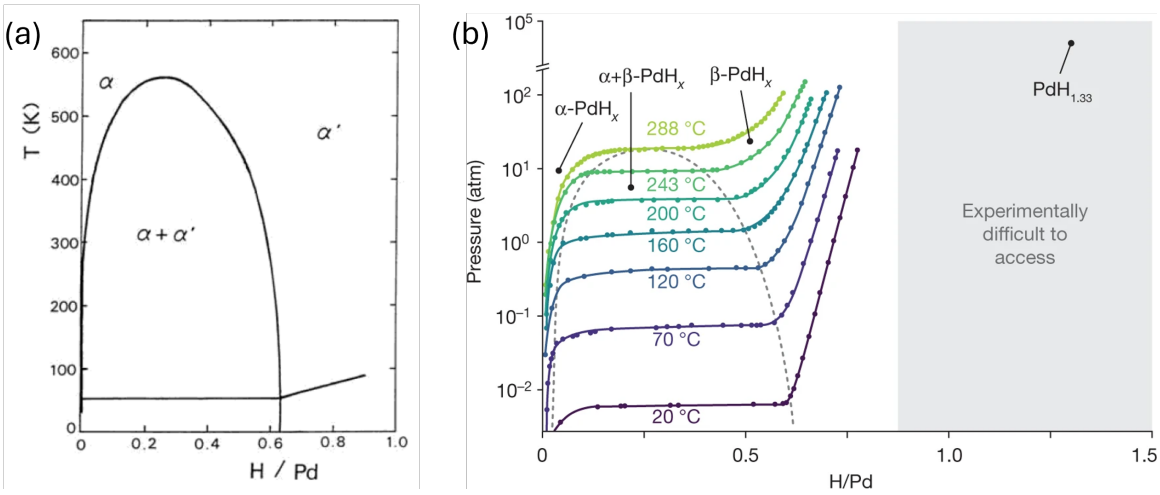

Figure 2.10: (a) Phase diagram of the Pd-H system, adapted from [141]. The abscissa shows the composition as the ratio between the number of H to Pd atoms. The absorption of H by Pd forms two distinct phases, α and α' phases. (b) Pressure versus composition isotherms for the Pd-H system, adapted from [142], originally documented in [143]. Note that the β phase in (b) corresponds to the α' phase in (a). The position of the critical point is determined through graphical interpolation of the data points [143]. At ambient temperature and pressure, the composition is limited to approximately 0.7.

relative to a reference state $p_0 = 1\,\text{atm}$ can be expressed as

$$\mu_\text{H} = \mu_0 + RT \ln \frac{p_{\text{H}_2}}{p_0} \tag{2.15}$$

with the gas constant R, and μ_0, the standard chemical potential of hydrogen gas at the reference pressure p_0. In electrochemical situation, the chemical potential under E_SHE becomes

$$\mu_\text{H} = \mu_0 - FE_\text{SHE} \tag{2.16}$$

with the Faraday constant, F. Equating Eq. 2.15 and Eq. 2.16, the E_SHE equivalent to p_{H_2} is expressed as

$$E_\text{SHE} = -\frac{RT}{F} \ln \frac{p_{\text{H}_2}}{p_0}\,. \tag{2.17}$$

This tells us, for instance, Pd at room temperature (300 K) can transition from the α to the α' phase either by exposing it to $p_{\text{H}_2} \approx 10^{-3}\,\text{atm}$ of hydrogen gas or applying $E_\text{SHE} \approx 0.06\,\text{V}$ in an electrochemical setup.

When Pd transitions to the α' phase, the absorbed hydrogen atoms occupy interstitial sites within the FCC Pd lattice structure, with octahedral sites being energetically more favorable than tetrahedral sites. The lattice parameter increases linearly with the hydrogen composition, which in turn causes volume expansion. The experimentally measured hydrogen-induced volume expansion is compiled over a wide range of hydrogen concentrations in [147] and expressed as

$$\Delta v/\Omega = 0.19 \pm 0.01\,, \tag{2.18}$$

where Δv is the characteristic volume change per hydrogen atom and Ω is the mean atomic volume of a Pd atom. This volume expansion through the α' phase transfor-

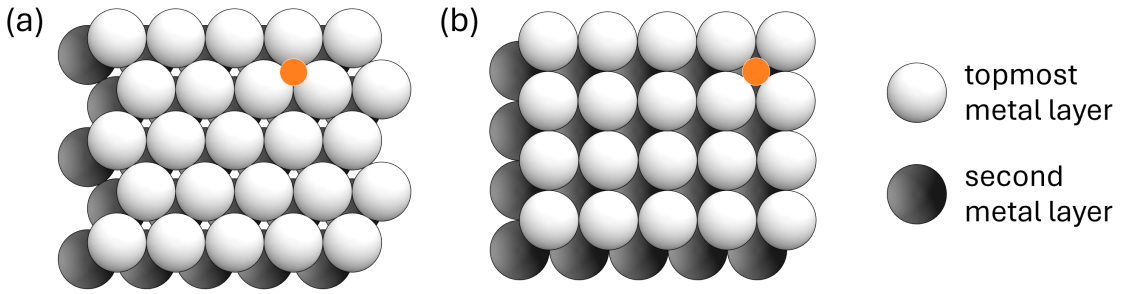

Figure 2.11: Schematic representation of adsorption sites (orange) of UPD H on (a) FCC(111) and (b) FCC(100) surfaces. Figures recreated from [154].

mation serves as the basis of hydrogen actuation property of Pd, along with its high hydrogen permeability and single selectivity to hydrogen [40, 148, 149].

2.4.2 Mechanism of hydrogen electrosorption

Hydrogen absorbing property of Pd has been extensively studied using both the gas phase and electrochemical pathways. In this thesis, hydrogen charging is achieved through electrosorption, using an acidic aqueous solution as a source of proton, H^+. The hydrogen entry into Pd during electrosorption involves several elementary steps. First, H^+ adsorption on the Pd surface atom takes place. Omitting the hydrating H_2O that forms a bonding to H^+, the reaction can be described as

$$H^+ + e^- + Pd \rightarrow Pd\text{-}H_{ads}\,, \tag{2.19}$$

which is also known as the Volmer reaction [150]. Subsequently, the adsorbed hydrogen undergoes interfacial transfer to become absorbed hydrogen:

$$Pd\text{-}H_{ads} \rightarrow Pd\text{-}H_{abs}\,. \tag{2.20}$$

The subsurface hydrogen, H_{ss}, which exists beneath the metal's topmost surface, has also been suggested to form on Pd [151, 152]. H_{ss} eventually becomes absorbed hydrogen. The absorbed hydrogen then diffuses into the bulk of the metal, driven by the concentration gradient of H_{abs}. Concurrently, adsorbed hydrogen can recombine to produce H_2:

$$2Pd\text{-}H_{ads} \rightarrow 2Pd + H_2 \uparrow \tag{2.21}$$

for Tafel reaction (chemical recombination), and

$$H^+ + e^- + Pd\text{-}H_{ads} \rightarrow Pd + H_2 \uparrow \tag{2.22}$$

for Heyrovsky reaction (electrochemical reaction) [153].

A unique aspect of hydrogen electroadsorption on Pd, as the other members of Pt-group metals, is the underpotential deposition of hydrogen (UPD H). This is an electroadsorbed state where hydrogen forms a covalent bond with the metal surface. It is distinguished from the over-potential deposited hydrogen as it occurs at the potentials more positive than the hydrogen evolution equilibrium potential. The process can be represented as Eq. 2.19. Experimentally, it has been observed that up to a monolayer

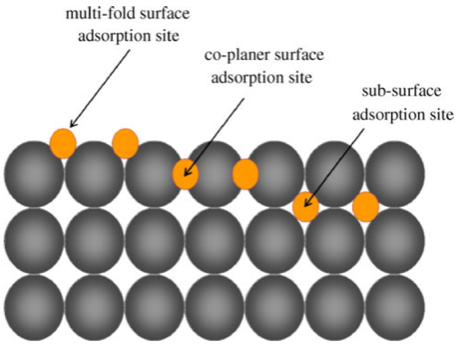

Figure 2.12: Schematic representation of available adsorption sites of UPD H. Adapted from [160].

of UPD H can form [155, 156]. The surface coverage of UPD H depends on the applied potential, and their exact sites depends on the crystallographic orientation of the metal surface. For Pd, which has an FCC crystal structure, UPD H may occupy threefold hollow sites on the (111) face and fourfold hollow sites on the (100) face [154, 157, 158], as illustrated in Fig. 2.11, because they are the most energetically favored hydrogen sites on each facet [159]. It still remains unclear, however, whether UPD H adatoms resides in the multi-fold hollow sites, coplanar sites, or subsurface sites. A schematic of each of these sites is shown in Fig. 2.12.

Since the sorption process involves multiple steps mentioned above, the slowest step limits the overall reaction rate. There are conflicting views whether the rate-determining step in charging/discharging kinetics is the diffusion of hydrogen within the metal's bulk [156] or the penetration through surface barriers [141]. The exact mechanism of charging kinetics is not yet fully understood, and np Pd provides an effective platform for studying this issue. Its high specific surface area highlights surface kinetics, and the relatively fast bulk hydrogen diffusion over short distances distinguishes it from conventional bulk Pd [141].

2.4.3 Butler–Volmer equation

The relationship between the current density, j, and electrode potential of an electrochemical reaction can be described by the Butler–Volmer equation:

$$j = j_0 \left[\exp\left(\frac{\alpha_a z F \eta}{RT} \right) - \exp\left(-\frac{\alpha_c z F \eta}{RT} \right) \right] \tag{2.23}$$

where j_0 is the exchange current density, η is the overpotential, z is the number of electrons involved, α_a and α_c are the unitless anodic and cathodic transfer coefficients, F is the Faraday constant, R is the gas constant, and T is the temperature. The equilibrium state of the system is defined as the condition where the anodic and cathodic current densities are equal in magnitude and opposite in direction, resulting in a total current of zero. Then, the overpotential, η, represents the deviation from this equilibrium potential due to electrode polarization, influences the rate of the reaction. Equation 2.23 is based on the assumption that the anodic and cathodic current densities are independently influenced by η, and that the total current density is the sum of these independent anodic and cathodic contributions [161].

Practically, the Butler-Volmer equation can be extended by incorporating the concentration dependence in the form of

$$j = j_{0,\mathrm{ref}} \left[\exp\left(\frac{\alpha_a z F \eta_{\mathrm{ref}}}{RT} \right) g_{\mathrm{a}} - \exp\left(-\frac{\alpha_c z F \eta_{\mathrm{ref}}}{RT} \right) g_{\mathrm{c}} \right] \tag{2.24}$$

where g_{a} and g_{c} are functions of the electrode surface concentrations of all chemical species [161, 162]. When the concentration of reacting species at the surface is equal to that in the bulk, Eq. 2.24 returns to Eq. 2.23. In Eq. 2.24, both exchange current density and overpotential are measured at chosen reference conditions, denoted by the subscript "ref", so that η_{ref} can be interpreted as the electrode polarization against a fixed reference electrode. This approach retains the aspects of experimentally measurable quantities, while maintaining a well-defined reference state [161].

In the context of hydrogen-metal sorption reactions, the Butler-Volmer equation describes the charge transfer process involved in hydrogen electrosorption, with η acting as the driving force that directly influences the reaction rates. It accounts for both the forward (injection) and backward (extraction) reactions, enabling the analysis of reaction kinetics [163].

Chapter 3

Materials and experimental procedures

3.1 Fabrication methodology of nanoporous niobium

3.1.1 Nb-Ni master alloy

The precursor alloy with a nominal composition of $Nb_{25}Ni_{75}$ (at%) was prepared from high-purity Nb (99.96%, VWR International GmbH) and Ni (99.99+%, Sigma-Aldrich Chemie GmbH) metal wires. The composition was carefully chosen to allow a bicontinuous structure to develop upon dealloying. The Nb-Ni phase diagram, as shown in Fig. 3.1, predicts a single intermetallic phase of Ni_3Nb at this composition [164, 165]. The Nb and Ni metal wires are repeatedly melted and solidified in an argon atmosphere using an arc melter (MAM-1, Edmund Bühler). After that, the solidified alloy ingot of approximately 2 g was annealed for 12 hours at 1200°C in a tube furnace (ROC 50/450/15, ThermConcept) with argon gas flow, and it was subsequently cooled in the furnace to room temperature. After cutting the ingot into a circular disk, both the upper and bottom surfaces were ground to P2500 grade SiC papers using a guiding die. This established smooth and coplanar surfaces for later loading in the testing device. Then it was cut with a diamond wire saw (Model 3032, Well Diamond Wire Saw) into cuboids with a cubic length of 1 ± 0.2 mm on each side.

3.1.2 Liquid metal dealloying of Nb-Ni

Niobium is immiscible to molten Mg while Ni has a negative mixing enthalpy with Mg [96]. Thus, liquid metal dealloying was performed on $Nb_{25}Ni_{75}$ cuboids using a molten Mg bath maintained at a set temperature.

Precursor sample was nestled within ~100 mg of Mg (as granules, -20+100 mesh, 99.8% metal basis, Alfa Aesar) in a Sigradur G glassy carbon crucible (GAT 007, HTW Hochtemperatur-Werkstoffe GmbH) of volume 0.07 mL. This amount of Mg ensures a thorough coverage of the sample, letting the precursor remain fully immersed in molten Mg at elevated temperature and allowing dealloying to occur uniformly on each surface. The crucible, containing the sample and Mg granules, was then heated in an infrared furnace (IRF 10, behr), under Argon flow (Argon 5.0, 99.999%) and with a heating rate

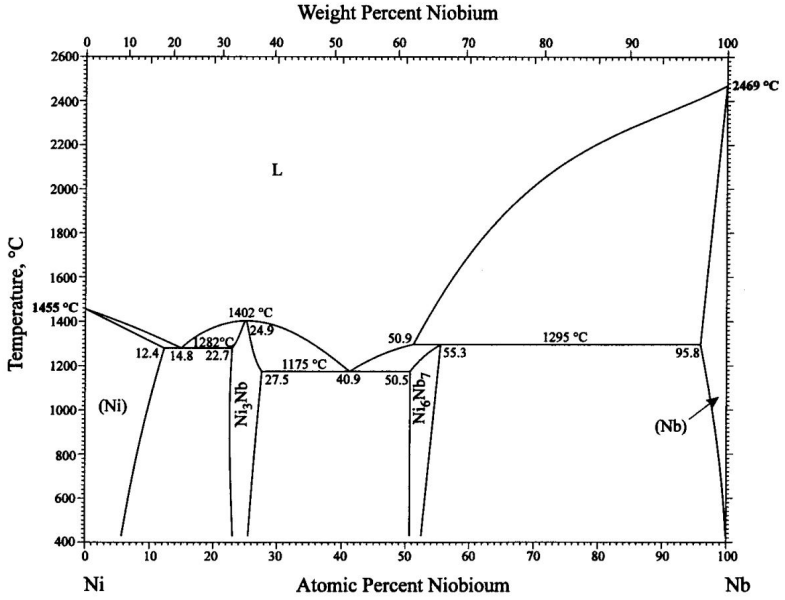

Figure 3.1: The Ni-Nb phase diagram. Adapted from [165].

of 50°C/s. The set temperature for the dealloying procedure ranged between 800°C and 900°C, with a tight control of ± 2°C from each target point. This is higher than the melting point of Mg (650°C) but lower than that of Nb or Ni. The entire dealloying duration was modulated between 30 and 90 minutes. Figure 3.2 shows three states of the LMD process, (a) the precursor, (b) the precursor and the Mg granule in the crucible before dealloying, and (c) the dealloyed sample covered with solidified Mg.

After dealloying, the sample was cooled down to room temperature inside the furnace and revealed to ambient air. Since the sample was tightly covered with a solidified Mg lump, this excess Mg mixed with Ni was etched by 3 M nitric acid for >12 hours at room temperature. The sample was then kept in ultrapure water (Arium Comfort I TOC, Sartorius) for another >12 hours followed by rinsing with ethanol and drying in air.

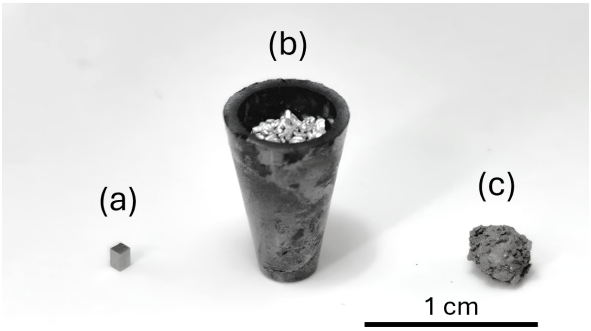

Figure 3.2: Photograph of steps during liquid metal dealloying. (a) Precursor sample. (b) Crucible containing Mg granules and one precursor sample (invisible), before dealloying. (c) After dealloying. The Mg melt is solidified and covers the sample. This is then removed by nitric acid.

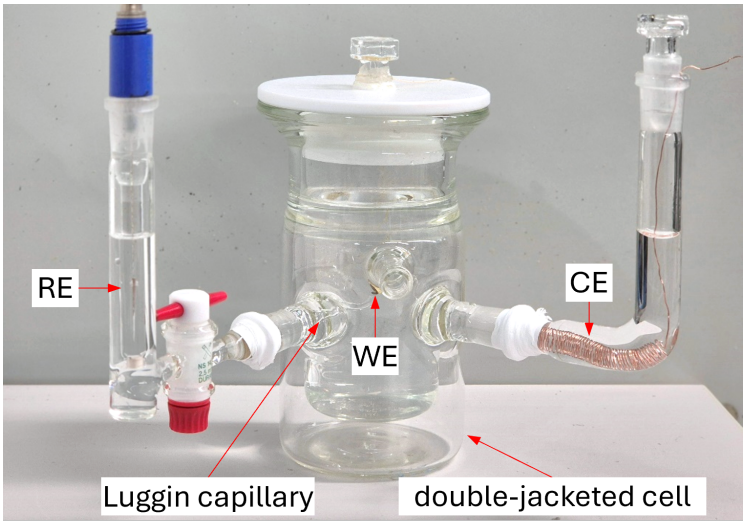

Figure 3.3: Photograph of the dealloying setup. A double-jacketed, three-electrode chemical cell is equipped with reference (RE), working (WE), and counter (CE) electrodes, and the electrolyte.

3.2 Fabrication methodology of nanoporous palladium

3.2.1 Pd-Cu master alloy

A Pd-Cu alloy with a nominal composition of $Pd_{15}Cu_{85}$ (at%) was utilized as a precursor alloy for the preparation of np Pd. Pd and Cu can form a homogeneous solid solution [166] where Pd and Cu atoms are uniformly distributed. Cu can then be selectively dissolved due to its lower reduction potential compared to that of Pd. The composition of $Pd_{15}Cu_{85}$ was chosen to facilitate dealloying across the sample dimension while maintaining a bicontinuous and freestanding structure [167].

The Pd-Cu alloy was prepared with a similar procedure to that of NbNi alloy described in Sec. 3.1.1. Metal wires of Pd (99.95%, ChemPur Feinchemikalien und Forschungsbedarf GmbH) and Cu (99.999%, Alfa Aesar) underwent a process of multiple melting and solidifying cycles in an argon atmosphere using an arc melter. To ensure a homogenized composition, the alloy ingot is annealed at 760°C under vacuum ($\approx 10^{-5}$ mbar) in the sliding furnace for 4 days and quenched in water. Subsequently, each ingot is cold-rolled by a manual rolling mill (Dohrmann 726W) until it reaches the thickness of ≈ 1 mm. Both faces of the disc-shaped ingot were mechanically ground with fine SiC papers P1200, P2500, and P4000 using a guiding die. The ingot was then cleaned with ethanol in an ultrasonic bath for 10 minutes. The ingot was then cut with the diamond wire saw to the final cuboid shape. Following these preparation steps, each master alloy sample has a cuboid shape with approximate dimensions of $1 \times 1 \times 1\,\mathrm{mm}^3$, with two of its faces polished and parallel to each other.

3.2.2 Electrochemical dealloying of Pd-Cu

Nanoporous Pd was prepared through the electrochemical dealloying of a $Pd_{15}Cu_{85}$ precursor alloy. This process involves the selective etching of the chemically more active component in the alloy, Cu in this case. The dealloying procedure was designed with reference to prior work [167].

To achieve a controlled dissolution rate, both an external potential and a defined temperature are necessary. A three-electrode chemical cell was employed, consisting of a working electrode (WE), a reference electrode (RE), and a counter electrode (CE), and a double wall to establish the required environment. Figure 3.3 presents a photograph of the setup. In the setup, the precursor alloy sample was connected to a gold wire serving as the WE, and Ag/AgCl/3M KCl and a Cu wire were used as the RE and CE, respectively. The electrodes were immersed in a solution of 1.0 M H_2SO_4 solution (ROTIPURAN® 98%, Roth) and the entire cell was maintained at 60°C using a thermostat that circulates heated water in the outer shell of the double-jacketed electrochemical cell.

The constant dealloying potential of 790 mV vs. standard hydrogen electrode (SHE) was applied using a potentiostat (Metrohm AUTOLAB) controlled by the NOVA software. The dealloying potential was maintained until the current decayed to 10^{-5} A. Subsequently, the sample was briefly rinsed in ultrapure water before proceeding with the reduction process described in the following section.

3.2.3 Electrochemical reduction

After the dealloying process, electrochemical reduction was performed on the as-dealloyed sample to remove excess residual Cu [168]. To carry out this process, a carbon fabric with a specific surface area of >1800 m^2/g (Kynol Europa GmbH, ACC-5092-20) and of approximately 3×3 cm in size, was employed as the CE to account for the increased surface area of the dealloyed sample. The WE and RE were the same as described in Sec. 3.2.2 with a fresh 1.0 M H_2SO_4 electrolyte. Ten cycles of cyclic voltammetry (CV) were performed, sweeping from 0 V to 1.2 V vs. SHE, with a scanning speed of 5 mV/s at room temperature.

Following this step, any remaining acid was removed by immersing the sample in ultrapure water for more than 12 hours, followed by ethanol for more than 2 hours. The sample was then air-dried.

3.2.4 Tailoring of ligament size

The ligament size of the np Pd can be tailored by thermally annealing the sample. After dealloying and electrochemical reduction, the samples are exposed to an elevated temperature. Structural coarsening, driven by surface atom diffusion [169, 170], allows control over the final structure size by adjusting the coarsening temperature and duration. Each sample underwent thermal treatment under vacuum conditions ($<10^{-5}$ mbar) at temperatures of 150°C, 200°C, 300°C, or 400°C for 5 minutes, depending on the desired ligament size. The furnace (MILA-5000, ULVAC GmbH) combined with the vacuum pump (TwisTorr 74 infrared FS AG, Agilent Technologies) was used for this process.

3.3 Materials characterization

3.3.1 Determination of solid volume fraction

Once the nanoporous sample is prepared, the solid volume fraction, φ, of the sample was determined from its mass and volume. The volume was obtained from edge lengths measured with an optical microscope (SZX10, Olympus). The mass of each sample was measured by a precision balance (ME36S, Sartorius).

3.3.2 Structural and phase characterization

The morphology of the dealloyed nanoporous samples was observed by a scanning electron microscope (SEM, Zeiss Supra VP55) using secondary electron and in-lens detectors with an accelerating voltage of 3-10 kV and a typical working distance of approxmately 4 mm. In order to determine statistical information of the microstructure sizes in electron micrographs, the Python package AQUAMI [171] was employed. Micrographs were first captured at ×10k magnification for each sample's fracture surfaces as representative of the bulk, and the neck diameters of the ligaments and their distribution were observed based on the SEM images. At least 300 diameter values were acquired to calculate the mean ligament size, L, and the variance, s, of the size distribution. The bootstrap error is quoted as a measure for the uncertainty of L [172].

The existing phases and chemical composition of the precursor alloy and dealloyed samples were examined using two complementary techniques: (1) energy dispersive X-ray spectroscopy equipped with SEM and (2) wide-angle X-ray diffraction. Energy dispersive X-ray spectroscopy in the SEM (Zeiss Supra VP55) used a 80 mm^2 silicon drift detector (Oxford Instruments). The accelerating voltage of the SEM was adjusted to 10-20 kV and working distance was approximately 7-9 mm. Characterization by wide-angle X-ray diffraction used a powder diffractometer (D8 Advance, Bruker AXS) in focusing Bragg-Brentano geometry, with Mo K_α radiation and an energy dispersive, position sensitive detector (LynxEye XE-T).

3.3.3 Mechanical characterization

The samples used for mechanical tests were cuboids with dimensions of $\sim 1 \times 1 \times 1\,mm^3$. Using a conventional testing device (Z010, ZwickRoell equipped with a laser speckle extensometer system, LaserXtens, for strain measurement), uniaxial compression tests were conducted at room temperature. Figure 3.4 shows the testing setup with an np Nb sample. To ensure good contact with the load surfaces, the position of the sample was optimized using the camera feed of the laser speckle extensometer system and a 2 N preload applied. These steps helped minimize experimental artifacts related to surface roughness or nonparallelity of the surfaces. Stress-strain response was recorded with an engineering strain rate of $10^{-4}\,s^{-1}$ and unload steps after each 2.5×10^{-2} strain increment. Each unloading step terminated at 1 MPa stress and was followed by immediate reloading.

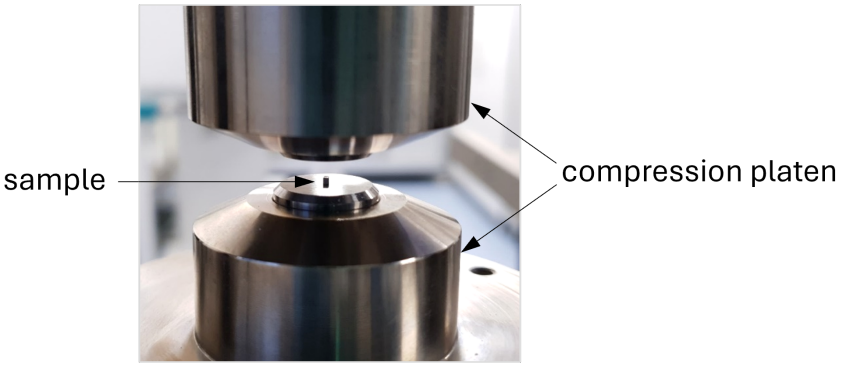

Figure 3.4: Photograph of the mechanical testing setup. The sample is placed between two compression platens.

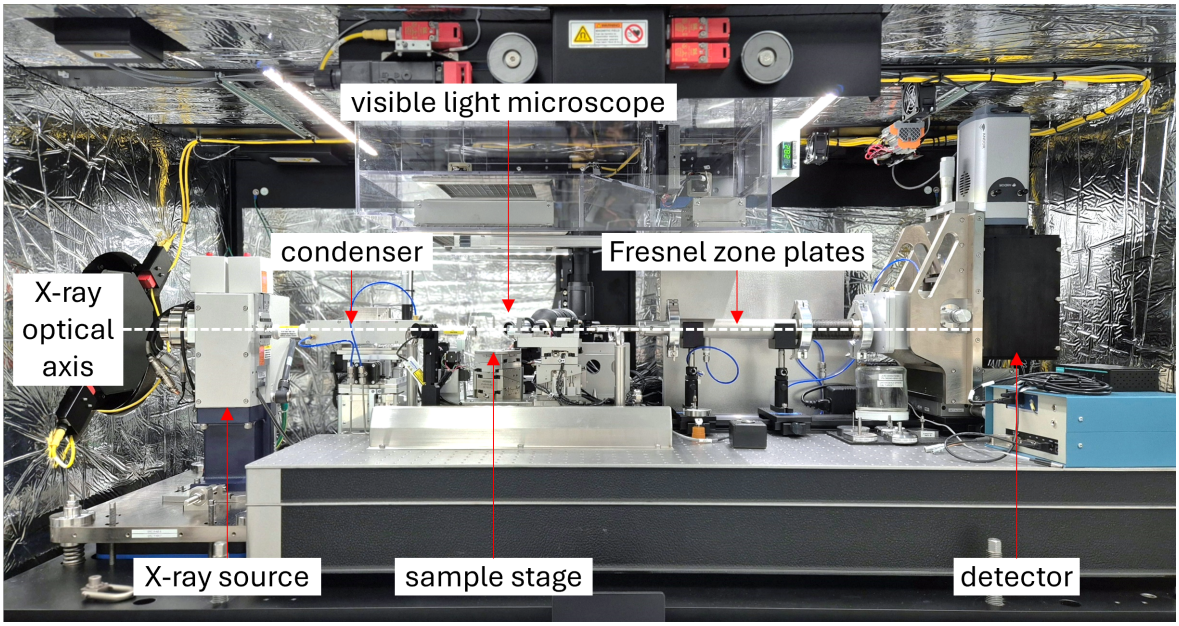

Figure 3.5: Front view of the Zeiss Xradia 800 Ultra X-ray microscope, with access doors open. Major components are labelled.

3.3.4 Tomographical characterization

The three-dimensional structural properties of np Nb were investigated using X-ray nanotomography. The tomography samples were prepared by Xe plasma focused ion beam (Helios G4 UXe, Thermoscientific). A freestanding cuboid was first cut and then milled to a cylindrical micropillar. The ion beam was initially directed normal to the pillar axis to lathe mill the sample, with an accelerating voltage of 30 kV and beam currents of 2.5 and then 1 μA. Next, beam currents of 4 and then 1 nA were applied, directed from the top. The low second beam current prevents "curtaining" and minimizes energy intake to the pillar surface. Their size, 50 μm in diameter and 88 μm in height, relative to the ligament size, renders the resulting columns a representative sample of the microstructure [173]. Due to their large diameters, FIB damage in the bulk of the pillars may be excluded.

The tomography measurement in a Zeiss Xradia 800 Ultra (Fig. 3.5) used monochro-

matic Cu K_α radiation and a large field of view (LFOV) imaging mode with cross-sectional images taken from an 180° arc. Since the height of the micropillar is larger than the field of view of 65 μm × 65 μm, two successive measurements were performed for each micropillar and the two sets of images were stitched using ImageJ [174].

The images were binarized into solid and pore via the Otsu threshholding algorithm [175] integrated in ImageJ, with a threshold matching the solid fraction to the value independently determined from mass per volume.

The binarized reconstruction formed the basis for determining the topological genus, G, with the software plugin BoneJ in ImageJ [176–178]. The scaled genus, g, as introduced in Sec. 2.3.4, is then calculated to determine the characteristic of the topology that is independent of the sample size and of the characteristic microstructural length scale. It is defined by

$$g = \frac{G}{V}\tilde{L}^3 \tag{3.1}$$

where V is the total volume (solid plus pores) and $\tilde{L}$ is the mean spacing between neighboring Nb ligaments.

For use in Eq. 3.1, $\tilde{L}$ is determined from the surface area of the reconstruction, as measured by evaluating the surface mesh with Simpleware ScanIP (SimpleWare Product Group, Bradninch Hall, United Kingdom). Specifically, the relation between $\tilde{L}$ and the surface area-to-volume ratio, S, of leveled-wave structures is used. As stated earlier, those structures provide a geometric model approximating dealloyed nanoporous solids [66]; they are characterized by

$$S = \frac{2q_0}{\pi\sqrt{3}}\mathrm{e}^{-\xi^2/2} \tag{3.2}$$

with q_0 the magnitude of a characteristic wave vector and ξ defined as in Eq. 2.11. Equation 3.2 is solved for q_0 and then $\tilde{L}$ obtained as

$$\tilde{L} = \alpha\frac{2\pi}{q_0}, \tag{3.3}$$

where α is a numerical constant, $\alpha = 1.23$ [66].

3.3.5 Electrochemical techniques

Chronoamperometry

Chronoamperometry technique is utilized to apply a square-wave electric potential to the working electrode. In this study, it serves two primary functions: first, to maintain a constant potential during the dealloying process, and second, to monitor the time-dependent response to potential jumps or achieve equilibrium at fixed potential levels.

Figure 3.6 illustrates the typical application of chronoamperometry. Figure 3.6(a) is from the dealloying process of the $Pd_{15}Cu_{85}$ precursor alloy in 1.0 M H_2SO_4. A steady potential measured versus SHE, E_{SHE}, is applied to the alloy to selectively corrode Cu in the sample, until the current approaches close to zero. The current and charge arising from the corroded Cu^{2+} ions are plotted over time in the figure. Figure 3.6(b) presents an example of the hydrogen electrosorption process of np Pd in response to a sequence of square-wave potentials, where the resulting current and charge responses are recorded over time.

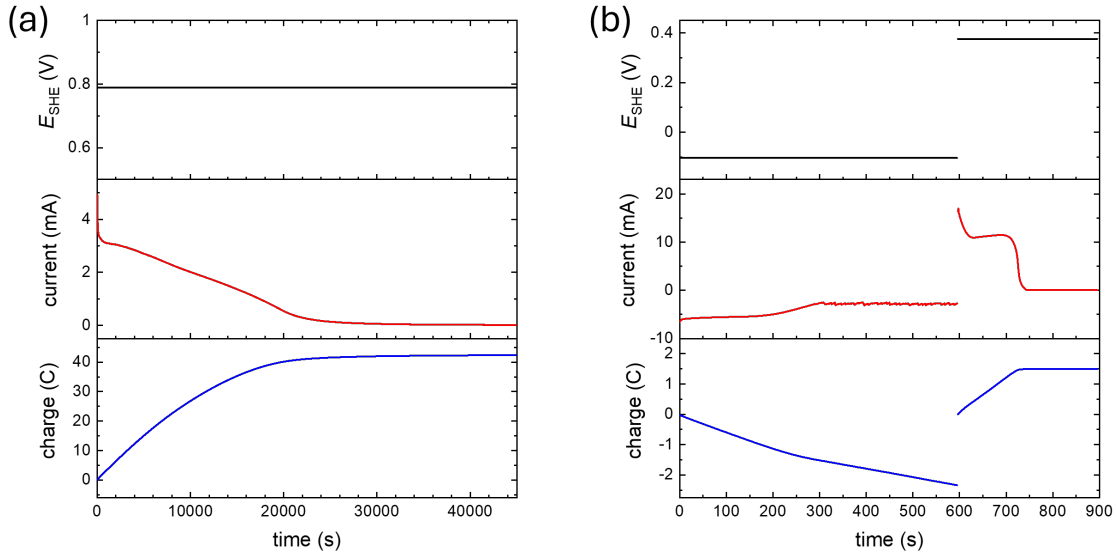

Figure 3.6: Examples of chronoamperometry. Potential, current, and charge are plotted over time. (a) Application of a constant potential for dealloying $Pd_{15}Cu_{85}$ alloy to produce nanoporous Pd. (b) Application of a potential step for hydrogen absorption at $E_{SHE} = -100\,mV$, followed by desorption at $E_{SHE} = 380\,mV$.

Cyclic voltammetry

In a cyclic voltammetry (CV) measurement, the potential at the working electrode is linearly swept across the potential range of interest, while the corresponding current response is simultaneously observed. The potential is swept between the upper and lower limits defined by the user at a selected scan rate. The CV technique is employed for (1) the electrochemical reduction of as-dealloyed np Pd, as described in Sec. 3.2.3 and (2) to determine the active surface area of np Pd. Figure 3.7(a) displays an example of a single cycle of CV potential waveform, E_{SHE}, with respect to SHE, with a scan rate of 10 mV/s and the resulting current response from a np Pd at room temperature. It is typically presented as a current versus potential plot, as shown in Fig. 3.7(b).

Electrochemical impedance spectroscopy

Electrochemical impedance spectroscopy (EIS) is employed to observe the reactions and kinetics of the np Pd-H system. The system was established by immersing np Pd in ultrapure 1.0 M H_2SO_4, an aqueous acidic solution serving as a reversible charging source of protons [180]. A three-electrode cell was employed to apply a periodic signal to WE, the np Pd sample. Gold foil and gold wire were employed to establish electrical connections between the sample and the setup. For the other electrodes, commercial Ag/AgCl/3M KCl electrode and carbon cloth were used as RE and CE, respectively. The influences coming from mutual inductance of the equipment was minimized by covering up the cell wall with a homemade Faraday cage.

The np Pd-H system was considered to be linear and time(t)-invariant. In other words, the response of the system to an input occurs with same frequency as the input, and depends solely on the characteristics of the input signal, without being influenced

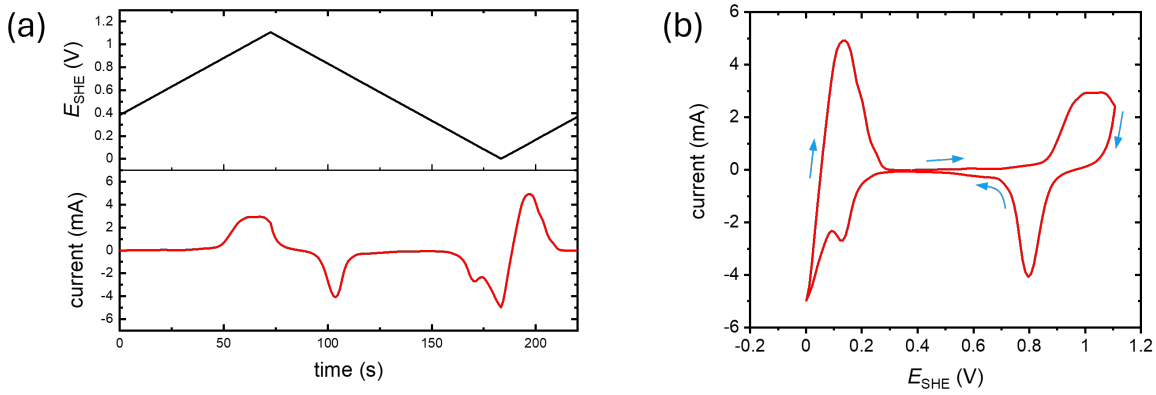

Figure 3.7: An example of cyclic voltammetry measurement on nanoporous Pd. (a) Potential versus SHE, E_{SHE}, sweep and current response over time. (b) Cyclic voltammogram of nanoporous Pd in 1.0 M H_2SO_4 recorded from the potential waveform in (a). The arrows show the scan direction of potential.

by any time-dependent effects such as degradation or other dynamic parameters. Based on these assumptions, the system's response under the sinusoidal perturbation signal,

$$E(t) = E_{\mathrm{DC}} + \Delta E \sin(2\pi f t)\,, \tag{3.4}$$

was recorded at each frequency values, f, ranging from 10 mHz to 100 kHz. E_{DC} is the DC component of the potential and ΔE is the amplitude of the perturbation. E_{DC} was set to maintain the system between the capacitive region and fully hydride region at each measurement. ΔE is fixed to 5 mV to conform the linearity constraint and to achieve optimal signal-to-noise ratio. The validity of the obtained data was evaluated by running the Kramers-Kronig (K-K) test using NOVA software. This test assesses whether the acquired data complies with the K-K relations, which allow the determination of the real part of a complex function from its imaginary part, and vice versa. The mathematical derivation of these relations can be found elsewhere [181]. Note that the K-K relations are based on the key assumptions that the complex function is analytic in the upper half of the complex plane, and it must vanish at infinitely high frequencies as fast or faster than $1/f$. During the K-K test, the impedance data are fitted to a model circuit which inherently satisfies the K-K relations. The outcome is then given as the sum of squares of the relative residuals. The sum of the residuals from the real and imaginary parts of the data set is maintained below 10^{-5}, which is considered a reasonably satisfactory fit [179]. This threshold indicates minimal measurement errors and confirms that the system exhibits linear and time-invariant behavior. Satisfaction with the K-K test is a necessary but not sufficient condition to ensure linearity, stability, and causality requirements.

The sinusoidal nature of the input and output signals enables analysis in the frequency domain using phasor notation. The relationship between the two signals corresponds to the system's transfer function [182]. This transfer function is defined as the ratio of the two phasors, input voltage and output current in this case, so that it corresponds to the impedance of the system. The total impedance at each frequency, $Z(f)$ can be plotted in the complex plane in the form of Nyquist plot, with its real

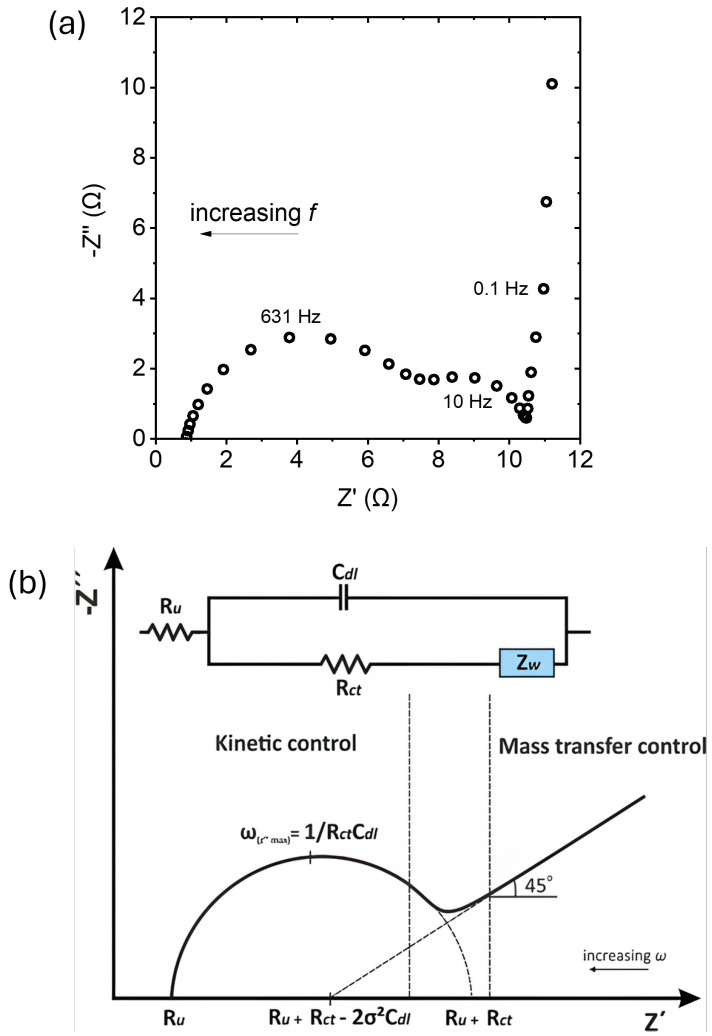

Figure 3.8: (a) A typical Nyquist-plot representation of the complex impedance measured from nanoporous Pd using electrochemical impedance spectroscopy. $E_{\mathrm{DC}} = 90\,\mathrm{mV}$ and $\Delta E = 5\,\mathrm{mV}$. The abscissa and ordinate represent the real part and the negative imaginary part of the complex impedance, respectively. (b) Equivalent electrical circuit and its physical interpretation corresponding to the representative Nyquist plot. Adapted from [179].

part, Z', on the abscissa and its imaginary part, Z'', on the ordinate, as in Fig. 3.8(a). The impedance spectrum is then fitted to an equivalent electric circuit model composed of passive components such as resistors, capacitors, and inductors. Figure 3.8(b) shows an example of a circuit model and its physical interpretation. In this thesis, any inductive behavior is excluded as it lacks physical applicability to the system. The numerical values of the components are retrieved from the circuit simulated by NOVA software. The circuit model is then analyzed to a corresponding physical process, and its time constant is given as

$$\tau = RC\,. \tag{3.5}$$

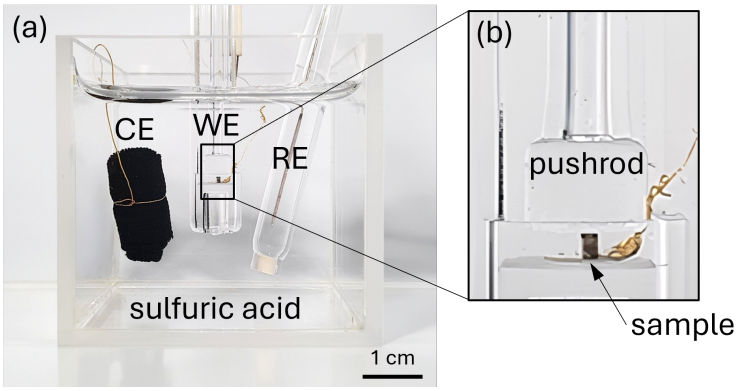

Figure 3.9: (a) Photograph of the electrochemical hydrogen charging cell. The three electrodes–WE, RE, and CE–are the nanoporous Pd sample, Ag/AgCl/3M KCl electrode, and carbon cloth, respectively. The electrodes are immersed in 1.0 M H_2SO_4 solution. (b) Enlarged view near the nanoporous Pd sample. The pushrod is in contact with the sample for in-situ dilatometry measurement.

3.3.6 In situ dilatometry

A vertical dilatometer (Linseis L75V) is combined with an electrochemical setup to monitor the in situ length variation of the np Pd sample during hydrogen charging and discharging. A photograph of the setup is shown in Fig. 3.9. Similar to the three-electrode cell configuration in Sec. 3.2.3, the WE, RE, and CE are the sample connected to a gold wire, Ag/AgCl/3M KCl reference electrode, and carbon cloth, respectively. The electrolyte is 1.0 M H_2SO_4. To maintain contact between the sample and the pushrod of the dilatometer, a constant vertical force of 100 mN is exerted on the sample throughout the measurement. During the experiment, the change in the sample's length is tracked over time as a potential is applied to control hydrogen concentration. Strain is then calculated as the ratio of the sample's length change, Δl, measured by the dilatometer, to the initial length, l_0, measured by the optical microscope (SZX10, Olympus).

Chapter 4

Results

4.1 Mechanical behavior, topological characterization, and their interrelation in nanoporous metals

The following sections begin with the introduction of a genus-dependent model to explain the mechanical properties of nanoporous metals. The model is then compared to synthesized np Au and extended through numerical simulations. Finally, experimental findings on np Nb are presented.

4.1.1 Genus-dependent scaling for leveled-wave-like networks

This section explores the relationship between the mechanical and structural properties of nanoporous materials, on the basis of existing database and novel simulations [183, 184]. Figure 4.1 illustrates the connection between previous works [66, 106] and the contributions of this study to the scaling law for the effective macroscopic Young's modulus of random network materials.

In np Au, $\tilde{L}$ can be tuned by deliberate coarsening at constant solid fraction, φ. An increase in temperature accelerates the surface diffusion, and this lets the microstructure evolve in such a way that the net area of surface and, consequently, the net excess surface energy is decreased, with a concomitant increase in $\tilde{L}$. That process can entail a strong decrease in E_{eff}. While atomistic simulations using embedded-atom interatomic potentials suggest a noticeable size-dependence of the effective elastic behavior of metal nanostructures [185, 186], more realistic investigations based on density functional theory establish that an inherent size-dependent elasticity can be expected in individual struts only for ligament sizes well below 10 nm [187]. Thus, the experimentally observed decrease in E_{eff} of np Au at constant φ indicates a loss in connectivity [62, 63]. Even in the as-prepared state of np Au, a strong and systematic deviation of $E_{\text{eff}}(\varphi)$ from the Gibson-Ashby behavior has been linked to variations in the connectivity: as np Au's density is reduced, the scaled genus, g, will systematically drop (as implied by Eq. 2.12), with a concomitant drop in E_{eff} [66].

A convenient hypothesis states that the joint impact of solid fraction and of connectivity on E_{eff} of random network structures can be separated in a product [65, 137],

$$E_{\text{eff}} = f_{\text{g}}(g) f_{\varphi}(\varphi) E_0 \tag{4.1}$$

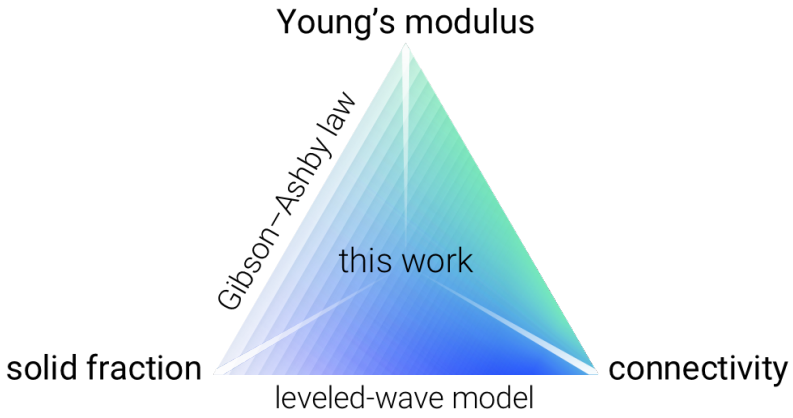

Figure 4.1: A pictorial summary of previous works [66, 106] and this work. The Gibson-Ashby scaling law is valid only for a constant connectivity case, as visualized by the lines parallel to the upper left edge of the triangle. The leveled-wave model assumes a fixed analytical relation between solid fraction and connectivity. This work reports a generalized scaling relation between the three parameters– Young's modulus, solid fraction, and connectivity.

with f_g and f_φ dimensionless scaling functions of g and φ, respectively.

Equation 2.3 provides a special case of Eq. 4.1 for constant g. Its suggestion that $f_\varphi \propto \varphi^2$ reflects the mechanics of the network structures in the limit of long thin struts, where φ is low and the elastic deformation is bending-dominated. In terms of the aspect ratio of the strut, r (diameter divided by length), it is found that $\varphi \propto r^2$ [104] and that the bending moment M, which determines the stiffness, scales as $M \propto r^4 E_0$. This immediately leads to the quadratic f_φ [106] and, hence, to the special form of Eq. 4.1 for bending-dominated network structures,

$$E_{\text{eff}} = f_g(g)\varphi^2 E_0 \,. \tag{4.2}$$

The argument holds independent of the detailed topological architecture (number and arrangement of struts in the representative local building block) of the network and, therefore, also independent of its connectivity.

Mangipudi et al. [137] have computed E_{eff} for a set of model microstructures by finite-element-modeling (FEM). Exploiting Eq. 4.2, they suggest a linear form, $f_g \propto g$. Their set of model structures contains both, periodic and random networks. In that context it is significant that E_{eff} is not uniquely determined by φ even for periodic network structures with a given unit cell and identical g. For instance, random displacements of the nodes can bring a substantial decrease in E_{eff} [60], and the morphology of the struts requires consideration [188]. Those observations are not immediately compatible with deriving scaling laws–such as that of Mangipudi et al.–by analysis of a set combining ordered periodic with random structures.

Focusing on np Au, Jin and coworkers have introduced and experimentally substantiated the notion of an effective load-bearing solid fraction, φ_{eff}, which can replace φ in Eq. 2.3. Their φ_{eff} counts only the load-bearing regions of the solid, ignoring the volume of "broken" struts that do not contribute to the mechanics [62, 63]. Their work does not address the topological genus hence leaves open how φ_{eff} relates to g. Yet, in line with their approach, one may assume a linear scaling between the two quantities–

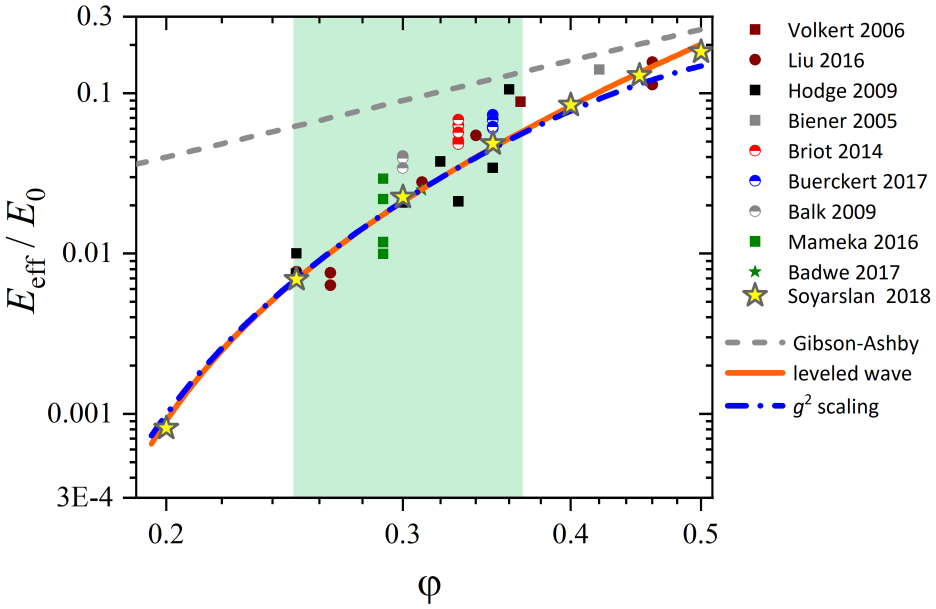

Figure 4.2: Normalized effective Young's modulus E_{eff}/E_0 versus solid fraction φ. Dashed line, Gibson-Ashby scaling law. Solid line, modified Roberts-Garboczi law, Eq. 4.4. Dash-dotted line, genus-dependent scaling law, Eq. 4.5. Symbols, experimental results for as-prepared nanoporous gold reported by [6, 30, 32, 62, 107, 115, 189–191] and FEM data for the leveled-wave model [66].

starting from a well-connected reference structure, every broken strut reduces g and φ_{eff} in the same proportion. In other words,

$$\varphi_{\text{eff}}(g,\varphi) = \frac{g}{g_0}\varphi\,. \tag{4.3}$$

with g_0 a constant that depends on the geometry of the reference structure. In view of Eq. 2.3, Eq. 4.3 would imply that the connectivity-elasticity law might be quadratic, as opposed to the linear relation suggested in [137].

As mentioned in Sec. 2.2.1, for the leveled-wave model and $\varphi \ll 0.5$, a modification,

$$E_{\text{eff}} = C_{\text{R}}\left(\frac{\varphi-\varphi_{\text{p}}}{1-\varphi_{\text{p}}}\right)^{m} E_0\,, \tag{4.4}$$

of the Roberts-Garboczi scaling law for random networks [26] has been found to agree well with experimental data for as-prepared np Au and with numerical results for E_{eff} of the leveled-wave model [66]. The adjustable parameters in Eq. 4.4 there are $C_{\text{R}} = 2.03$ and $m = 2.56$.

Figure 4.2 shows Eq. 4.4, superimposed to experimental literature data for as-prepared np Au [6, 30, 32, 62, 107, 115, 189–191] and to FEM data for the leveled-wave model [66]. The strong deviation from the Gibson-Ashby law at low φ is a signature of the loss of connectivity as the percolation threshold is approached.

As mentioned above, the drop in E_{eff} upon coarsening of np Au [32, 62, 63] suggests a loss in connectivity. Yet, data for g is not available for those experiments. Studies by experimental 3D tomographic reconstruction [137, 139, 192] explore how g evolves

upon coarsening. Those studies conclude on self-similar coarsening with essentially invariant g. Kinetic Monte Carlo (KMC) simulation suggests $\varphi = 0.3$ as a threshold, with self-similar coarsening at larger φ and loss of connectivity at lesser φ [140]. Data exploring E_{eff} during a systematic variation of g in np Au, which could reveal the topology-dependence of the elasticity, has not been reported.

The approach to a genus-dependent scaling law for np Au starts out with matching f_{g} in Eq. 4.2 to the leveled-wave model. One may here compute the values of f_{g} as $E_{\text{eff}}/(\varphi^2 E_0)$, using Eq. 4.4 for E_{eff}. Together with Eq. 2.12 for $g(\varphi)$, the aforementioned expression for $f_{\text{g}}(\varphi)$ forms an implicit representation of the f_{g} versus g relation with φ as a parameter. This representation is shown as the solid line in Fig. 4.3.

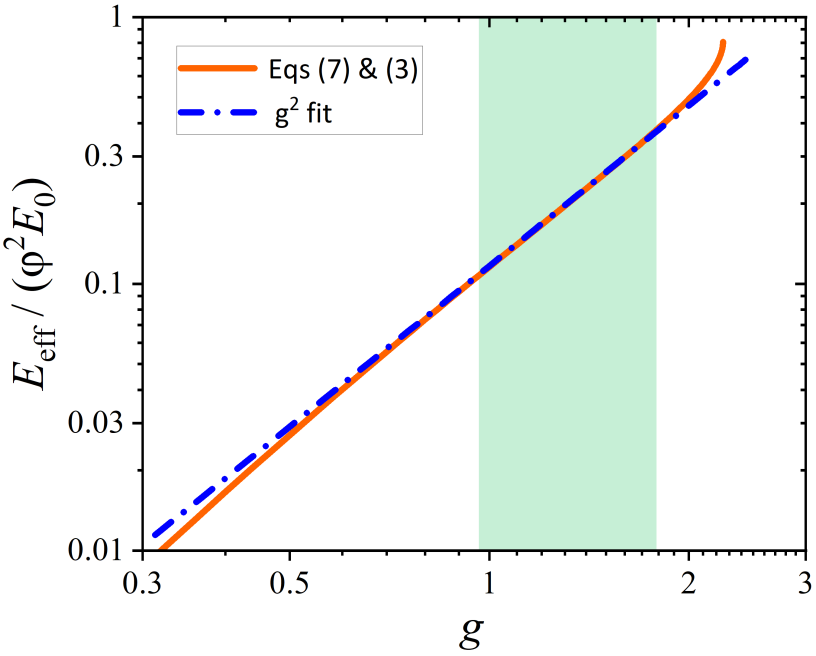

Figure 4.3: Topology-dependent scaling in the leveled-wave model. The function $E_{\text{eff}}/(\varphi^2 E_0)$, with Eq. 4.4 for E_{eff}, represents the elastic leading constant f_{g}. Solid line shows parametric graph of $f_{\text{g}}(\varphi)$ versus the solid-fraction- (φ-) dependent topological genus $g(\varphi)$ of Eq. 2.12 in the region $\varphi = 0.2-0.5$. Shaded: experimental region of interest as marked in Fig. 4.2. Dashed: fit with a quadratic g-dependence in that region.

Practically all experimental studies of np Au have φ in the range of $0.2-0.45$ and, as exemplified by our Fig. 4.2, their majority is in the even smaller interval of $0.25-0.37$, shaded in the figure. In Fig. 4.3, a linear fit (blue solid line) on logarithmic scales in the same interval (shaded) obtains $f_{\text{g}} = (g/2.88)^{2.04}$. This supports the aforementioned hypothesis of an essentially quadratic relation between f_{g} and g. Superimposed to the exact parametric plot, Fig. 4.3 shows a best fit with the quadratic law (dashed line), again for the same, experimentally most relevant, interval. In the region of interest, the fit, $f_{\text{g}} = (g/2.93)^2$, is seen to provide an excellent approximation to the parametric graph.

Applying the fit back to Eq. 4.2, the new scaling law reads

$$E_{\text{eff}} = \left(\frac{g}{g_0}\right)^2 \varphi^2 E_0 \tag{4.5}$$

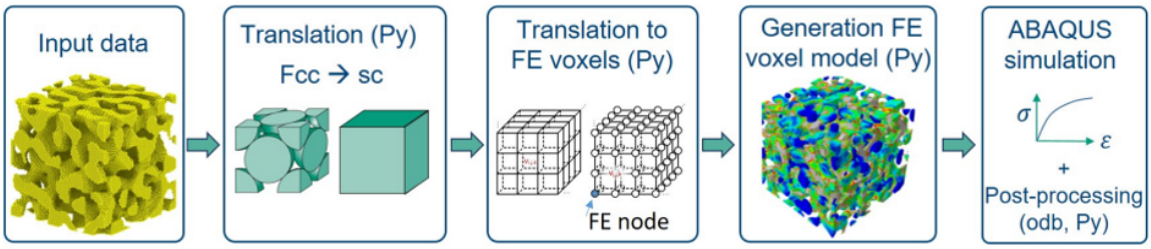

Figure 4.4: Workflow for the creation and simulation of an FE voxel model for leveled-wave structures, adapted from [184]. The input data for coarsened leveled wave structures is from the dataset in [193]. A translation from a face-centered-cubic (fcc) to simple-cubic (sc) grid allows creating cubic FE elements representing the individual solid voxels. Colors in the generated FE voxel model indicate the von Mises stress distribution as result of the numerical simulation of the model during compression in vertical direction. Homogenization delivers the macroscopic stress-strain behaviour, from which E_{eff} is derived in a postprocessing step.

with $g_0 = 2.93$.

Figure 4.2 shows the genus-dependent scaling law of Eq. 4.5 (using Eq. 2.12 for g of the leveled-wave model) superimposed to the literature data and to the scaling law of Eq. 4.4. The agreement with experiment is apparent.

One immediately sees that the new scaling law of Eq. 4.5 can be interpreted as a modified Gibson-Ashby law, with φ replaced by the effective solid fraction, φ_{eff}, of Eq. 4.3, in other words,

$$E_{\text{eff}} = \varphi_{\text{eff}}^2(g, \varphi) E_0 \,. \tag{4.6}$$

This confirms the speculation, based on the concept by Liu et al. [62] of an effective load-bearing solid fraction. For comparison, Fig. 5.1 inspects the linear g-scaling suggested in [137]. That scaling hypothesis does not provide a satisfactory fit to the data in Fig. 4.2. Further details can be found in Sec. 5.1.2.

4.1.2 Extension to networks with reduced connectivity

So far, the present analysis of the genus-dependent scaling rests exclusively on the leveled-wave model, where φ and g are inextricably coupled (Eqs 2.12 and 4.4). The constraint $g = g(\varphi)$ implies that the separation into the functions f_{g} and f_{φ} is not rigorous and requires independent support, conveniently in the form of data for networks with same φ but different g.

One approach to varying the connectivity of networks is the random cutting of the struts of a periodic lattice. A universal relation, independent of the coordination number of the perfect reference lattice, links E_{eff} to a suitably normalized total cut fraction or a suitably normalized scaled genus [65]. Yet, specifying a fraction of cuts or, alternatively, normalizing the scaled genus to the correct reference volume (correct choice of L in Eq. 2.8 for the reference structure), requires that a perfect reference structure is identified in the first place. That task is not obvious for random network structures, and specifically in experiment. Here, this work utilizes that coarsening of leveled-wave like structures, a process that is driven by curvature-driven surface diffusion, can change g while leaving φ sensibly constant.

A data set based on KMC simulations and exploring the change in connectivity of np Au during coarsening is reported in [140, 193]. The simulation accounts for surface excess energy as the driving force and for surface diffusion as the atomistic mechanism of microstructure evolution. That data provides samples with φ and g decoupled. Here, the 3D representations from that work is imported into FEM simulations. The details of the FEM methodology are provided in [183]. The workflow for computing E_{eff} is shown in Fig. 4.4 [184].

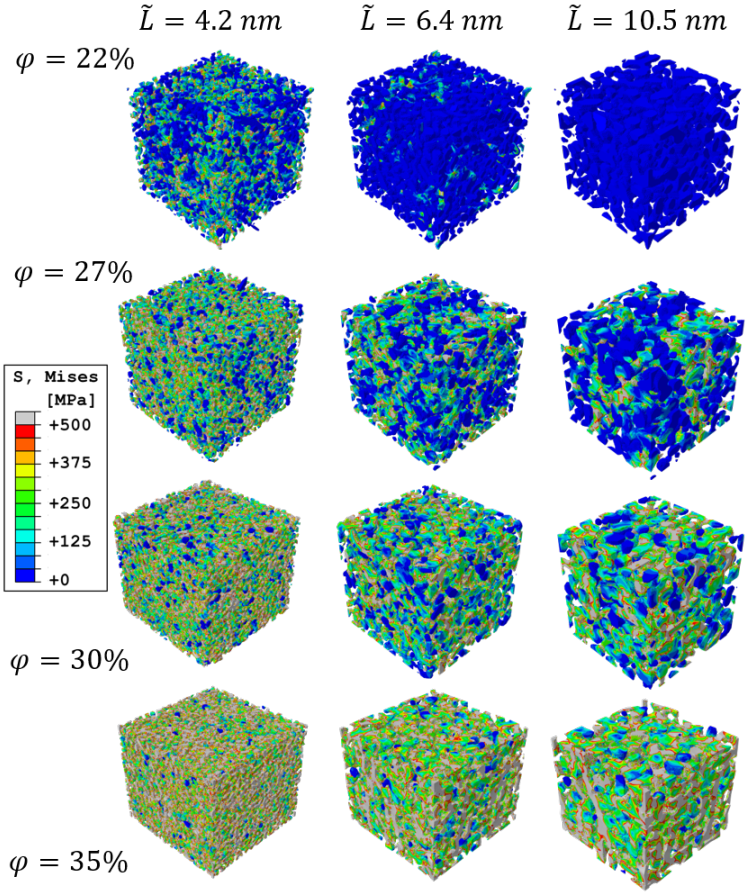

Figure 4.5: Load distribution in leveled-wave type structures visualized via elastic-plastic compression to 10% strain and its evolution during coarsening. Finite-element method results for local von Mises stress (legend). Rows: four samples of different solid fraction φ. Columns: as-generated and coarsened to characteristic spacing $\tilde{L}$ (legend).

Exemplary von Mises stress fields from the simulations are shown in Fig. 4.5. Blue designates stress-free regions. These regions are typically disconnected from the main load-bearing cluster. They can be seen to become more frequent in later stages of coarsening, specifically for structures with low φ. This illustrates the gradual disconnection upon coarsening.

For all structures of the coarsening simulation, Fig. 4.6 shows E_{eff}, normalized to the Gibson-Ashby prediction $\varphi^2 E_0$, versus g. Thus, as in Fig. 4.3, the ordinate displays f_{g}. Each symbol type in the figure represents a (numerical) sample with a given φ. Groups of symbols for each sample are connected by lines, following that sample's evolution

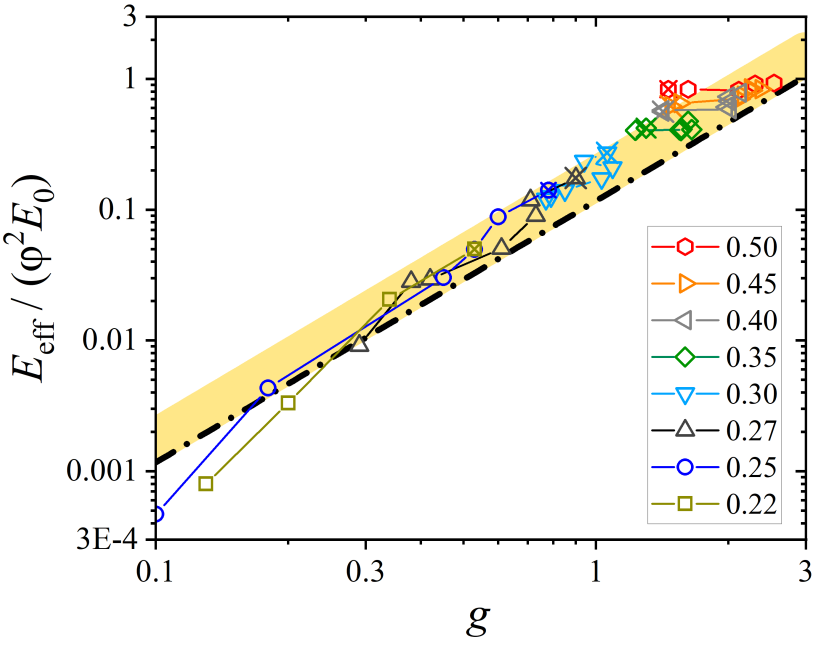

Figure 4.6: Analysis of connectivity scaling for effective Young's modulus, E_{eff}, of computer-generated structures with reduced connectivity. E_{eff} (normalized to the Gibson-Ashby prediction $\varphi^2 E_0$) is shown versus scaled genus, g. Data points: results from modeling of coarsened nanoporous gold. For solid fraction φ, see legend. Colored lines connect data points of structures with common φ, in sequence of increasing coarsening time. Initial structures are marked ×. Note log-log scaling. Dashed line: Eq. 4.5, with $g_0 = 2.93$ for the leveled-wave model. Shaded: confidence band with $g_0 = 2.40 \pm 0.50$.

during the coarsening. The initial state is marked × for each sample. By construction of the KMC simulation, each sample has constant φ during the entire coarsening.

Most samples in Fig. 4.6 exhibit an initial increase in g. This evolution does not imply new connections. Instead, it results from an error in computing $\tilde{L}$ of the as-generated structure. The error propagates into the computation of g by Eq. 2.8 and lets g initially be underestimated by up to ~ 40%. The problem is explained in [140] and the underlying issues are collected in Sec. 5.1.1.

During the later stages of the coarsening, Fig. 4.6 reveals distinct differences in the samples' behavior. Samples with high φ experience little change in E_{eff} during coarsening. By contrast, E_{eff} of the samples with low φ drops significantly as the coarsening proceeds, along with a drop in g. This may be understood as the signature of the loss in connectivity, as mentioned in the previous section, during coarsening of low-φ random microstructures.

Setting aside the artifact of the initial decrease in g, the central feature in Fig. 4.6 is that E_{eff} decreases with g in agreement with the g^2 scaling law of Eq. 4.5 (dashed line). In other words, the FEM results for microstructures in which g varies independently of φ support the proposed scaling law.

The shaded band in Fig. 4.6 contains all data points but ignoring the initial ones (for the reason outlined above) and the ones at extremely small g, where the stiffness starts to fall significantly below the g^2 scaling. The band represents $g_0 = 2.40 \pm 0.50$. It underlines that the data for the sample with varying connectivity is compatible with

our suggested scaling law, yet with g_0 about 20 % smaller than what was found for the as-prepared, non-coarsened leveled-wave structures of [66].

The different values of the E_{eff} in the two FEM studies (this work and [66]) may reflect differences in how the microstructure was discretized when setting up the models for the numerical analysis. In spite of the different g_0, the observations on the two different data sets are likely compatible with the identical underlying scaling law.

4.1.3 Fabrication of nanoporous niobium

The following three sections present results on np Nb, focusing on the experimental investigation of the mechanical and structural characteristics of nanoporous structures.

Chemical composition and phases before and after LMD

As described in Sec. 3.1, np Nb samples were prepared by dealloying the precursor alloy with a nominal composition of $Nb_{25}Ni_{75}$ (at%) in a liquid Mg bath. X-ray diffraction (Fig. 4.7(a)) shows peaks attributed to orthorhombic $NbNi_3$ in the precursor alloy. The X-ray powder diffractogramm from a fracture surface, Fig. 4.7(b), confirms complete through-bulk dealloying with predominant body-centered cubic Nb phase. The diffractogram shows weak reflections of NbO, an oxide species commonly formed when Nb is exposed to the atmosphere. The presence of this oxide layer on the acid-exposed, air-handled, and high-surface-area samples is consistent with niobium's natural tendency to form a ≤ 1 nm of thermodynamically stable NbO layer upon air exposure, as extensively documented in [194]. It is also known that Nb_2O_5 layer may slowly develop over time. In this study, Nb_2O_5 layer was not observed in freshly fabricated samples, and all characterizations including the X-ray diffraction were conducted within a day of fabrication.

The optical appearance of each sample is shown in the insets of Fig. 4.7(a-b). Nanoporous Nb retains the precursor's geometry, with no visible macroscopic cracks or shrinkage observed under the microscope, consistently reproduced in this study. The energy dispersive X-ray spectroscopy analysis finds 99.2 ± 0.7 at% Nb in the dealloyed sample; residual Mg and Ni were < 0.1 at% and 0.8 ± 0.8 at%, respectively. The element distribution maps corresponds to Fig. 4.7(c) can be found in Fig. 4.7(d-f).

Control of nanoporous Nb structure size

Figure 4.8 shows the SEM images of np Nb prepared under nine different dealloying conditions. The solid volume fraction of each of the nine samples tested is 0.36. For representative cross-sectional micrographs, the samples were sliced using a scalpel and their cross-sections were observed. Each sample is composed of a bicontinuous network of randomly oriented Nb ligaments. The ligament size and morphology showed no visible differences between the center and near-surface areas of the cross-sections, as displayed in Fig. 4.9. The figure shows two distinct regions on the cross-section of np Nb samples prepared at 850°C for 45 minutes and 900°C for 45 minutes as a representative. The ligament sizes in the central part of the cross-section and at the corner ($\sim 60\,\mu$m from the exterior surface) are comparable.

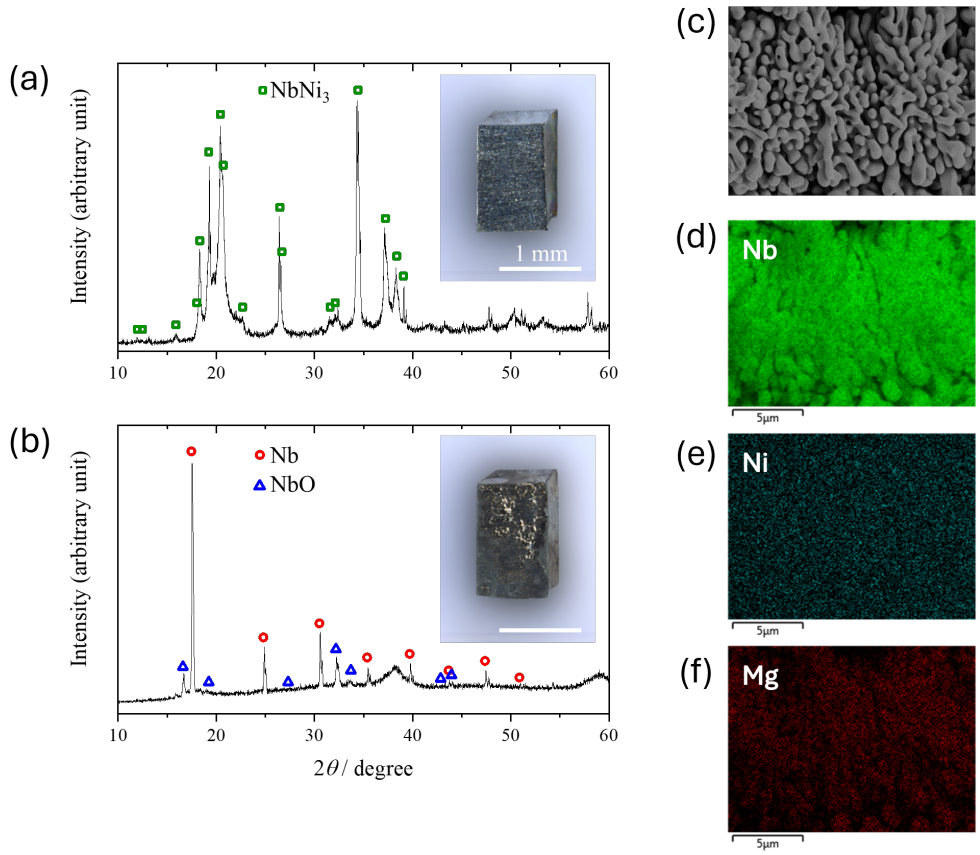

Figure 4.7: X-ray diffraction patterns and optical images of (a) a precursor alloy with a nominal composition of $Nb_{25}Ni_{75}$ (at%) and (b) nanoporous Nb prepared by liquid metal dealloying at 850°C for 45 minutes. Markers indicate reflection positions of reference patterns for various crystal structures, see legends. (c) SEM micrograph of a nanoporous Nb dealloyed at 850°C for 45 minutes. Elemental mapping of (c) for (d) Nb, (e) Ni, and (f) Mg by energy dispersive X-ray spectroscopy.

Ligament sizes were determined from SEM micrographs, measuring ligament diameters near their center as exemplified by the arrow in Fig. 4.8. The mean ligament size, L, of individual samples ranges from a few hundred nm to $> 1\mu$m, depending on the dealloying conditions. Note the distinction between L and the mean ligament spacing, $\tilde{L}$, discussed in Sec. 2.3.4.

A noticeable trend can be seen when comparing the dealloying conditions presented in Fig. 4.8: smaller ligaments are produced at lower dealloying temperature and/or with shorter immersion time. As an example for sample-to-sample variation, the L of six samples prepared at 850°C for 30 minutes, including the one in Fig. 4.8, was 380 ± 60 nm. The minimum value of L that is reliably reproduced in this work was ~ 400 nm obtained at 800°C for 30 minutes. Below this temperature or with a shorter duration, the structure remains dense with a substantial amount of residual Ni.

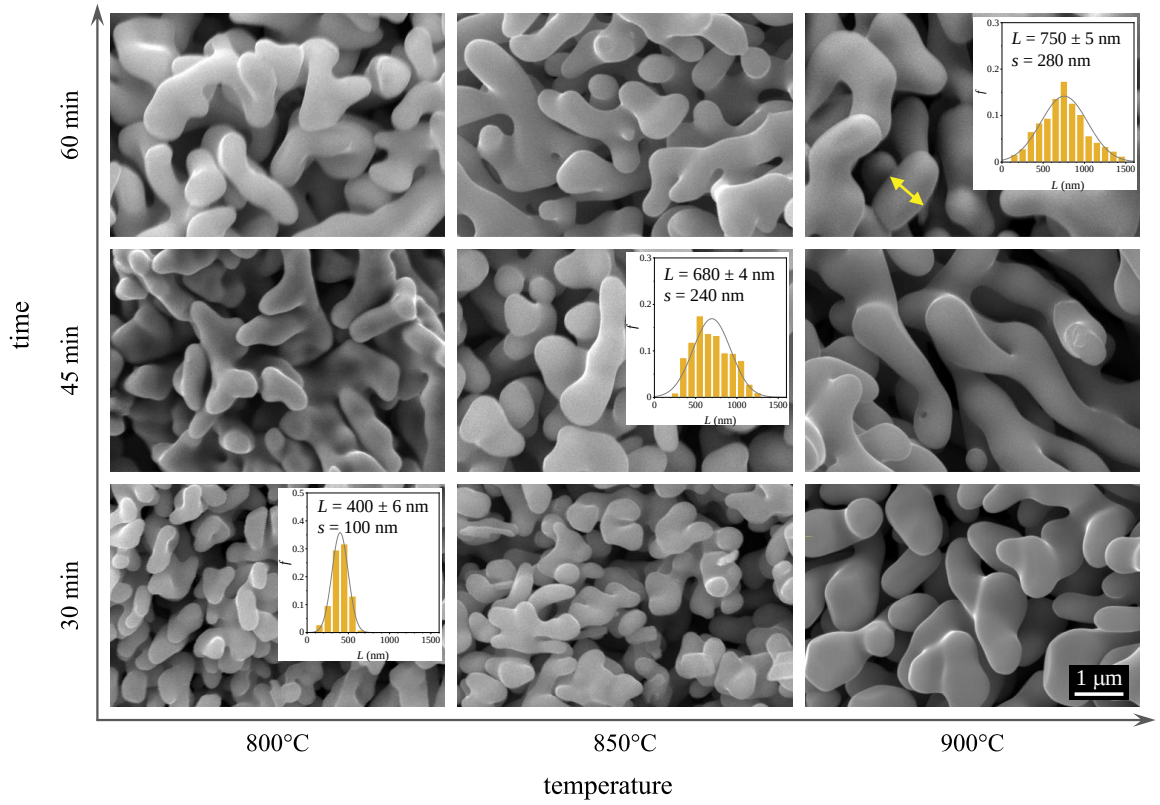

Figure 4.8: Scanning electron micrographs of nanoporous Nb dealloyed under nine different combinations of immersion time (see ordinate) and temperature (see abscissa) conditions. Insets show ligament size distribution histograms for selected conditions. L is the mean ligament size and s its standard deviation.

4.1.4 Mechanical properties of nanoporous niobium under compression

The combined analysis of mechanical properties and microstructures is now extended to nanoporous Nb produced via liquid-metal dealloying. Figure 4.10(a) presents the stress-strain graphs under compression, displayed as engineering stress, σ_{eng}, versus engineering strain, ε_{eng}. The graphs are from individual samples, prepared under three different dealloying conditions: 850°C for 30 minutes, 900°C for 60 minutes, and 900°C for 90 minutes, resulting in average ligament sizes of 320 ± 2, 690 ± 4, and 840 ± 3 nm with standard deviations of the ligament size distribution at 130, 320, and 420 nm, respectively.

The effective Young's modulus, E_{eff}, in different states of compression was determined as the secant modulus from the unload-reload segments in Fig. 4.10(a). Figure 4.11 provides an example of secant modulus determination with an enlarged view of a typical stress-strain curve. Figure 4.12 shows the φ-dependence of E_{eff} of np Nb scaled by the Young's modulus of massive Nb, $E_0 = 103\,\text{GPa}$ [195]. As compression progresses, the solid fraction increases with plastic strain. Figure 4.12 reflects this trend, where higher E_{eff} is observed with larger φ. Across the data groups for different ligament sizes in Fig. 4.12, the size dependency of E_{eff} is weak.

From the stress-strain curves, the yield strength, σ_{Y}, at 15% plastic strain is plotted

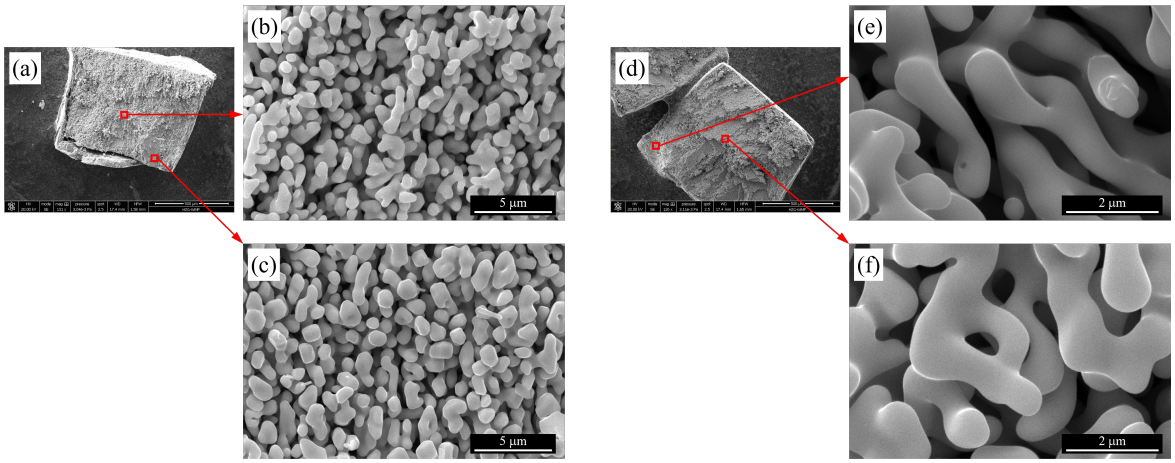

Figure 4.9: Ligament size comparison at two distinct locations on a sample cross-section. (a) Cross-section of a nanoporous Nb sample dealloyed at 850°C for 45 minutes. (b) Ligaments in the central area of (a). (c) Ligaments near the exterior surface of (a). (d) Cross-section of a nanoporous Nb sample dealloyed at 900°C for 45 minutes. (e) Ligaments in the central area of (d). (f) Ligaments near the exterior surface of (d).

in Fig. 4.13 as a function of L. Refer to Fig. 4.11 for an example of yield strength determination. The plastic strain level is chosen to approximate the as-dealloyed state while being within the range where any instrumental effects coming from the possible imperfections of the sample shape can be ruled out. Figure 4.13 shows that the yield strength is enhanced with smaller L, and the linear fit line is plotted together. This ligament size dependency is further discussed in Sec. 5.2.2 in connection with the crystal structure of Nb.

In Fig. 4.10(b)-(c), the structural change at $\varepsilon_{\text{eng}} = 0.4$ is displayed compared to the relaxed (as-dealloyed) network. The ligament spacing decreases, aligning with the expected outcome of plastic compression forming new contacts between neighboring ligaments. Mechanical failure occurred once the strain exceeded 0.4.

4.1.5 Scaled genus density of nanoporous niobium

Figure 4.14(a) shows an SEM image of a micro-pillar of np Nb for X-ray nanotomography. The porous structure is visible at the FIB-milled surface of the sample. Four samples were investigated in this way, with their dealloying conditions and $\tilde{L}$ values listed in Table 4.1. A cropped slice of a typical cross-sectional image of the pillar observed by tomography is shown in Fig. 4.15(a). The gray image is then binarized to Fig. 4.15(b), and the same process is applied to all slices of the pillar. Figure 4.14(b) is the binarized reconstruction of the micro-pillar in 4.14(a). The porous structure closely resembles that seen in the SEM image. For further analysis, a $> 1\mu$m outer surface layer is cropped out. This minimizes any effects arising from the FIB-curtained surface, while the column volume remains sufficient to be representative.

The structure is then skeletonized, emphasizing the connectivity between the ligaments. Figure 4.14(c) illustrates an example of two individual rings observed within the pillar. The scaled genera obtained from the experimental tomographic reconstructions are displayed in Fig. 4.14(d), with the $\varphi - g$ relation for the leveled-wave model [66] su-

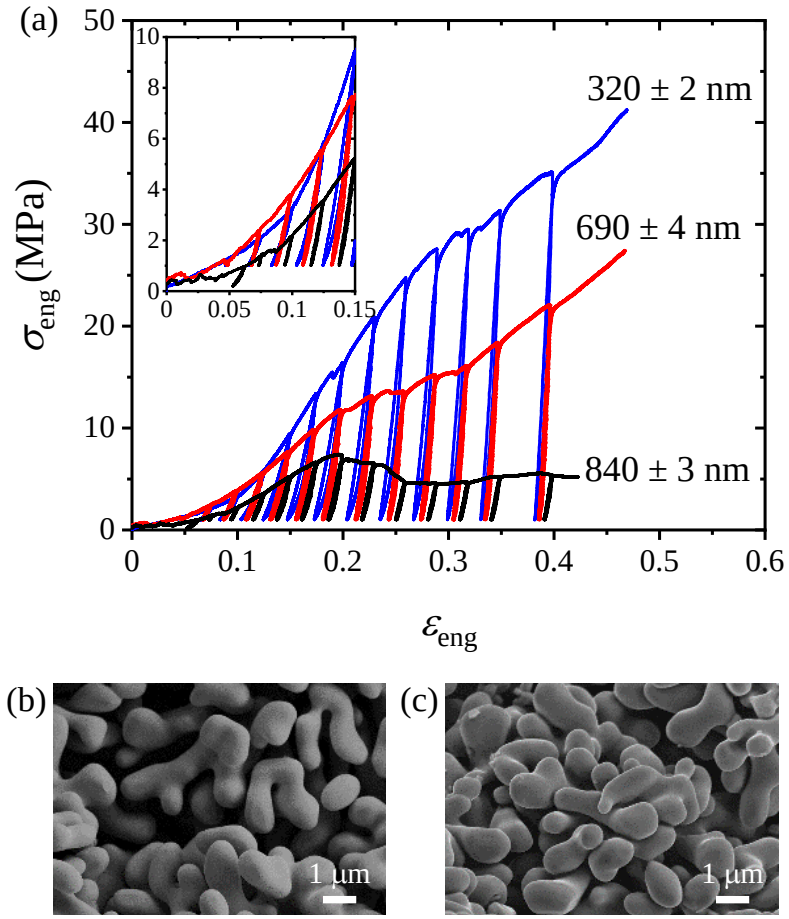

Figure 4.10: (a) Stress-strain curves of nanoporous Nb samples with three different mean ligament sizes. The inset shows the curves at the low strain level. SEM images of nanoporous Nb with (b) $\varepsilon_{eng} = 0$ and (c) $\varepsilon_{eng} = 0.4$ of compression. In (b) and (c), the nanoporous Nb is dealloyed at 900°C for 90 minutes.

Table 4.1: Dealloying conditions and the mean ligament spacing, $\tilde{L}$, determined by X-ray nanotomography. T is the temperature of Mg melt and t is the immersion time.

T [°C]	t [min]	$\tilde{L}$ [μm]
800	45	1.46
850	30	1.52
850	30	1.76
900	60	1.37

perimposed for comparison. Figure 4.14(e) complements that graph with a display of g versus $\tilde{L}$. It is seen that the sample set explores essentially a single φ value and a quite narrow range of $\tilde{L}$. This prevents substantiated conclusions on how g correlates with those parameters. For further discussion, only the average value, g_{avg}, is considered.

From the set of samples listed in Table 4.1, it is found that $g_{avg} = 1.21 \pm 0.15$. As

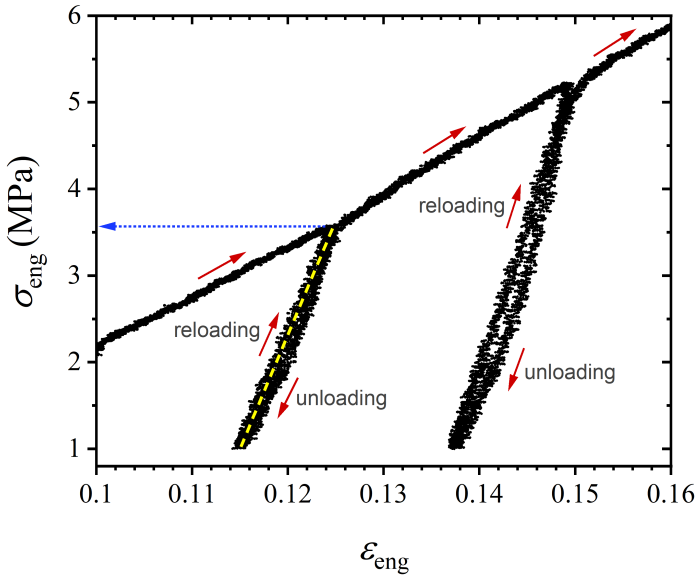

Figure 4.11: Determination of Young's modulus and yield strength from an unload-reload segment of a stress-strain curve. The red arrows indicate the direction of compression progress. The slope of the yellow dashed line represents the secant modulus. The blue dotted arrow indicates the yield strength at a corresponding plastic strain level.

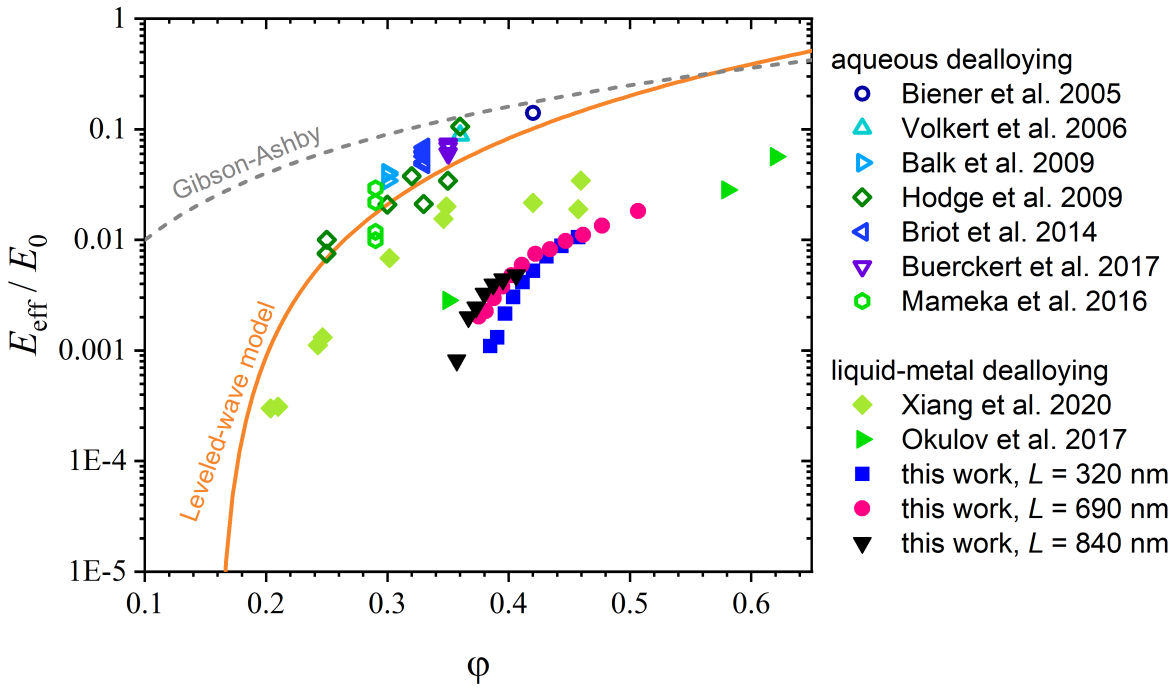

Figure 4.12: Scaled Young's modulus of nanoporous Nb (this work) and other reported porous materials produced by liquid-metal dealloying [72, 74] (closed symbols), and of nanoporous Au produced by aqueous dealloying [52, 54, 82, 107, 189–191] (open symbols). All data points are scaled by the Young's modulus of base material, E_0. The modified Roberts-Garboczi scaling law for the leveled wave model [66] and Gibson-Ashby scaling law [59] are displayed for reference.

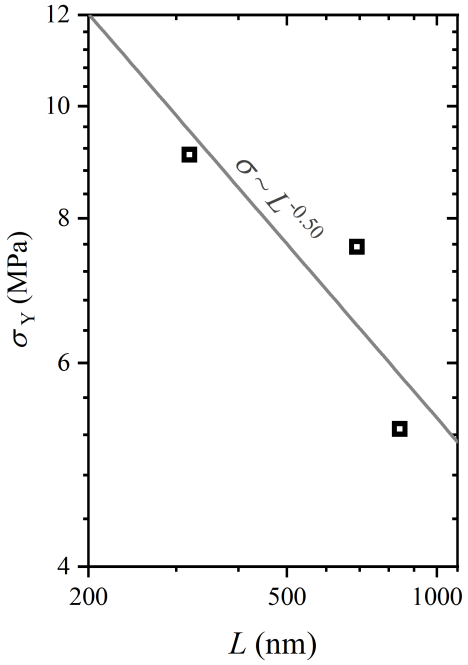

Figure 4.13: The yield strength, σ_Y, of nanoporous Nb versus ligament size, L, at ε_{eng} = 0.15. The straight line indicates $\sigma \sim L^{-0.50}$ with arbitrary prefactor.

compared to the leveled-wave model at the same solid fraction, the g_{avg} of np Nb is less by the factor of ~ 1.5. Since the leveled wave model is considered as an adequate description of np Au, it can be concluded that the network structure of np Nb is less connected than that of np Au.

4.2 Hydrogen interaction dynamics in nanoporous palladium

4.2.1 Microstructure and compositional properties of nanoporous palladium

Chemical composition of nanoporous Pd

Following the preparation steps in Sec. 3.2, crack-free np Pd samples were successfully prepared. Figure 4.16 presents an SEM image of a typical fracture surface along with its energy dispersive X-ray spectroscopy spectrum. Quantitative measurements on four independent samples and at least two positions in each sample reveal a residual Cu content of 3.9 ± 0.6 at%. The morphologies of the ligaments on the fracture surfaces are depicted in the SEM micrographs of Fig. 4.17.

Ligament size upon thermal coarsening

In Fig. 4.17(a), the ligaments of as-dealloyed np Pd exhibit a hierarchical structure, characterized by nanoscale ligaments containing even smaller pores. Figures 4.17(b) and (c) illustrate the effects of thermal coarsening at 300°C and 400°C, respectively.

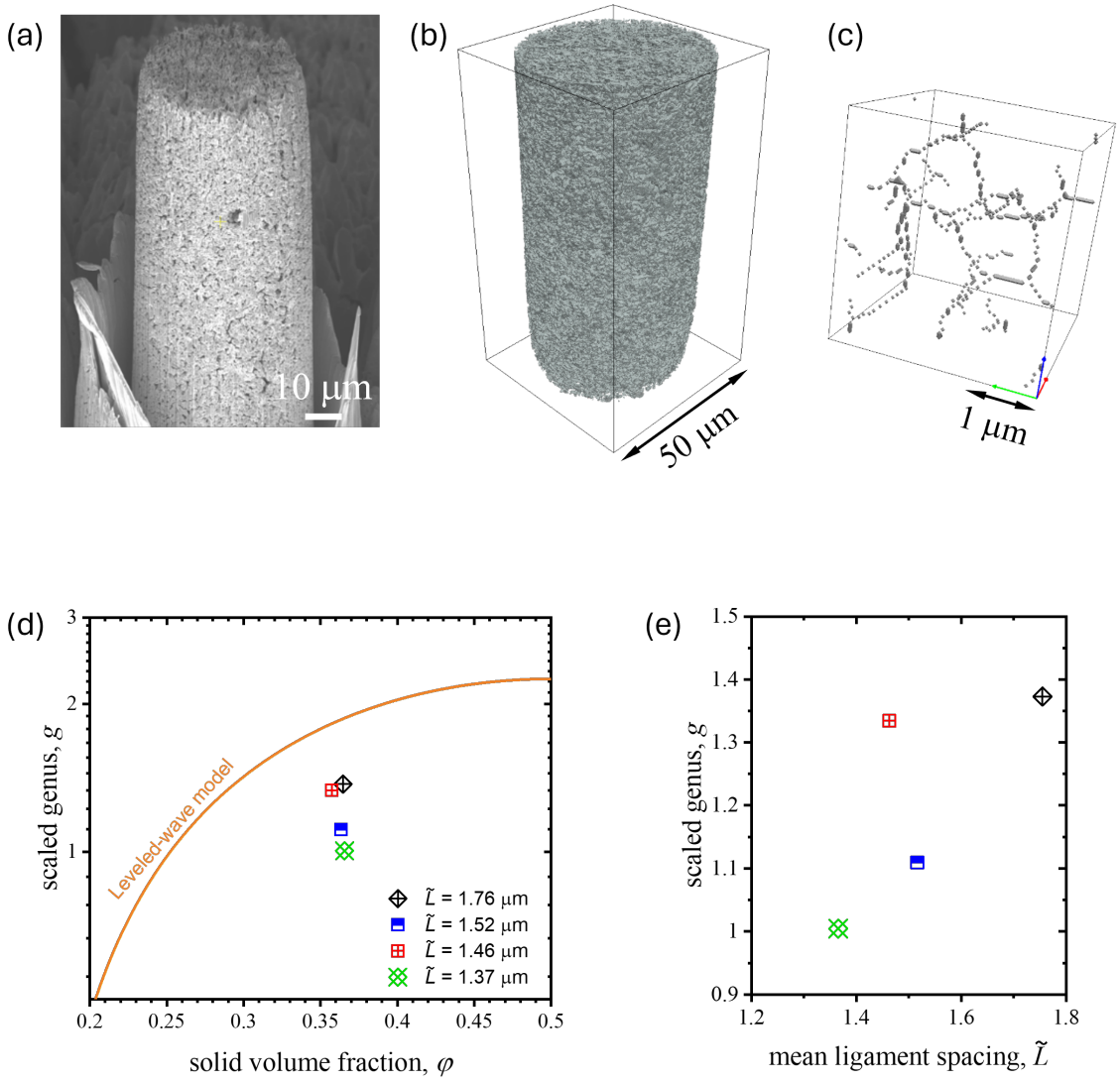

Figure 4.14: (a) SEM image of a nanoporous Nb micropillar and (b) its X-ray nanotomography-based 3D reconstruction. Note that the sample has been rotated by an arbitrary angle, providing a different perspective from (a). (c) Skeletonized structure of (b), cropped to contain two continuous rings. (d) Scaled genus, g, versus solid fraction, φ. A skin layer–possibly FIB-affected–has been removed for the g calculation. Solid line: leveled-wave model [66]. (e) g versus the mean ligament spacing, $\tilde{L}$, of the four nanoporous Nb micropillars.

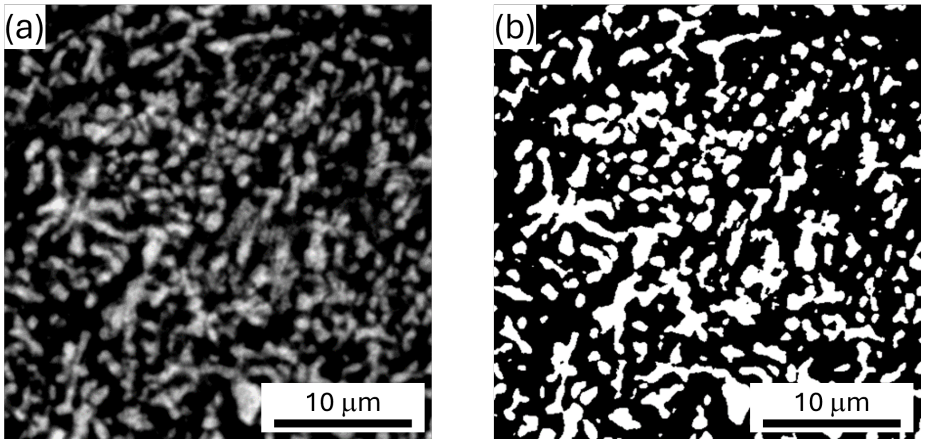

Figure 4.15: Typical cross-sectional images of nanoporous Nb observed by X-ray nanotomography. (a) Before and (b) after binarization.

The samples are exposed to elevated temperatures for 5 minutes, as described in Sec. 3.2.4. The hierarchical structure is eliminated after thermal annealing, resulting in monomodal porous structure with coarsened ligaments. The average ligament sizes are measured by randomly selecting at least 30 ligament diameters from each micrograph. The as-dealloyed sample (Fig. 4.17(a)) displays two distinct ligament sizes, with average diameters of 32 ± 13 nm for the larger ligaments and 11 ± 4 nm due to the smaller pores. This increases to 55 ± 15 nm and 106 ± 28 nm upon thermal coarsening at 300°C and 400°C, respectively (Fig. 4.17(b,c)). With the same duration of heat treatment, the resulting ligament sizes increase at higher temperatures, consistent with previous observations [167].

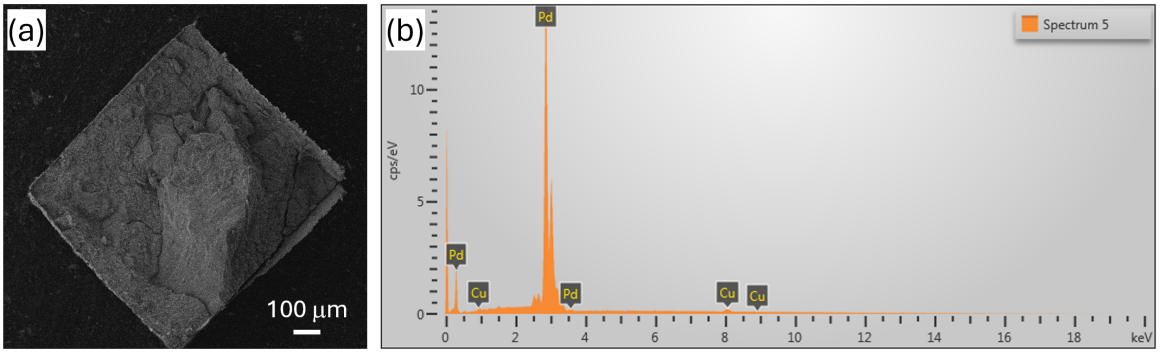

Figure 4.16: (a) Scanning electron micrograph of a typical nanoporous Pd fracture surface. (b) Corresponding energy dispersive X-ray spectroscopy spectrum from a scan area of ~ 71 × 94 μm on the fracture surface, showing ~ 97 at.% Pd and ~ 3 at.% Cu.

Determination of electrochemically active surface area

The electrochemically active surface area, A of the np Pd samples was obtained from cyclic voltammetry (CV) measurements following the procedure described earlier in [167, 196]. The resulting cyclic voltammograms for np Pd samples with different ligament sizes are shown in Fig. 4.18(a), displaying the influence of ligament size variation.

Practically, the CV plots can be divided into three regions from left to right: (1) hydrogen ad/absorption and desorption at potentials below $E_{\mathrm{SHE}} \sim 0.34\,\mathrm{V}$, (2) capacitive charging/discharging of the double layer with a relatively low current; and (3) oxygen species adsorption and desorption at potentials above $E_{\mathrm{SHE}} \sim 0.60\,\mathrm{V}$. Figure 4.18(b) highlights the area under the OH desorption peak. This area under the curve corresponds to the charge, Q, required to reduce a monolayer of PdO:

$$Q = \int_0^t i\,dt = \left(\frac{dE}{dt}\right)^{-1} \int_0^t i\,dE \tag{4.7}$$

where t is time, i is the current, and $\frac{dE}{dt}$ is the scan rate which is 10 mV/s for the data shown in Fig. 4.18. This charge is then translated into the active surface area, using Q^*, the charge needed to reduce PdO monolayer per unit area of Pd:

$$A = \frac{Q}{Q^*} \tag{4.8}$$

with $Q^* = 420\,\mu\mathrm{m/cm^2}$ for Pd [197]. The resulting mass-specific surface areas are $4.10\,\mathrm{m^2/g}$, $3.40\,\mathrm{m^2/g}$, and $1.73\,\mathrm{m^2/g}$ for np Pd samples with mean ligament sizes of $\sim 34\,\mathrm{nm}$, $\sim 54\,\mathrm{nm}$, and $\sim 121\,\mathrm{nm}$, respectively. These active surface area values are later utilized in the area-specific capacitance analysis in Sec. 4.2.5.

4.2.2 Hydrogen solubility isotherms of nanoporous palladium

The hydrogen fraction, x_{H}, is defined as the ratio between the number of moles of palladium and hydrogen in an np Pd sample. The molar quantity of each component is determined from the mass of hydrogen-free np Pd and the electric charge measured by the potentiostat, respectively. As described in Sec. 3.3.5, the chronoamperometry technique was employed to let the sample alternate between the hydrogen-free state ($E_{\mathrm{SHE}} = 380\,\mathrm{mV}$) and a charged state. For each charging and discharging potential, the current and charge responses were recorded over sufficient time until either the current reaches zero or the simultaneous dilatometer signal saturates. A measurement duration of 600 s was sufficient to achieve this steady-state condition for transitions between the hydrogen-free state and the α phase at $E_{\mathrm{SHE}} \geq 60\,\mathrm{mV}$, while 2000 s was required to

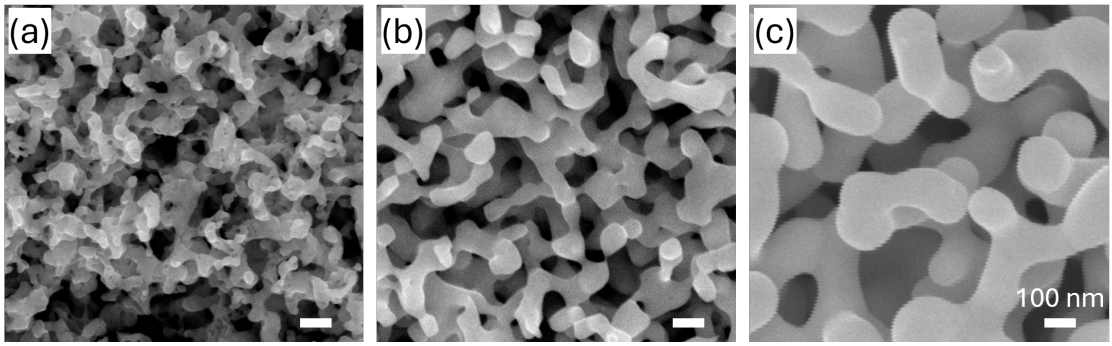

Figure 4.17: SEM images of microstructure on the fracture surfaces of nanoporous Pd (a) after dealloying and electrochemical reduction, (b) after thermal coarsening at 300°C for 5 minutes, and (c) at 400°C for 5 minutes.

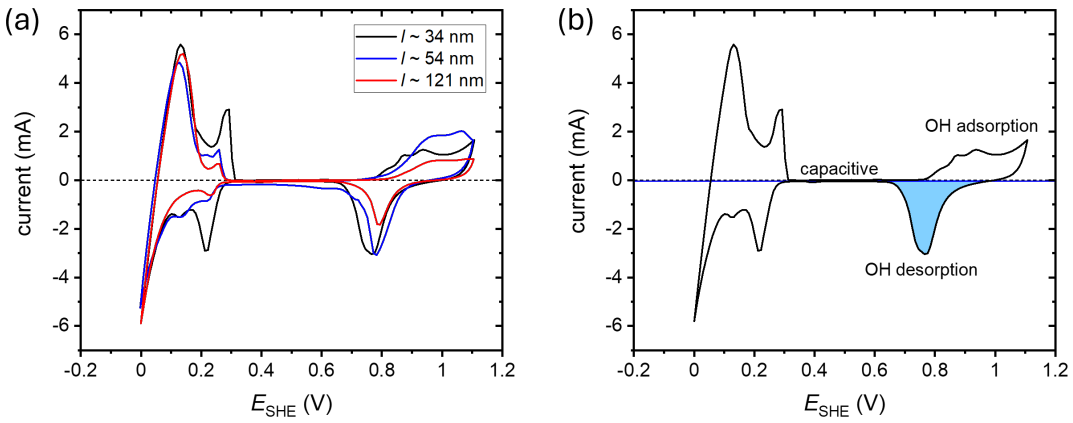

Figure 4.18: (a) Cyclic voltammogram of nanoporous Pd with ligament sizes of ~ 34 nm, ~ 54 nm, and ~ 121 nm in 1.0 M H_2SO_4 at a scan rate of 10 mV/s and room temperature. (b) Cyclic voltammogram of nanoporous Pd with ligament sizes of ~ 34 nm from (a), with the oxide peak shaded in blue. The blue horizontal solid line indicates the capacitive current level.

ensure the steady-state for transitions involving the α' phase at $E_{\mathrm{SHE}} \leq 30\,\mathrm{mV}$. Near the phase transition point, $30\,\mathrm{mV} < E_{\mathrm{SHE}} < 60\,\mathrm{mV}$, each measurement was conducted for 4000 to 18000 s to ensure steady state conditions are reached. A uniform time step of 1 s was used for all measurements.

The charge measured during the desorption process, Q_{de}, is used instead of the absorption/adsorption process to reduce interference from the hydrogen evolution reaction at the cathode. To further improve accuracy, the underpotential deposition charge, Q_{UPD}, is subtracted from Q_{de} to exclude contributions from surface-adsorbed hydrogen. Therefore, the bulk hydrogen fraction of np Pd is

$$x_{\mathrm{H}} = \frac{(Q_{\mathrm{de}} - Q_{\mathrm{UPD}})/F}{n_{\mathrm{Pd}}}\,. \tag{4.9}$$

where F is the Faraday constant and n_{Pd} is the mole number of Pd atoms. The net hydrogen fraction for three different ligament sizes at each potential is plotted as isotherm curves in Fig. 4.19. For all samples and phases, the hydrogen fraction increases with decreasing potential, undergoing a phase transition at $E_{\mathrm{SHE}} = 47 - 49\,\mathrm{mV}$ and reaching a maximum of $x_H = 0.71 \pm 0.01$ near $E_{\mathrm{SHE}} = -50\,\mathrm{mV}$. Figures 4.19(a) and (c) show detailed plots of the α and α' phases. Visually, there are several data points from the smaller ligament sample (black circles) which exhibit higher hydrogen solubility in the α phase, whereas the opposite trend is observed in the α' phase. However, upon closer inspection using the Mann–Whitney U test [198], performed pairwise between the samples, it was revealed that the p-values range from 0.49 to 0.87, greater than the conventional threshold of 0.05. This indicates that there are no statistically significant differences between the samples. The test was conducted for each pair of samples in each phase range shown in Figures 4.19(a) and (c), except for the α' phase for the sample with $l \sim 185\,\mathrm{nm}$ (red squares), due to a lack of data points.

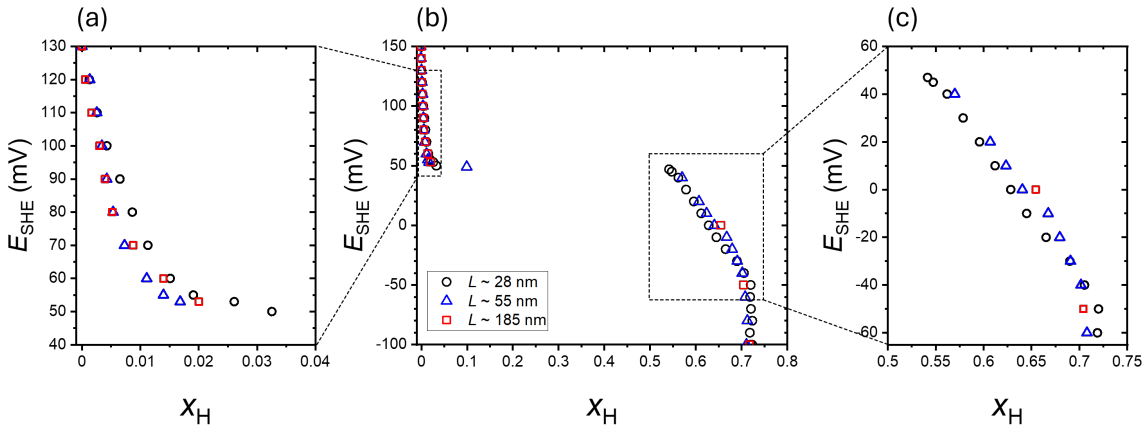

Figure 4.19: Sorption isotherms of nanoporous Pd with three different ligament sizes at room temperature, showing electrode potential versus the hydrogen molar ratio, x_H. Enlarged plots of (b) are shown in (a) and (c).

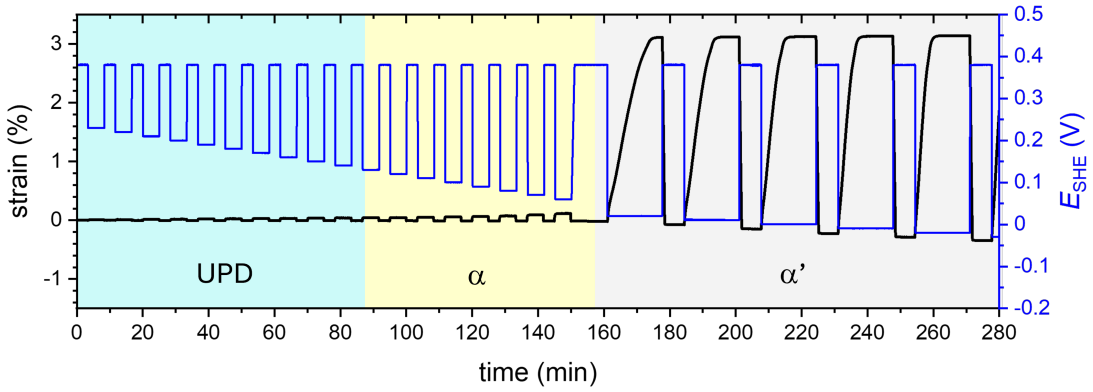

Figure 4.20: Strain response of a nanoporous Pd with $l \sim 28\,\text{nm}$ under step-wise potential switching between the hydrogen-free state at $E_{SHE} = 380\,\text{mV}$ and the charging potential of interest. The shade indicates the underpotential deposition (UPD), α, and α' phase regions based on the charging potential.

4.2.3 Hydrogen-assisted actuation of nanoporous palladium

Hydrogen-induced strain response

Hydrogen absorption in a Pd crystal causes lattice expansion, resulting in a measurable macroscopic length change. The strain response, therefore, indicates hydrogen charging and serves as the actuation mechanism of np Pd-H. Figure 4.20 shows a series of strain response of an np Pd sample monitored in-situ by a dilatometer under stepwise potential changes. The hydrogen-free state at $E_{SHE} = 380\,\text{mV}$ is used as a reference. The sample is repeatedly charged with hydrogen by applying a potential of interest–lower than 380 mV–and then discharged to the reference state. The time-dependent strain response at each potential level is recorded until strain becomes constant and the current reaches zero, indicating that equilibrium is reached. For all charging cycles, hydrogen charging causes sample expansion, while hydrogen unloading returns it to its

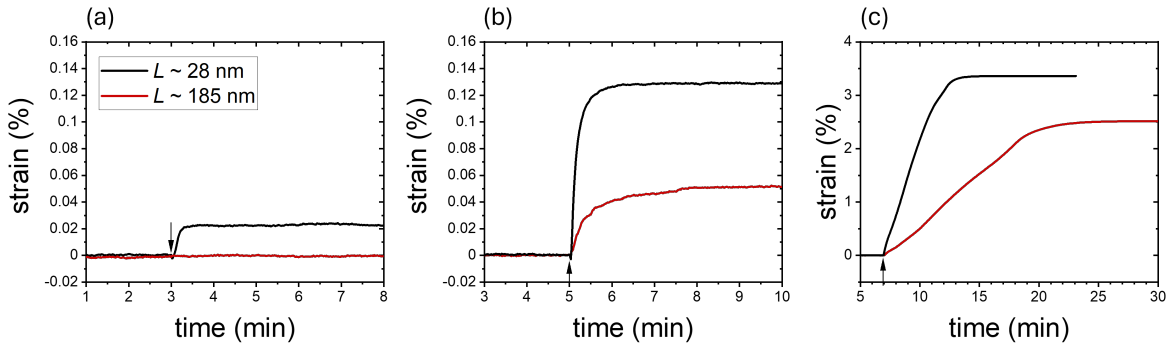

Figure 4.21: Strain responses of nanoporous Pd with ligament sizes of ~ 28 nm (black) and ~ 185 nm (red). The onset of the charging potential is indicated by an arrow. Prior to this onset, the sample is in a hydrogen-free state and the charging potentials are (a) E_{SHE} = 200 mV, (b) 60 mV, and (c) 0 mV.

original length. At set potentials of 50 mV < E_{SHE} < 130 mV, the sample is in the α phase, dilute solute solution, and at E_{SHE} < 49 mV, it enters the α' phase, concentrated solute solution. This phase transformation is visible by the magnitude of the saturated strain, with a maximum strain of 3.79 % observed in the α' phase.

As reported earlier [167], more than 100 cycles of loading and unloading have been performed without any observable degradation of the sample, demonstrating the material's durability as an actuator.

Ligament size effect on hydrogen-induced strain response speed

The effect of ligament size on hydrogen loading speed was investigated by comparing samples with two different ligament sizes: 28 ± 7 nm and 185 ± 35 nm, where the latter being more than six-fold larger than the former. Figure 4.21 shows loading strain curves at three representative potential values corresponding to each phase: np Pd with underpotentially-deposited (UPD) hydrogen at E_{SHE} = 200 mV, α phase at E_{SHE} = 60 mV, and hydride α' phase at E_{SHE} = 0 mV.

In the UPD regime (Fig. 4.21(a)), np Pd with L = 28 ± 7 nm exhibits a measurable strain of 0.02 %, whereas the sample with L = 185 ± 35 nm shows minimal to imperceptible strain response. This is consistent with previous observations [199] that UPD strain arises purely from surface stress caused by hydrogen on the surface. The strain effect is therefore less pronounced for larger ligaments due to the lower specific surface area. In the α and α' phases (Fig. 4.21(b,c)), which involve bulk hydrogen absorption, both samples demonstrate a measurable strain. In both phases, the sample with L = 185 ± 35 nm demonstrates a noticeably slower response compared to the sample with L = 28 ± 7 nm. The half time, defined as the time required to reach half of the maximum strain, is plotted in Fig. 4.22 for each E_{SHE} levels. This observation suggests that larger ligament size inherently slows down the hydrogen actuation response. For the sample with L = 28 ± 7 nm, the results are quantitatively comparable to [167]. The underlying mechanisms responsible for this limited kinetics are discussed in Sec. 5.3.3 and Sec. 5.3.4.

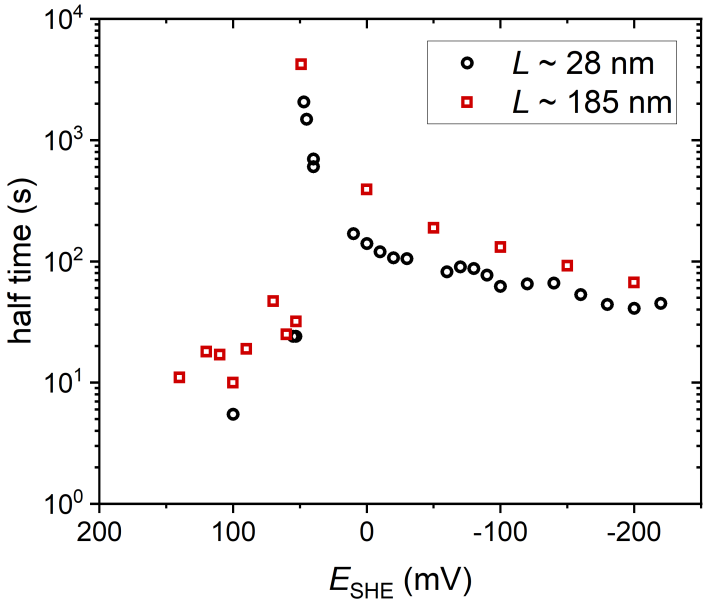

Figure 4.22: Half time of hydrogen charging for nanoporous Pd with ligament sizes of ~ 28 nm (black) and ~ 185 nm (red) at varying charging potentials, E_{SHE}.

4.2.4 Electrochemical impedance spectroscopy on nanoporous palladium

To investigate the reactions involved in interfacial kinetics and transport behavior, electrochemical impedance spectroscopy (EIS) is performed on np Pd samples. Initially, a DC electric potential, E_{DC}, measured against the SHE, is applied to the working electrode until equilibrium is reached in the sample, allowing for identification of the phase within the Pd-H system. Then, a sinusoidal perturbation of AC potential wave with known amplitude, ΔE, and frequency, f, is superimposed on the DC signal. The resulting current is observed as output signal. As described in Sec. 3.3.5, the amplitude is fixed at a relatively small value, and the impedance of the system is monitored at each frequency value.

Influence of perturbation amplitude

The amplitude of the perturbation signal, ΔE, should be sufficiently small to maintain the linearity of the system while still being large enough to ensure a reliable signal-to-noise ratio. An excitation voltage amplitude in the range of 5 to 10 mV is commonly used [179]. Figure 4.23(a) presents impedance measurement data for two cases: ΔE = 5 mV and ΔE = 10 mV. The results for the two perturbation amplitudes are identical, indicating that a perturbation amplitude of 5 mV is adequate for the EIS measurement.

The linearity of the system is further confirmed by examining the Lissajous plot, as illustrated in Fig. 4.23(b). The symmetric shape of the Lissajous plot at a perturbation amplitude of 5 mV implies that the system is time-invariant and operates linearly. Consequently, subsequent measurements are conducted using a perturbation amplitude of 5 mV.

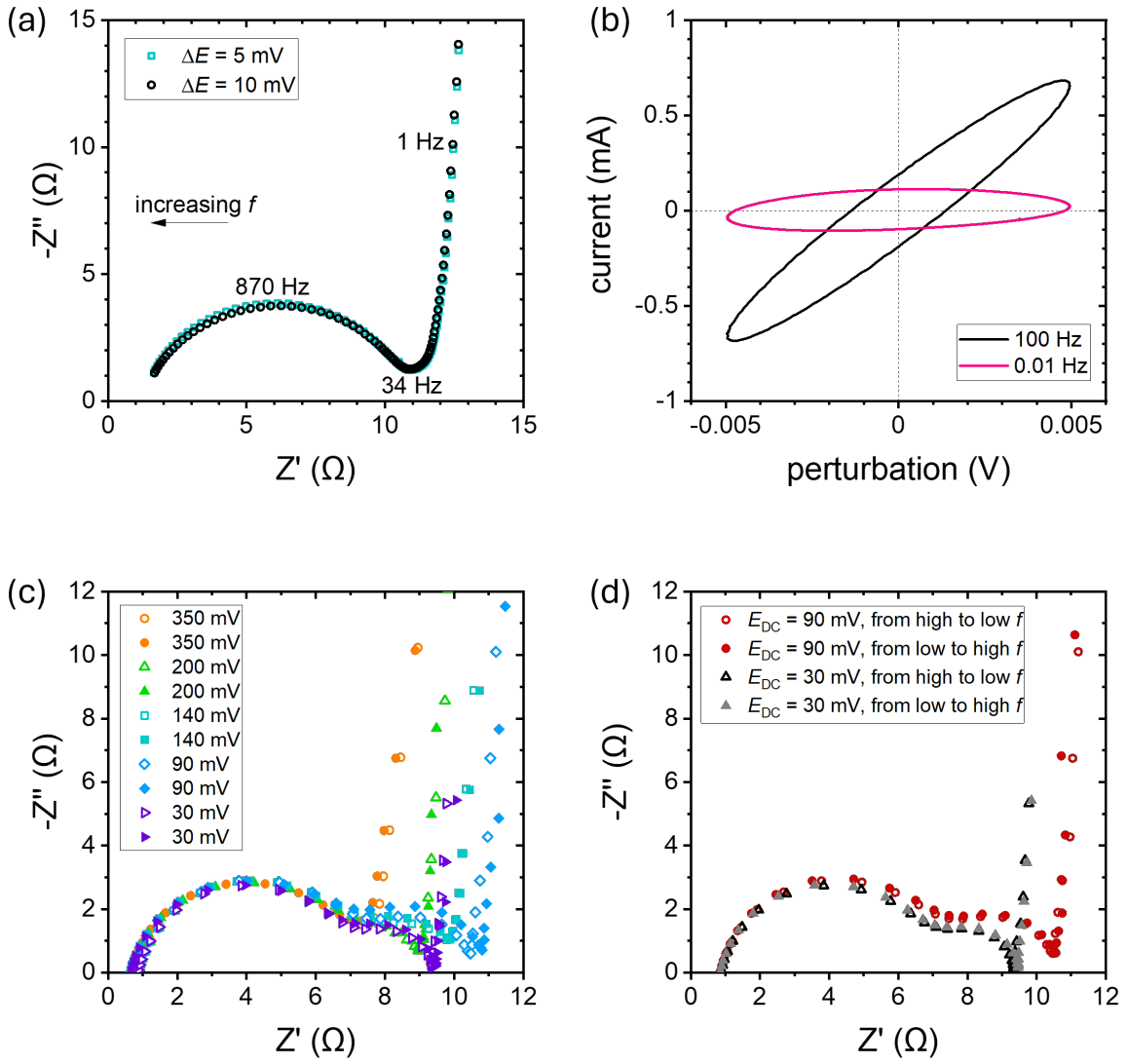

Figure 4.23: (a) Impedance spectra of nanoporous Pd with ΔE = 5 mV and 10 mV at E_{DC} = 350 mV. (b) Lissajous plots at E_{DC} = 90 mV and ΔE = 5 mV, shown for two different frequencies: 100 Hz and 0.01 Hz. (c) Impedance spectra from an increasing sequence of E_{DC} (open symbols) and a decreasing sequence of E_{DC} (closed symbols). (d) Impedance spectra for frequency scanning from highest to lowest (open symbols) and lowest to highest (closed symbols). ΔE = 5 mV for all measurements in (b-d).

Influence of DC potential scanning direction

The repeatability of the measurement is assessed by sweeping the DC voltage, E_{DC}, in two opposite directions. Impedance measurements are recorded at E_{DC} = 30, 90, 140, 200, 350 mV in both increasing and decreasing sequences. The frequency scanning direction is consistently descending with logarithmically uniform steps for all measurements. The results are shown in Fig. 4.23(c). The impedance data obtained from both sequences are identical, indicating that the system's response is independent of its prior hydrogen charging state and solely dependent on the potentiostatic control of the input signal.

Influence of frequency scanning direction

Another practical consideration to check the causality and the stability of the system is the effect of the prior excitation frequency, i.e., the frequency sweeping direction. At a fixed DC potential, the frequency is swept in both ascending and descending orders, with logarithmically uniform steps. The impedance data measured from both seqeunces at four different E_{DC} values are presented in Fig. 4.23(d). The E_{DC} values are selected to cover both α and α' phases. As shown in the plots of Fig. 4.23(d), the direction of the frequency sweep did not produce any noticeable differences in the impedimetric data. Combined with the findings from the previous sections, this confirms that the system meets the assumptions of a linear time-invariant system.

4.2.5 (Pseudo)capacitance and time constants in nanoporous palladium-hydrogen system

Electrochemical impedance spectroscopy (EIS) was conducted on np Pd samples with three different ligament sizes: (1) $L = 34 \pm 7$ nm, (2) $L = 54 \pm 10$ nm, (3) and $L = 121 \pm 2$ nm. The first sample exhibits a hierarchical structure with an additional lower ligament size level of 11 ± 3 nm. The aim is to investigate the influence of ligament size on the hydrogen charging process. The impedance data encompass conditions ranging from the hydrogen-free state ($E_{\mathrm{DC}} = 380$ mV) to the saturated α' phase, across a frequency spectrum of 10^{-2} Hz to 10^{5} Hz.

Figures 4.24(a) and (b) present Nyquist plots (complex plane plots) illustrating the complex impedance of np Pd samples with two distinct ligament sizes. Figures 4.24(c) and (d) provide an enlarged view of Figures 4.24(a) and (b), respectively, highlighting finer details of the high-frequency region. Each spectrum can be characterized by three distinct parts, from high to low frequency: at most two well-resolved semicircles and nearly linear section, closely parallel to a vertically straight line. The first group of semicircles, referred to as Group 1, appears in the high frequency range (approximately $f > 10^2$ Hz) and overlaps for all the tested DC voltages, E_{DC}. In contrast, the second set, Group 2, emerges in the intermediate frequency range only when the E_{DC} is below the transition point to UPD, and it varies with changes in E_{DC}. Finally, the nearly vertical line at the lowest frequency range corresponds to an–almost entirely–imaginary impedance. The physical origin and significance of each feature is discussed in more detail in Sec. 5.3.3.

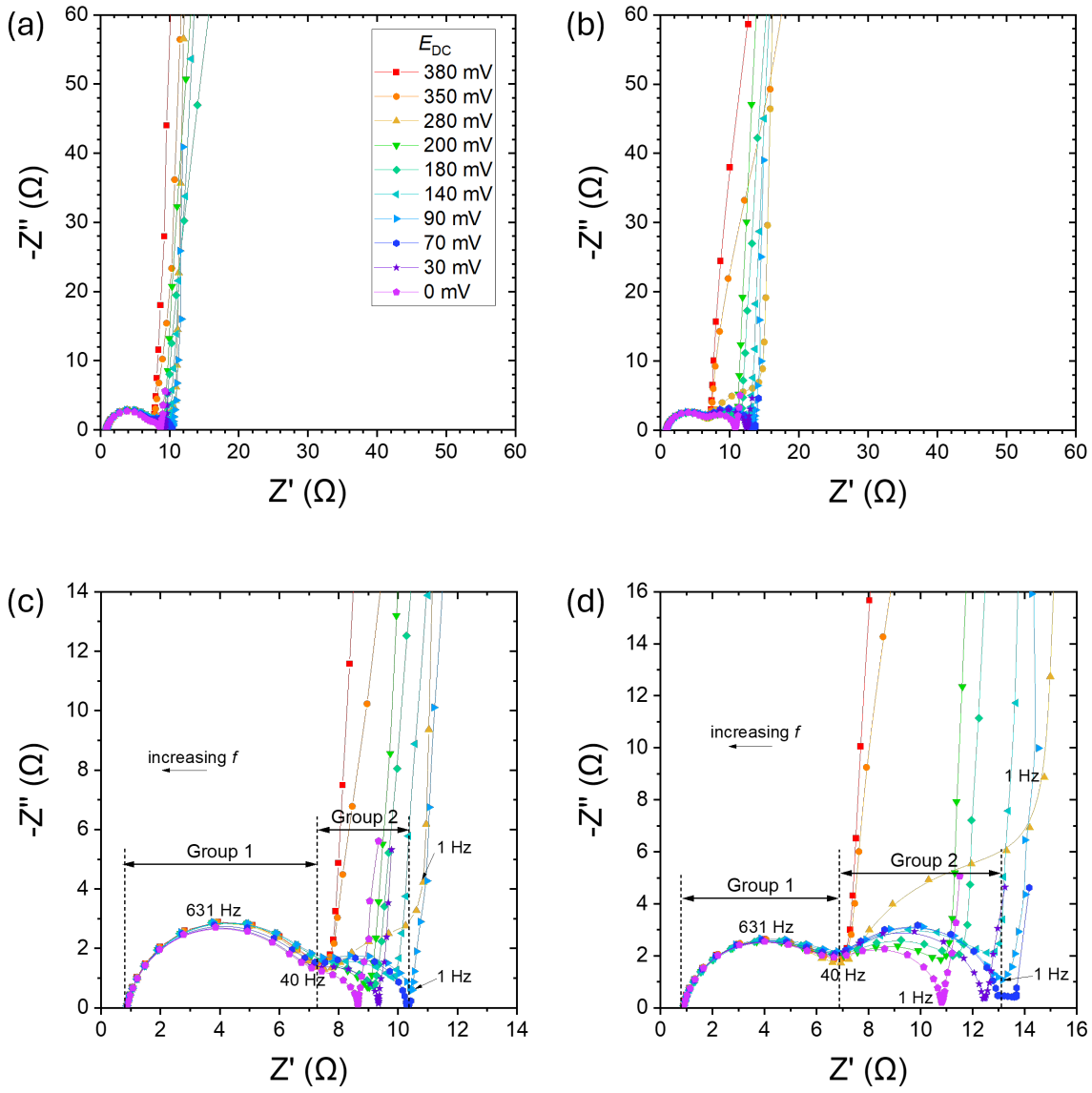

Figure 4.24: Nyquist plots of the impedance spectra for nanoporous Pd with ligament sizes of (a,c) ~ 34 nm and (b,d) ~ 121 nm. Panels (a) and (b) show a broader frequency range, while (c) and (d) present an enlarged view of the higher frequency region. In (c) and (d), the Group 1 and 2 semicircles are indicated. The legend in (a) applies to (a)–(d).

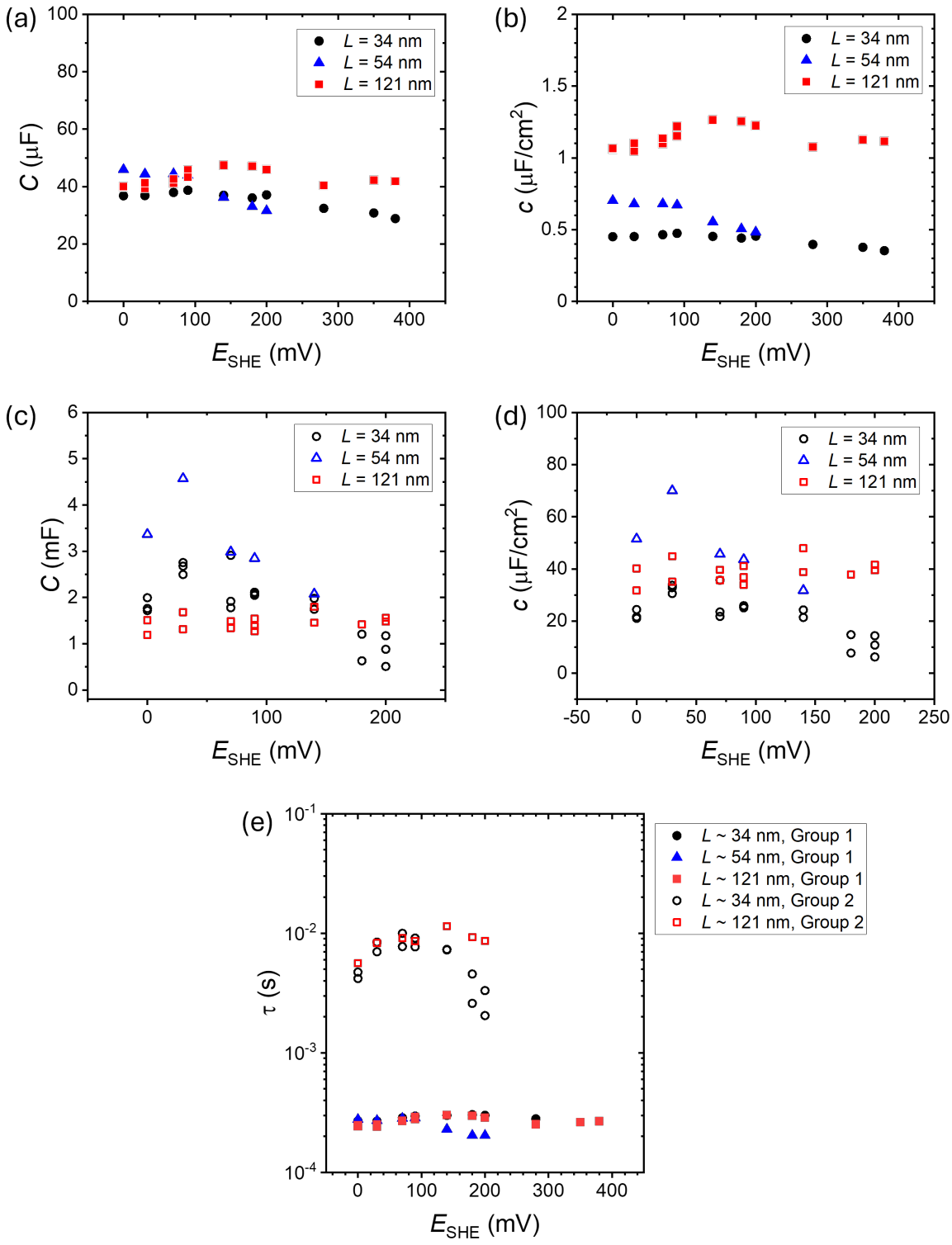

Figure 4.25: Capacitance, C, of nanoporous Pd with different ligament sizes, determined by equivalent circuit fitting of (a) Group 1 semicircles and (c) Group 2 semicircles. Area-specific capacitance, c, for the same samples corresponding to (b) Group 1 semicircles and (d) Group 2 semicircles. (e) Time constants from the equivalent circuit model for each ligament size and semicircle group.

The experimental impedance data in Figures 4.24(c) and (d) feature a constant phase element (CPE) with an exponent greater than 0.996, indicating that the system can be analyzed by fitting it with an equivalent circuit, based on the Boukamp model [200]. The detailed methodology is provided in Sec. 3.3.5. The absolute capacitance, C, and the area-specific capacitance–the absolute capacitance normalized to the electrochemically active surface area of each sample–, c, is derived for each set of semicircles and plotted in Fig. 4.25(a, b) and (c, d) for Groups 1 and 2, respectively. The time constants derived from both groups are plotted together in Fig. 4.25(e). The time constants from each group of semicircles fall within the range of 10^{-4} s and 10^{-2} s, respectively, indicating that two distinct processes are involved and they occur on a milli to microsecond timescale. These timescales remain consistent across the different ligament sizes tested.

Chapter 5

Discussion

5.1 Discussion on the genus-dependent scaling law

5.1.1 Discussion on the new scaling law

The Gibson-Ashby scaling law [105] has demonstrated notable success for stochastic or periodic open-cell microstructures, with widely different geometries and, apparently, similar connectivity. This shows that mechanics and microstructural geometry can be coupled by simple scaling relations. In that case, the key microstructural metric governing the behavior is the solid fraction, φ.

The findings presented in Sections 4.1.1 and 4.1.2 unraveled a separate scaling, namely between the mechanics and the network connectivity as measured by the scaled topological genus, g. It is demonstrated that, at a constant φ, the effective Young's modulus scales with g^2 as embodied in Eq. 4.5. In interpreting this result, one may ask about the physical basis for the numerical value of g_0. The maximum g for leveled-wave-like random network structures is 2.25 (Eq. 2.12 with φ = 1/2) and this falls within the confidence interval of $g_0 = 2.40 \pm 0.50$. Our findings are thus compatible with the notion of the np Au and leveled-wave structures as derived from an "ideal" random network simply by cutting connections. In such an ideal network, $g = g_0 = 2.25$.

As this scaling is derived from leveled-wave-like structures, it is a priori restricted to a specific class of morphologies. That being said, the leveled-wave model has been established to represent a significant range of materials with random bicontinuous microstructures, supporting the relevance of the new scaling law. The apparent commonality in the architecture of different classes of porous and random network materials may be understood as a consequence of similarities in the driving forces and transport mechanisms of the microstructure evolution. The prototypical processes behind leveled-wave-like structures are early-stage spinodal decomposition and later-stage spinodal coarsening, in which surface- or bulk-diffusion act most efficiently at small scale while interfacial free energy minimization favors large scales. The same mechanisms also control the breaking of network struts by Plateau-Rayleigh instabilities [101]. Interfacial energy is generally relevant for porous materials, and diffusive transport is often a prerequisite for microstructure evolution during their formation. This supports the leveled-wave microstructure as a physically motivated model.

In architected periodic lattices, any microstructural descriptor–including the num-

ber and relative angle of struts meeting in a node [9, 13, 14, 201] as well as axial [202–204] and cross-sectional [205] shape factors of the struts–can, in principle, be freely engineered. The accessible parameter space for microstructure design is thus drastically wider than what is explored by nature's spinodal-like microstructure evolution processes, and the conclusions of the present work cannot forcefully be transferred to architected structures from the more general parameter space. Indeed, a study of the elasticity of lattice networks with idealized cylindrical struts that are randomly cut [65] does not support a simple power-law relation between Young's modulus and scaled genus. Yet, that study does support the present findings by exposing the scaled-genus dependence of the elasticity as decoupled from other factors, as expressed in Eq. 4.1.

An error source in extracting the scaled genus from atomic-scale representations of random network structures

The values for the size parameter $\tilde{L}$ are adopted from [140]. That reference determined $\tilde{L}$ of the initial structure from the specific surface area, S_V (surface area per solid volume), exploiting

$$\tilde{L} = \frac{4}{S_V}\frac{\alpha}{\sqrt{3}\varphi}\mathrm{e}^{-[\mathrm{erf}^{-1}(2\varphi-1)]^2} \tag{5.1}$$

for the leveled wave model [66].

S_V in Eq. 5.1 is susceptible to two factors, surface roughness and the volume determination on the basis of surface position. In comparison to the leveled-wave model with a smooth surface, the atomic-scale roughness of the model structure increases the surface area. Furthermore, the volume determination can be impacted by the surface reconstruction algorithm. As the algorithm [140, 206] constructs the surface as an interpolation of atom centers, it shifts the surface inward compared to the leveled-wave surface. As a result of the solid volume being underestimated, the specific surface area becomes erroneously large. This results in a ligament spacing too small and, hence, a lower g value is anticipated with the same E_{eff} value.

The two just-mentioned artifacts yield an initial value of $\tilde{L}$ that is systematically $11 \pm 2\%$ below the true value of the leveled-wave structure [140]. The error in $\tilde{L}$ then propagates to g following Eq. 2.8, so that the initial scaled genus value is underestimated by 1.11^3. As a consequence, the numerical constant g_0 in the scaling law Eq. 4.5 is undervalued by the factor of $1.11^6 \approx 1.9$. This partly explains the shift of the data for initial structures in Fig. 4.6 towards the left boundary of the shaded region.

5.1.2 Assessment of the scaling by Mangipudi et al.

As addressed in Sec. 2.3.4, Mangipudi et al. [137] have determined f_{g} by analyzing Young's moduli of model microstructures, suggesting $f_{\mathrm{g}} \propto g$. Comparing their results to those of the present work requires that the different conventions for specifying the scaled genus are accounted for. Unlike Eq. 2.8, Mangipudi et al. define their scaled genus as

$$\overline{g} = \frac{G}{VS^3} \tag{5.2}$$

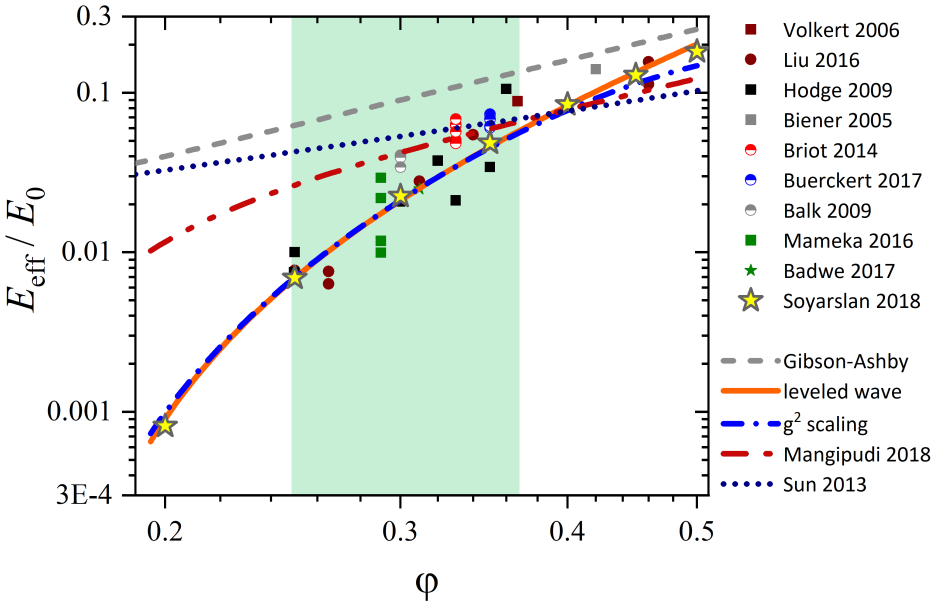

Figure 5.1: Normalized effective Young's modulus E_{eff}/E_0 versus solid fraction φ as Fig. 4.2, but the scaling laws suggested by Mangipudi et al. [137] and Sun et al. [111] are superimposed as the red dash-dot-dotted line and navy short-dotted line, respectively. Note that these latter approaches do not satisfactorily catch the trends in the combined experimental and modeling data for as-prepared nanoporous gold and for leveled-wave-like structures.

with S the surface area per unit foam volume. Analyzing their data set for E_{eff} versus $\overline{g}$, they found

$$E_{\text{eff}} = 5\overline{g}\varphi^2 E_0\,. \tag{5.3}$$

The results in [66]–specifically, the comparisons derived from applying Eq. 3.2 to Eq. 5.2, and Eq. 2.10 to Eq. 2.8 with the notion of $L = \tilde{L}$–imply that

$$\overline{g} = \frac{3\sqrt{3}}{64\alpha^3} e^{3[\text{erf}^{-1}(2\varphi-1)]^2} g\,, \tag{5.4}$$

and this permits us to convert between the two measures for scaled genus and to plot the predictions of the Mangipudi law, assuming the connectivity-solid-fraction relation of the leveled wave model. The result is shown in Fig. 5.1, alongside the various experimental and finite element modeling data discussed in Sec. 4.1.1. It is seen, that the linear scaling suggested by Mangipudi et al. results in a considerably diminished sensitivity of the predicted Young's modulus on the solid fraction. This is an obvious result of the weaker dependence of stiffness on connectivity in their law. Obviously, that law does not appropriately catch the trends in np Au and in leveled-wave-like structures.

Additionally, another scaling law, represented by the navy short-dotted line in Fig. 5.1, introduces a term linear in φ to the quadratic dependence of the Gibson-Ashby law [61, 111]. This modification accounts for stretching, as opposed to bending-dominated deformation, at higher solid fractions. Such law has not been validated against similarly large data sets as Eq.4.4, and the inspection here indicates that it again fails to reproduce the low-φ behavior observed in experiments and numerical simulations for random network materials.

5.2 Relationship between network microstructure and mechanical properties of nanoporous niobium

5.2.1 Mean ligament size and size distribution

It has been suggested that L, the characteristic length scale of a liquid-metal-dealloyed structure, is determined primarily by the coarsening kinetics, and that those obey the power law $L \propto \sqrt{d}$ where d is the dealloyed depth [99]. That would suggest a gradient in ligament size as one moves from the outer surface into the interior of a sample. A more recent investigation, on the other hand, has pointed out that–at sufficiently high temperature–the local dealloying direction may diverge from that of the macroscopic sample surface normal [207]. This implies that an appropriate notion of d can differ locally within the sample. Irrespective of the different suggestions, the electron micrographs did not reveal a noticeable dependency of L on the distance from the sample's exterior surface, indicating each sample has a single, well-defined L value.

Figure 4.8 demonstrates that the L of individual samples can be controlled by adjusting the immersion time and the temperature of molten Mg. As mentioned earlier in Sec. 4.1.3, higher temperature and longer immersion time result in larger L, confirming the coarsening trend reported in [97].

It is also noteworthy that the coefficient of variation, defined as the ratio of the standard deviation, s, to the mean ligament size, L, increases with L. For the examples in Fig. 4.8, the values of s/L are 0.25, 0.35, and 0.37 in order of ascending L. For electrochemically dealloyed np Au, experiment suggests $s/L = 0.303 \pm 0.007$ throughout an interval of ligament size including 20-fold coarsening [172]. This is consistent with self-similar microstructure evolution in np Au. Self similarity is also implied by experimental topology analysis of coarsened np Au [173] and by atomistic simulation [140] of coarsening for $\varphi > 0.3$, as in the present samples. While the absolute s/L values for np Nb–coarsened in-situ during LMD–are roughly similar to np Au, s/L of np Nb systematically increases with $\tilde{L}$, suggesting a gradual loss of structural order and, hence, non-self-similar coarsening. This is consistent with previous findings for LMD-generated porous metals [77]. To summarize, the np Nb samples are distinguished from np Au by thier reduced microstructural order, non-self-similar coarsening, and lesser scaled genus.

Investigations into the mechanism of LMD have emphasized the distinction to aqueous dealloying, and specifically a strong variability of the microstructural morphologies generated by LMD [95, 99]. Whereas aqueous dealloying is controlled sensibly by the kinetics of dissolution and of surface diffusion alone, the transport in the melt and the ensuing phenomena of variable dissolution rate and repartitioning of the master alloy's constituents may generate a richer set of morphologies for LMD. This aligns with morphological variation during coarsening and, consequently, a reduced order.

Besides their different transport pathways, LMD and aqueous dealloying are also distinguished by their microstructure evolution sequences and by the magnitude of the force driving coarsening. In aqueous dealloying, the process involves two stages: primary dealloying, which establishes an initial network in response to the driving force for dissolution, and secondary dealloying, which coarsens the network through the driving forces from capillarity [208, 209]. There are observations that the primary

dealloyed network is quite disordered, yet coarsening transforms it to a spinodal-like, ordered network structure [210]. This primary/secondary dealloying distinction has not been reported for LMD [99, 211], suggesting that the ordering tendency of coarsening plays a less prominent role in LMD. The coarsening behavior of nanoporous metals, which generates and maintains spinodal-like structures–and often self-similarity–is understood as the result of two governing factors, capillarity as the driving force and diffusion as the transport mechanism [101, 140]. Since capillarity scales with the product of surface tension and mean curvature, it is strong in aqueous-dealloyed materials with truly nanoscale ligament size. In contrast, LMD generates sub-micron to micron-scale structures, where the mean curvature can be orders of magnitude weaker. Other factors, for instance crystal lattice defects or microstrain, may then become significant and interfere with the ordering tendency of diffusive coarsening. This may explain why LMD-processed porous metals often deviate from the well-defined, spinodal-like structures observed in aqueous-dealloyed metals.

5.2.2 Size-dependent strength of nanoporous niobium

The yield strength, σ_{Y}, of np Nb is analyzed in relation to the mean ligament size, L. The general trend observed in Fig. 4.13 is consistent with the well-established "smaller is stronger" trend commonly seen in micro- to nanoporous metals [32, 51, 116, 117]. A linear fit of the log-log plot gives the size dependency of $\sigma_{\mathrm{Y}} \propto L^n$ with the size exponent $n = -0.47 \pm 0.27$.

While much research on nanoscale size effect has focused on FCC crystals, two conceivable factors should be considered when comparing these results to np Nb, which consists of BCC material: (1) BCC metals exhibit a higher Peierls stress than FCC metals, and (2) Nb has a relatively low critical temperature. Contrary to FCC metals, which have low Peierls stress and negligible temperature sensitivity, dislocations in BCC metals must overcome a moderate to high level of energy barrier, letting their yield strength more sensitive to temperature. Above the critical temperature, where thermal fluctuation energy can surpass the Peierls barrier, dislocations become thermally activated and have sufficient energy to glide easily [124]. The critical temperature of Nb is 350 K, and it can drop with an athermal stress, for instance, to 290 K under 13 MPa [126]. This suggests that Nb may exhibit behavior similar to FCC metals near room temperature.

The observed power-law exponent of -0.47 for np Nb indeed aligns with previous findings for nanoscale gold, an FCC metal, in small-scale tests [10, 11, 56, 118]. This agreement reinforces the concept that the size reduction may increase the material strength applies not only to individual BCC micropillars, but also to macroscopic networks composed of nanoscale ligaments.

5.2.3 Young's modulus and network connectivity of nanoporous niobium

No clear dependence of the Young's modulus, E_{eff}, on ligament size was observed throughout the experiment. Although a size-dependency could arise from surface excess elasticity, this effect becomes appreciable only at structure sizes well below 10 nm

[8, 212]. Therefore, the results relate to a scale-independent elasticity regime, where the network topology may play a decisive role [8, 62, 137].

The effective Young's modulus of np Nb is plotted in Fig. 4.12 alongside LMD-made porous Ti and $Fe_{0.80}Cr_{0.20}$ [72, 74] and np Au (aqueous dealloying) [52, 54, 82, 107, 189–191]. The Gibson-Ashby scaling law [59] and the modified Roberts-Garboczi scaling law parameterized for np Au and for leveled-wave structures [66] are superimposed for comparison. The Roberts-Garboczi scaling law fitted to the leveled-wave structure has successfully reproduced the relation between microstructural features and elastic properties of np Au [66] as shown in the Figure. Strikingly, np Nb exhibits a 10 to 60 times lower modulus compared to the scaling laws. E_{eff} is also considerably lower than the experimental results for np Au of similar relative density [10, 54, 62]. This anomalous compliance indicates that the Gibson-Ashby scaling law overpredicts np Nb's stiffness from its φ, and the fitting parameters of the Roberts-Garboczi scaling law for np Au might not be applicable to np Nb.

Deviations between the Gibson-Ashby scaling for constant-connectivity structures and real nanoporous materials have been related to a solid-fraction-dependent connectivity [53, 60, 62, 65, 82, 111, 184]. This motivates an examination of the topological genus, as a quantifiable measure of connectivity. The average g of np Nb is found to be 1.2 and, thereby, ~1.5 times lower than that [66] of the leveled-wave model structure at the same solid fraction. Qualitatively, therefore, the anomalous compliance of np Nb can be traced back to its deficiency in connectivity. For network structures derived from the leveled-wave model (Sec. 4.1.1) and with disconnections due to coarsening (Sec. 4.1.2), the E_{eff} at any given solid fraction scales as g^2. That scaling is obviously not applicable to the LMD Nb samples since–compared to np Au–np Nb's reduction in E_{eff} considerably exceeds the squared relative change in scaled genus. This emphasizes further that the microstructural morphology and topology of the LMD samples differ substantially from that of np Au produced by aqueous dealloying.

In the context of microstructure metrics for nanoporous metals that might impact their mechanics, beyond the classic parameters of solid fraction and ligament size, the topological genus stands out. Its connection to stiffness and strength has been firmly established [36, 62, 65, 66, 82] and, for the special case of spinodal-like structures, has been formulated into a scaling law [184]. Yet, other metrics have also been suggested or identified as relevant. In addition to the above-mentioned width of the ligament size distribution, this includes specifically details of the ligament morphology [204, 213] and the size distribution of load-bearing rings within the ligament network [214]. Each of these parameters may influence the mechanical performance of LMD-produced np Nb. However, scaling laws that might be combined with the current data for a more comprehensive discussion of their impact have yet to be established.

5.3 Hydrogen sorption kinetics in nanoporous palladium

5.3.1 Nanoporous palladium for hydrogen sorption

Nanoporous Pd proved to be an experimentally more suitable material for characterizing hydrogen kinetics compared to np Nb. As stated in Sec. 4.1.3, one key issue with np Nb is the presence of NbO, a stable oxide phase commonly formed under atmospheric conditions. The existence of this oxide layer on Nb samples was foreseeable, given the material's high surface area, which makes it particularly susceptible to oxidation. Despite the attempts to remove this oxide layer through heat treatment up to 800°C under vacuum and exposure to hydrogen gas as a reducing agent, it persisted and was identified as a possible barrier for hydrogen absorption into the Nb lattice. More extreme conditions, such as ultra-high vacuum at temperatures above 1600°C, as reported by [215], were not applicable without compromising the stability of the porous structure. Despite these efforts, np Nb was ultimately unsuitable for hydrogen sorption studies, hence the following discussion will focus exclusively on np Pd.

5.3.2 Size effect on hydrogen solubility

For the hydrogen solubility of np Pd presented in Figures 4.19(a) and (c), the solubility differences between pairs of independent samples were analyzed using the Mann–Whitney U test [198]. This method was chosen because the solubility datasets are not expected to follow a normal distribution, and the measurement from each sample are independent. The p-values ranging from 0.49 to 0.87, as presented in Sec. 4.2.2, are greater than the conventional criterion of 0.05, indicating that there is no statistically significant difference between the samples. In contrast to an earlier observation on nanocrystalline Pd [216], where interface stress caused by hydrogen enrichment or depletion at interfaces (grain boundaries) can alter hydrogen solubility in the bulk [216], the bulk absorption behavior of np Pd appears independent of ligament size. This inconsistency can be attributed to differences in microstructural scale. While the mean grain sizes of [216] range between 8 – 12 nm, the ligament size of np Pd is an order of magnitude larger. This larger structural feature likely alleviate the influence of interface on hydrogen bulk solubility.

The size-independence of hydrogen solubility can be further discussed in relation to the sorption strain magnitude shown in Fig. 4.21. While solubility (Fig. 4.19) is derived from the charge data measured by potentiostat, the saturation strain (Fig. 4.21) is independently obtained via dilatometer. Especially for the α' phase, where the UPD effect is negligible compared to the bulk-absorbed hydrogen, the size-independence of solubility does not explain the reduced strain observed in the larger ligament sample. The pronounced size-dependence of saturation strain remains to be investigated. Potential approaches are outlined in Sec. 6.2. Current observations so far suggest that the reduction of ligament size may amplify chemo-mechanical coupling.

5.3.3 Reaction mechanisms and rate-limiting process

The impedance spectrum of np Pd displayed in Sec. 4.2.4 can be roughly divided into three distinct regions, each corresponding to a specific physical interface or process. This section analyzes the impedance spectrum in connection with the physical origins of each region of the plot. For the analysis, the hydrogen evolution reaction is excluded from consideration, as the potential levels of interest, E_{DC}, are above the threshold for $H_2(g)$ generation [160]. In other words, all measurements were conducted at potentials positive to the hydrogen evolution reaction.

Prior to analysis, one intrinsic effect to be addressed is the electric double layer (EDL). The characteristic thickness of EDL, λ, is given as [217]

$$\lambda = \left(\frac{\varepsilon_0 \varepsilon_{\mathrm{r}} RT}{F^2 z^2 c_0} \right)^{1/2} . \tag{5.5}$$

where ε_0 is the permittivity of free space, ε_{r} is the relative permittivity of the electrolyte, R is the gas constant, T is the absolute temperature, F is the Faraday constant, z is the valence of ionic species, and c_0 is the molar concentration. For hydrogen ions in 1 M H_2SO_4 at room temperature, assuming a relative permittivity similar to that of water, λ is approximately 13 nm. Comparing this λ value to the pore sizes of np Pd–which are also on the same scale as the ligament size [218]–the overlapping of EDL is unlikely [219]. Therefore, any effects from EDL overlapping are not considered here.

Given that the CPE exponent of the semicircles in the complex plane plots of Figures 4.24(c) and (d) is close to 1, the patterns represent the coupling of capacitive and resistive behavior associated with surface characteristics. The high-frequency semicircles, labeled Group 1 and located in the left section of each plot, overlap across all E_{DC} levels, indicating that the impedance of this interface layer is independent of the Pd-H state. Additionally, Figures 4.25(a) and (b) show that the capacitance is independent of ligament size but diverges significantly when normalized to the electrochemically active surface area. This suggests the capacitance may originate from a source external to the sample, possibly a setup artifact, the interface between the sample and the holder. The comparable absolute capacitance values across samples in Fig. 4.25(a) further support this, as the setup and the wiring are nearly identical for all measurements. The time scale of these semicircles is calculated following Eq. 3.5, with the results presented in Fig. 4.25(e). The time scales are consistently on the order of 10^{-4} s, regardless of ligament size or E_{DC}. This is significantly shorter than the actuation process time scale ($\approx 10^2$ s), suggesting that charge transfer occurring from the setup artifact is negligible for actuation speed.

The second set of capacitive loops, labeled Group 2 in Fig. 4.24(c) and (d), appears only below the transition point to UPD, i.e., $E_{\mathrm{DC}} < E_{\mathrm{UPD}}$, where $E_{\mathrm{UPD}} \approx 240$ mV [220]. This indicates that this Group 2 semicircles are due to the presence of hydrogen atoms on Pd surface. Hydrogen underpotential deposition is characteristic of Pt-group metals [160], including Pd, where H atoms form covalent bonds with the metal substrate and occupy surface sites [156]. On Pd (111) and (100) surfaces, the energetically favored sites are threefold and fourfold hollow sites, respectively, as illustrated in Fig. 2.11 for each facet. The diminished divergence in capacitance between ligament sizes when normalized to the electrochemically active surface area (compare Figures 4.25(c) and (d)) further indicates that the Group 2 semicircles originate from surface-adsorbed

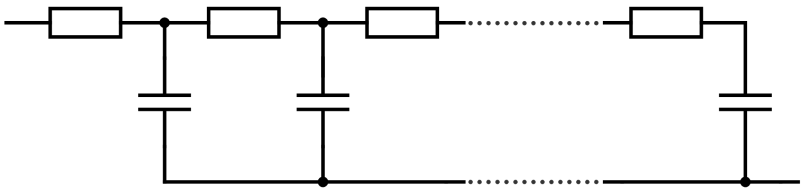

Figure 5.2: The equivalent circuit of a (semi-)infinitely large network of pores. The resistances and capacitances of individual resistors and capacitors are not necessarily identical.

charge on np Pd. Each pore consisting of the Pd surface brings a certain amount of capacitance and resistance to the system, and the collective behavior of a semi-infinite number of pores in the macroscopic sample can be modeled as a transmission system [221–224]. A simplified schematic of this circuit model is shown in Fig. 5.2. The exact calculation from this microscopic picture is challenging, if not impossible, as it requires the exact number of pores (components) in the macroscale sample and the random shapes of each pore. Instead, area-specific capacitance, c, is calculated by dividing the absolute capacitance by the electrochemically active surface area, as shown in Fig. 4.25(d). The c values of np Pd align with the typical EDL capacitance values for Pd, $20 - 65\,\mu\mathrm{F/cm^2}$ [225–227]. Although there is a strict difference that UPD H is adsorbed onto the electrode surface within the Stern layer of the EDL, while EDL capacitance arises from both the Stern layer and the diffuse layer, this comparability suggests that adsorbed H^+ ions play a key role in the capacitive behavior at the interface.

The time scales for charge transfer in the near-surface layer (corresponds to Group 2), plotted in Fig. 4.25(e), range from $10^{-3}\,\mathrm{s}$ to $10^{-2}\,\mathrm{s}$ and exhibit no significant dependence on ligament size, except for a minor deviation at $E > 140\,\mathrm{mV}$. These values are broadly comparable to the relaxation time of adsorption/desorption process of hydrogen on Au in acidic solution, $0.12\,\mathrm{ms}, 0.20\,\mathrm{ms}$, reported by [228]. This relatively fast process can be associated with the movement of ions in the pore space, facilitated by the Grotthuss mechanism [229]. The Grotthuss mechanism involves the formation and breaking of covalent bonds between neighboring water molecules, and protons can move through such a chain reaction. It enables fast and efficient hydrogen transport by a proton hopping process, transferring protons through a network of hydrogen-bonded water molecules. The short time scale of such process again confirms that charge transfer across the adsorbed layer at the interface is negligible when considering the overall actuation duration of $\approx 10^2\,\mathrm{s}$, and does not significantly impact the total actuation time.

An additional step involved in the hydrogen charging process is the diffusion of absorbed H into the bulk of metallic Pd, driven by the concentration gradient. The diffusion time scale of H in the α phase of Pd-H system is estimated based on [230, 231]. Using half the ligament diameter, in the range of $10 - 100\,\mathrm{nm}$, as the diffusion distance, and the diffusion constant of H in Pd lattice at 300 K, $D = 3.8{\times}10^{-11}\,\mathrm{m^2/s}$ [147, 231], the equilibration time scale for np Pd in this work is estimated to be on the order of $10^{-6}\,\mathrm{s}$ to $10^{-4}\,\mathrm{s}$. This diffusional process is negligibly fast compared to the overall charging

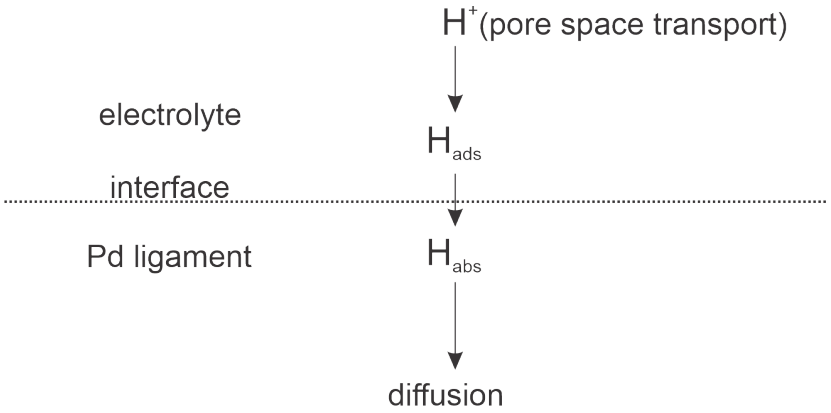

Figure 5.3: Hydrogen charging process in nanoporous Pd. The diagram illustrates hydrogen adsorption and absorption at the electrolyte–Pd ligament interface, along with diffusion within the Pd lattice.

process, explaining the absence of mass transfer impedance (Warburg impedance) in the Nyquist plots in Fig. 4.24.

The steps discussed above are schematically illustrated in Fig. 5.3 and the order of their length and approximate time scales are listed in Table 5.1. The length scale of the charge transfer is approximated from the sample dimension, while the activated jump lengths are approximated based on the lattice spacing of Pd.

Table 5.1: Processes and scales, approximately

process	length scale	time scale
activated jump - adsorption	0.2 nm	10 ms
activated jump - injection	0.2 nm	10 -100 s
diffusion within Pd ligaments	10 - 100 nm	$1 - 100\,\mu$s

Since the actuation of np Pd-H involves multiple steps in series, the slowest one dictates the overall reaction rate. A comparison of the actuation response time, which ranges from 1 to 10 minutes, with other time scales outlined in Table 5.1, reveals that these processes are sufficiently fast and not rate-limiting. This suggests that the primary rate-limiting factor is charge injection at the Pd surface, and that the actuation of np Pd operates under interface kinetics constraints. The characteristic of surface injection (Faradaic process) is not captured in the EIS measurement, therefore, alternative methods, such as potential jump tests, are necessary to accurately observe the full response kinetics of np Pd-H.

The finding that charge injection is the primary rate-limiting factor is consistent with the faster actuation observed in samples with smaller ligaments. Smaller ligaments provide a larger specific surface area, facilitating surface interaction–specifically hydrogen absorption–and thus accelerating the hydrogen charging of Pd bulk. The enhanced charging speed in np Pd with reduced ligament size provides a clear pathway for optimizing H-based actuators.

5.3.4 Reaction modeling of hydrogen sorption kinetics

In the previous section, it was concluded that the charging time scale of np Pd is primarily governed by the charge injection, i.e., the hydrogen transfer across a barrier at the surface. Therefore, the hydrogen sorption kinetics are modeled with a focus on the surface injection process, assuming an energy barrier for hydrogen insertion and removal. The discharging process is perfectly analogous to the charging process, and the focus here is on the charging process.

It is also demonstrated that hydrogen diffusion within the Pd lattice is sufficiently fast to assume (quasi-)instantaneous equilibrium within the sample. In other words, the hydrogen composition at the surface is effectively the same as that within the ligament interior at all times. In the following discussion, the term "hydrogen concentration" refers to the bulk composition, without distinguishing it from the surface composition and neglecting any composition gradient.

Deriving the kinetic rate equation using the Butler–Volmer equation

Consider a finite size of Pd solid crystal initially equilibrated to a constant hydrogen composition. The Pd-H solid solution can exchange mass and energy with a much larger fluid reservoir, effectively considered infinite in size. The temperature is constant over time throughout the system, and with no spatial temperature gradient. In this state, the charge flux, j, coming from the hydrogen injection is zero. When an overpotential is applied, the system is perturbed from equilibrium, and the flux j is–according to standard assumption in the literature–governed by a Butler-Volmer-like current-overpotential equation [163], with the hydrogen concentration x concurrently changing over time. The injection and extraction rates scale with the concentrations of vacant and occupied sites in the crystal, leading to the current-potential relation expressed as

$$j = j_{\mathrm{ex}} \left[\frac{1-x}{1-x_{\mathrm{eq}}} \exp\left(-\alpha \frac{F(U-U_{\mathrm{eq}})}{RT} \right) - \frac{x}{x_{\mathrm{eq}}} \exp\left((1-\alpha) \frac{F(U-U_{\mathrm{eq}})}{RT} \right) \right], \tag{5.6}$$

where α is the transfer coefficient, j_{ex} is the exchange current density ($j_{\mathrm{ex}} > 0$), x_{eq} is the equilibrium concentration corresponding to the final state, F is the Faraday constant, R is the gas constant, and T is the temperature. Here, U corresponds to the applied potential and U_{eq} is the potential at the equilibrium state, thereby without loss of generality, it is free to say that $U = U_{\mathrm{eq}}$. By definition, j reaches zero when $x = x_{\mathrm{eq}}$. With $U = U_{\mathrm{eq}}$, it leads to

$$j = j_{\mathrm{ex}} \left(\frac{1-x}{1-x_{\mathrm{eq}}} - \frac{x}{x_{\mathrm{eq}}} \right). \tag{5.7}$$

The implication of Eq. 5.7 is that the driving force for charge transfer is determined by the hydrogen concentration, particularly when the current value, x, deviates from the final concentration at equilibrium, x_{eq}. This governing equation is applicable to ideal solutions.

For a Pd sample with arbitrary finite geometry (see Fig. 5.4) characterized by volume V and surface area A, and with an assumption that the current flux is normal

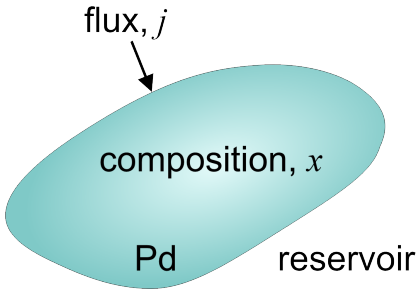

Figure 5.4: A schematic of a random shape of Pd structure, with a hydrogen concentration of x and subject to the hydrogen injection charge flux j.

to the surface and uniform across the sample surface, by definition,

$$\frac{\mathrm{d}}{\mathrm{d}t}\int_V x\,dV = \Omega j A \tag{5.8}$$

where Ω is the atomic volume of Pd. With a non-zero flux, x evolves over time, denoted as $x(t)$. Consequently, j also becomes a time-dependent function, as it depends on $x(t)$ through Eq. 5.7. The concentration is uniform throughout the volume, as explained at the beginning of this section. Under this condition and the given variable dependencies, Eq. 5.8 simplifies to

$$\frac{\mathrm{d}x(t)}{\mathrm{d}t} = \alpha_S \Omega j(t)\,. \tag{5.9}$$

The specific surface area, $\alpha_S = A/V$, is introduced as a parameter bound to the sample geometry. Changes in α_S due to hydrogen-induced expansion are neglected for simplicity. By substituting $j(t)$ from Eq. 5.7 into Eq. 5.9,

$$\frac{\mathrm{d}x(t)}{\mathrm{d}t} = \Omega\alpha_S j_{ex}\left(\frac{1-x(t)}{1-x_{eq}} - \frac{x(t)}{x_{eq}}\right). \tag{5.10}$$

The boundary conditions are $x = x_i$ at $t = 0$ and $x = x_{eq}$ at $t = \infty$. Solving 5.10 yields a closed-form expression for $x(t)$, which is given by

$$x = x_{eq} + (x_i - x_{eq})\exp\left(-\frac{\alpha_S \Omega j_{ex}}{x_{eq}(1-x_{eq})}t\right). \tag{5.11}$$

As mentioned in Sec. 4.2.3, the half time of charging is defined as the time when $x = (x_{eq} - x_i)/2$. This half time can be determined either numerically from the x versus t plot or from the exponent in Eq. 5.11, as the time constant of the exponential response is linearly proportional to the half time. The half time for an initially dilute sample with a non-zero initial concentration of $x_i = 0.001$ is shown by the blue solid line in Fig. 5.5, plotted against equilibrium concentration, x_{eq}. By the definition of charging, x_{eq} is greater than x_i and the abscissa is normalized to the site density, $x_{site} = 1$, the value that x cannot exceed. The ordinate is normalized to the characteristic parameter of the system, $\tau_0 = 1/\alpha_S \Omega j_{ex}$. The plot shows that charging time increases with the final state concentration up to $x_{eq} = 0.5$ and decreases beyond this point.

In the same Fig. 5.5 the experimental data adapted from [167] is superposed for comparison. Here, data for $x_{eq} \lessapprox 0.03$ are not considered for the present discussion as

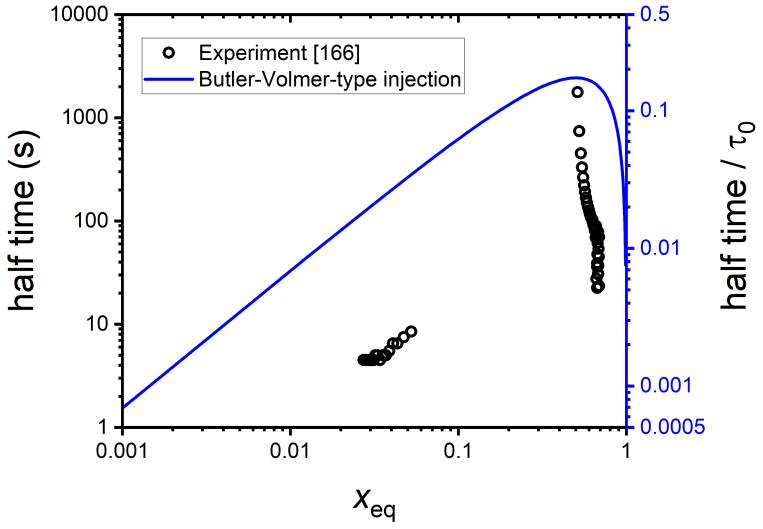

Figure 5.5: Normalized half time of Butler-Volmer-type hydrogen injection process (blue line), as a function of equilibrium hydrogen concentration, x_{eq}, scaled by the site density, x_{site} = 1. Experimentally measured half time of hydrogen actuation in nanoporous Pd at different equilibrium hydrogen concentration is superposed for comparison (black circle). Experimental data recreated from [167] with permission.

they remain in the UPD regime and do not involve bulk absorption. When comparing the model's prediction to experimental data, the model reproduces the general trend observed in the experiments: the half time increases with x_{eq} in the α phase ($x_{eq} \lessapprox 0.05$), while the opposite is true for the α' phase ($x_{eq} \gtrapprox 0.5$) with a larger negative slope. Additionally, the relationship τ_0 being inversely proportional to α_S, and α_S inversely proportional to ligament size [232, 233], qualitatively explains the longer half times observed for larger ligaments (See Fig. 4.22 and Sec. 4.2.3). However, upon closer inspection, the model either overpredicts the half time in the α phase, or underpredicts it in the α' phase. Notably, near x_{eq} = 0.5, the experimental trend deviates significantly from the predicted curve, suggesting that the model fails to accurately capture the sharp increase in half time near the phase transformation point. Additionally, the residuals–the differences between the experimental and model values–are non-randomly distributed. This pattern indicates that there are systematic errors in the model, and that this ideal solution model does not fully represent the behavior of the real system.

Modification of the Butler-Volmer equation

To account for the discrepancy, the activation enthalpy associated with elastic strain can be implemented in the previously mentioned Butler-Volmer-type reaction [234]. The findings of [234] suggest that changes in the electrode's strain, which directly affect the lattice spacing, can modify the energy barrier for the combination of protons and hydrogen adsorption. The surface stress response can appear as either expansion or contraction of the lattice, and can be quantified by introducing the electrocapillary coupling parameter, ς, defined as $\varsigma = \mathrm{d}f/\mathrm{d}q|_e$, where f, q and e are the surface stress, the superficial charge density and the tangential strain at the surface, respectively [199]. A positive value of ς has been reported in [199, 234, 235] for hydrogen electrosorption

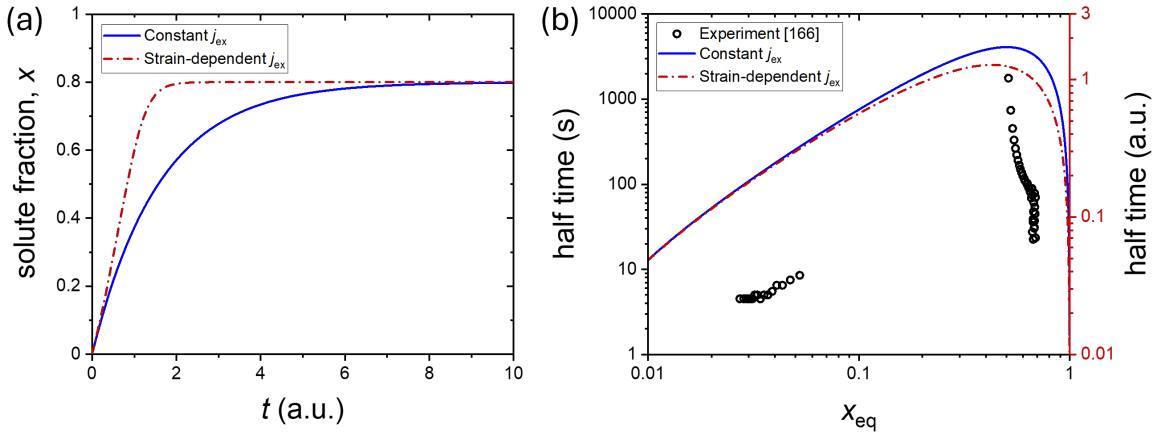

Figure 5.6: (a) Hydrogen fraction, x, as a function of time, t, with an initial concentration of 0.001 and equilibrium concentraion of 0.8. (b) Half time of the hydrogen injection process as a function of equilibrium hydrogen concentration, x_{eq}, with time in arbitrary units. The black circle represents experimental data, recreated from [167]. For both (a) and (b), the dash-dotted line corresponds to the Butler-Volmer reaction modified for strain-dependent activation enthalpy, and solid line represents the classical Butler-Volmer-type reaction with a constant exchange current density.

on Pt and Pd. This observation aligns with the fact that hydrogen sorption induces macroscopic expansion and tensile surface stress, and that the reaction is accelerated.

This strain-dependence of the activation enthalpy is incorporated into the rate equation and the impact is examined. Since increased charge density amplifies strain effects, this introduces an dependence on the hydrogen bulk concentration, x. For Pd, the strain, $e = \Delta l/l_0$, is linearly proportional to the hydrogen concentration [40] and can be linked to the mean hydrogen bulk concentration, x, through the strain-concentration coefficient, $\eta = l_0^{-1}\partial l/\partial x$. This alteration in energy barrier can be reflected in the exchange current term, j_{ex}, by introducing a x-dependency of j_{ex}, which was previously treated as a constant in the formal approach. Referring to [234], j_{ex} can be expressed as follows.

$$j_{\mathrm{ex}} = j_{\mathrm{ex},0} \exp\left(\frac{F\eta\varsigma}{RT}x\right) \tag{5.12}$$

with a constant $j_{\mathrm{ex},0}$.

Equation 5.10 remains valid with this modification. Thus, by equating Eq. 5.10 and Eq. 5.12, the resulting differential equation becomes

$$\frac{\mathrm{d}x(t)}{\mathrm{d}t} = \Omega\alpha_{\mathrm{S}} j_{\mathrm{ex},0} \exp\left(\frac{F\eta\varsigma}{RT}x\right)\left(\frac{1-x(t)}{1-x_{\mathrm{eq}}} - \frac{x(t)}{x_{\mathrm{eq}}}\right), \tag{5.13}$$

and is solved numerically. For the calculations, the parameters are set as follows: $\eta = 0.06$ [167], $\varsigma = 1\,\mathrm{V}$ [234], and $T = 300\,\mathrm{K}$. Arbitrary values of $\Omega = 1, \alpha_{\mathrm{S}} = 1$, and $j_{\mathrm{ex},0} = 0.1$ are assigned for simplicity, without affecting the generality of the results. Figure 5.6 displays the modified version alongside the classical Butler–Volmer-type response, using the boundary conditions of $x = 0.001$ at $t = 0$ and $x = 0.8$ at $t = \infty$. In Fig. 5.6(a), the hydrogen concentration reaches x_{eq} more quickly than the classical

Butler-Volmer-type process with a constant j_{ex}, as expected. This is reflected in the reduced half time in Fig. 5.6(b). The blue solid line in Fig. 5.6(b) corresponds to that of Fig. 5.5. The modification shifts the slope of the plot, however, it does not improve the agreement with the experimental data. Specifically, the sharp increase near $x_{eq} = 0.5$ is still not satisfactorily captured, and the convexity observed in the experimental curve for $x_{eq} > 0.5$ contrasts with the model's concave prediction.

Kinetic rate equations from a thermodynamic perspective

The Butler-Volmer equation, which forms the basis of the previous approaches, combines the charge transfer rate with the overpotential. However, this model does not account for the miscibility gap, the central behavior of the Pd-H solid solution. In this section, the equilibrium states are evaluated strictly from a thermodynamic perspective and the composition-dependent energy of H in the Pd crystal lattice is incorporated. The kinetic rate is then determined by revisiting the parameters in the ready-made Butler-Volmer equation.

Following the model scenario in [236], an interstitial regular solution, where the solute is randomly distributed on available interstitial sites, is considered. The energy of the system arises from the bonds H–H and H–matrix (host material, Pd), with fixed bond energies. The molar enthalpy, H, of the solution with solute fraction x is

$$H = \Omega_M x + \Omega_S x(1-x)\,, \tag{5.14}$$

where Ω_M is the energy associated with interactions between solute and the matrix and Ω_S is the energy associated with interactions between solute molecules. The enthalpy due to solute-matrix interactions scales linearly with x since it involves the fraction of solute in the system. The energy due to solute-solute interactions depends on both x and $(1-x)$, accounting for pairwise interactions.

The entropy, S, is derived from the number of microstates, Ω. For a solid solution containing two types of atoms, of which the numbers are xN and $(1-x)N$, the number of possible configurations of this system is given by $N!/(xN)!(1-x)N!$. The entropy is then expressed as $S = k\ln\Omega$, where k is the Boltzmann constant. Simplifying this expression using Stirling's approximation and the relation $R = N_A k$, where N_A is Avogadro's number and R is the gas constant, leads to

$$S = -R\left(x\ln x + (1-x)\ln(1-x)\right)\,. \tag{5.15}$$

Then the molar Gibbs free energy, G, at temperature T is given by

$$G = H - TS \tag{5.16}$$

Subsequently, the chemical potential, μ, of the solid is given by the derivative of G with respect to the solute fraction x: $\mu = \partial G/\partial x$. This determines the driving force for mixing or phase separation. By substituting Eq. 5.14 and Eq. 5.15 into Eq. 5.16, and taking the partial derivative with respect to x,

$$\mu = \Omega_M + \Omega_S(1-2x) + TR\ln\left(\frac{x}{1-x}\right)\,. \tag{5.17}$$

For the reservoir, it contains H in the form of protons and electrons, and the chemical potential accounts for both species. Without loss of generality, one can set the chemical potential of protons to zero. The reservoir is assumed to be at a constant composition, which gives the chemical potential of the reservoir, μ_{R}, as

$$\mu_{\mathrm{R}} = -FU_{\mathrm{app}}\,, \tag{5.18}$$

for an applied electric potential, U_{app}, and the Faraday constant, F.

The thermodynamic condition for equilibrium is when the chemical potentials are equal between the two communicating phases, the reservoir and the solid. From this condition, the solute fraction in the solid at equilibrium, x_{eq}, is evaluated. In order to solve the system numerically, the variables are scaled to dimensionless form. The reduced chemical potential, μ_{red}, and the dimensionless temperature, τ, are defined as

$$\mu_{\mathrm{red}} = \frac{\mu}{\Omega_{\mathrm{S}}} \tag{5.19}$$

and

$$\tau = \frac{T}{T_c} \tag{5.20}$$

where $T_c = \Omega_{\mathrm{S}}/2R$ is the critical temperature at which the miscibility gap in the solution vanishes [236]. Assuming that the matrix behaves as an ideal, neutral medium that neither attracts nor repels the solute H, $\Omega_{\mathrm{M}} = 0$. Then, Eq. 5.17 simplifies to

$$\mu_{\mathrm{red}} = 1 - 2x - \tau\,\mathrm{arctanh}(1-2x)\,. \tag{5.21}$$

A numerical procedure is implemented to solve the equation for x, and evaluate the equilibrium composition at a given temperature and chemical potential. At two-phase coexistence, the chemical potential is zero. The spinodal condition, derived from the thermodynamic stability criteria, $\partial\mu/\partial x = 0$, is [236]

$$\tau = \frac{1}{T_c}\frac{2\Omega_{\mathrm{S}}}{R}x(1-x)\,. \tag{5.22}$$

The solute compositions at the spinodal point, both the dilute and concentrated compositions at a given reduced temperature, can be numerically calculated. For the example case of $\tau = 0.8$, Fig. 5.7 shows μ_{red} as given by Eq. 5.21. The plot highlights the spinodal composition in the α phase (red circle) and displays the charging path (dotted arrow) with the phase transformation, in the direction of increasing x.

The Faradaic current of the reaction is now modeled in the scheme of the Butler-Volmer equation, Eq. 2.23, but the overpoential at any instance during the charging process, is defined in the spirit of [237, 238]. In both works, the open circuit potential, U_{OCP} is the virtual equilibrium potential at any instant, and then the overpotential, η, is defined as the difference between the applied potential, U_{app}, and the instantaneous U_{OCP}:

$$\eta = U_{\mathrm{app}} - U_{\mathrm{OCP}}\,. \tag{5.23}$$

That U_{OCP} is again a function of the solute concentration, x, and can be formulated into a function of x by equating Eq. 5.17 and the chemical potential of H^+, μ_{H^+},

$$\mu_{H^+} = -FU_{\mathrm{OCP}}. \tag{5.24}$$

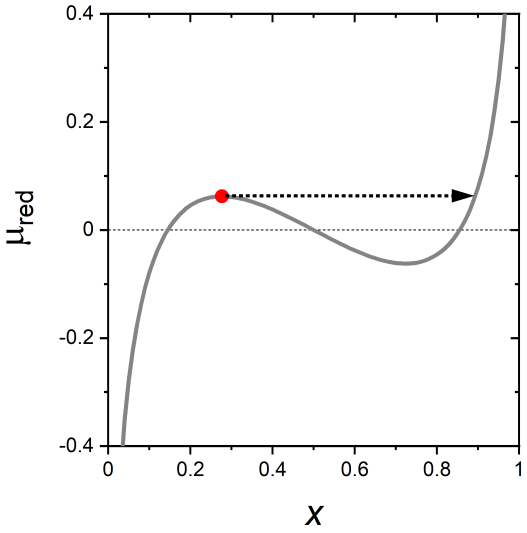

Figure 5.7: Reduced chemical potential, μ_{red}, as a function of solute fraction, x, for $\tau = 0.8$. The red circle marks the spinodal composition in the dilute (α) phase. The dotted arrow represents the charging path, bypassing the unstable states.

U_{app} serves as the driving force toward equilibrium, ultimately determining the final concentration at equilibrium, $x = x_{\mathrm{eq}}$. Consequently, it can also be written in terms of x_{eq} as the decisive parameter corresponding to U_{app}. The value of x_{eq} can be obtained by solving for U_{app} as a function of x_{eq}, derived from equating Eq. 5.17 and Eq. 5.18.

$$U_{\mathrm{app}} = \frac{-\Omega_S + 2x_{\mathrm{eq}}\Omega_S - TR\ln x_{\mathrm{eq}} + TR\ln(1 - x_{\mathrm{eq}})}{F} \tag{5.25}$$

Since there are two-phase coexistence regions in the parameter space, where a given U_{app} may correspond to multiple values of x_{eq}, numerically, the first element of the list of solutions is selected. This ensures that the system bypasses any unstable states, which correspond to the unstable interval shown in Fig. 5.7. This naturally raises the question whether the use of chemical potential is appropriate in this context. The system is assumed to equilibrate instantaneously, or in other words, the injection is slow enough that the bond-count-based equations, Eq. 5.14 and Eq. 5.15 as well as the chemical potential extracted from Eq. 5.16, remain valid. However, the equilibrium and homogeneity assumption appear to contradict spinodal decomposition. The extended use of free energy within the spinodal decomposition range is justified by earlier works [239–241], which demonstrate that the free energies of an interface can be considered as specific stationary points of a broader expression that describes the free energy of a system.

By substituting the expression for η in terms of x and x_{eq}, and combining Eq. 5.24 and Eq. 5.25 into Eq. 2.23, with $z = 1$ for the hydrogen injection reaction and $\alpha_{\mathrm{a}} = \alpha_{\mathrm{c}} = 1/2$ for simplification, the rate equation becomes

$$j = j_{\mathrm{ex}} \frac{e^{-\frac{2(x+x_{\mathrm{eq}})}{\tau}} \left(e^{\frac{4x}{\tau}}(-1+x)x_{\mathrm{eq}} - e^{\frac{4x_{\mathrm{eq}}}{\tau}} x(-1+x_{\mathrm{eq}}) \right)}{\sqrt{(1-x)x}\sqrt{(1-x_{\mathrm{eq}})x_{\mathrm{eq}}}} . \tag{5.26}$$

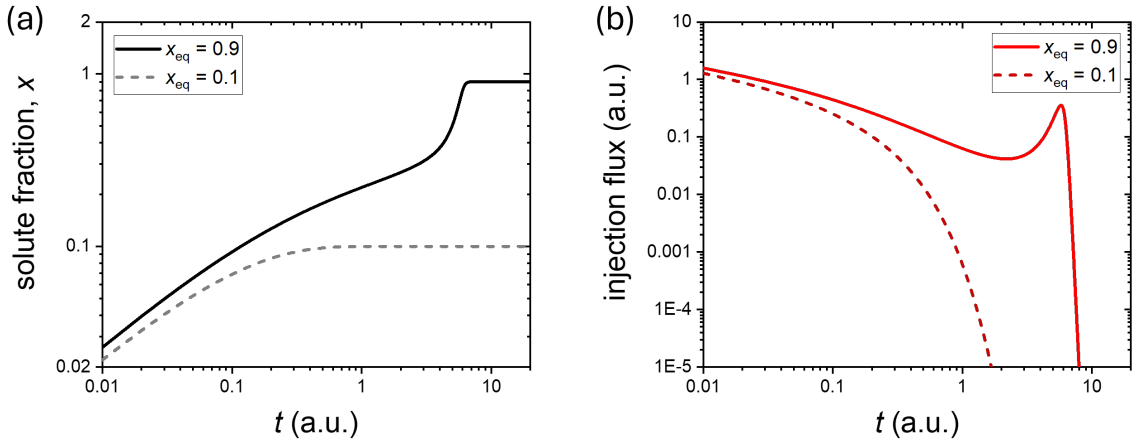

Figure 5.8: The hydrogen injection responses over time, modeled from a thermodynamic perspective. (a) Solute fraction, x, as a function of time, t, with an initial value of 0.001 and $x_{\mathrm{eq}} = 0.9$. (b) Injection flux of (a), represented as the derivative of x with respect to t.

j_{ex} is a constant, and a positive value of j indicates that hydrogen is inserted. Naturally, j returns to zero at $x = x_{\mathrm{eq}}$. Applying the same concept as in Eq. 5.9, and simplify the representation, the differential equation to be solved becomes

$$e^{-\frac{2(x+x_{\mathrm{eq}})}{\tau}} j_{\mathrm{ex}} \sqrt{\frac{1-x}{x}} \sqrt{\frac{1-x_{\mathrm{eq}}}{x_{\mathrm{eq}}}} \left(-\frac{e^{\frac{4x_{\mathrm{eq}}}{\tau}} x}{1-x} + \frac{e^{\frac{4x}{\tau}} x_{\mathrm{eq}}}{1-x_{\mathrm{eq}}} \right) = \frac{1}{\alpha_{\mathrm{S}} \Omega} \frac{\mathrm{d}x(t)}{\mathrm{d}t} . \tag{5.27}$$

A numerical solution to Eq. 5.27 is shown in Fig. 5.8(a) for the two cases with $x_{\mathrm{eq}} = 0.9$ and $x_{\mathrm{eq}} = 0.1$, each corresponding to the α' and α phases. The initial concentration x_{i}, i.e. x at $t = 0$, is 0.001, $\tau = 0.8$, and the value of j_{ex} is set to unity without loss of generality. In both cases, the solute fraction (H composition), x, increases over time until it saturates at x_{eq}. The injection flux, j, is proportional to the derivative of x and is plotted over time in Fig. 5.8(b). The flux is initially positive and it decreases to zero as the system approaches equilibrium. During the process, the flux for $x_{\mathrm{eq}} = 0.9$ case shows a slight increase. Such behavior is absent in the case of $x_{\mathrm{eq}} = 0.1$ when the system stays within the α phase, and rather pronounced when the system undergoes phase transformation. Experimental observation on this behavior would be beneficial to check the physical validity of the present model. From the $x-t$ curves as in Fig. 5.8(a), the half time is extracted as the time when x reaches $(x_{\mathrm{eq}} - x_{\mathrm{i}})/2$. This half time is plotted in Fig. 5.9 across the x_{eq} values, for an exemplary condition of $x_{\mathrm{i}} = 0.001$ and $\tau = 0.8$. The classical Butler-Volmer case, and the Butler-Volmer case modified to account for strain-dependent activation enthalpy are superimposed in blue and red, respectively for comparison. Both are plotted with an arbitrary scale factor. Note that the blue and red plots in Fig. 5.9 is identical to Fig. 5.5 and Fig. 5.6 with the same color, with unstable compositions excluded. The model prediction in Fig. 5.9 shows good agreement with the experimental observations in [167], successfully capturing the effect of the miscibility gap, particularly near the phase transformation region.

One might question the maximum concentration of H in Pd when comparing the outcome of this model to the experimental data in Fig. 5.9. The current model assumes

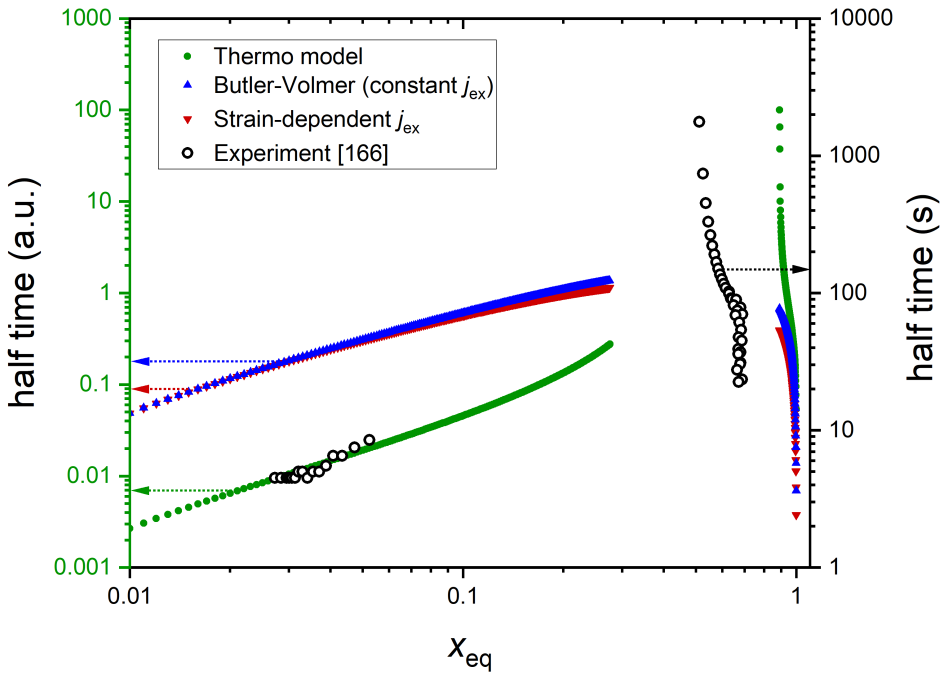

Figure 5.9: Half time of the hydrogen injection process as a function of equilibrium hydrogen concentration, x_{eq}, shown in arbitrary units. Green circles, the new rate law modeled from a thermodynamic perspective. Blue triangles, the classical Butler-Volmer-type reaction, with an arbitrary scale factor. Red inverted triangles, the Butler-Volmer-type reaction modified to account for strain-dependent activation enthalpy. Unstable compositions are excluded. Black circles, experimental data recreated from [167].

that the maximum possible x equals 1, based on the number of octahedral interstitial sites in the Pd lattice that can be occupied by H. However, achieving a highly hydrided Pd in practical, typically $x_{eq} \gtrapprox 0.7$, is challenging and requires extreme conditions [242, 243]. This limitation can be explained through the orbital configuration of Pd. The electronic structure of a free Pd atom corresponds to $[\mathrm{Kr}]4d^{10}5s^0$, while in metallic Pd, the $4d$ electrons form a conduction band that is only partially filled. The $4d$ band also interacts with hydrogen, creating new hybridized electronic states that are essential for stabilizing hydrogen in the Pd lattice. The electronic states associated with the d-orbital bonding are nearly saturated near a H concentration of 0.7. Beyond this, strong electronic repulsion occurs between the electrons in the $4d$ orbitals and the incoming hydrogen atoms, requiring significant energy input for further hydrogen accommodation [244]. The proposed model does not reflect such orbital configurational effects and this requires a separate approach.

Chapter 6

Summary and outlook

6.1 Summary of key findings

This thesis explores the relationship between the microstructural characteristics of network nanomaterials and their mechanical properties, and applies these insights to enhance the functional performance of nanoporous metals.

The first section of this thesis proposes a scaling relation on the mechanical stiffness of nanoporous materials, with a particular emphasis on the influence of microstructure topology. Here, np Au is examined as a standard model material for random network nanostructures and specifically their mechanics. The mechanical behavior of such open-cell foam structures has been expressed by classical Gibson-Ashby relations which highlight the solid volume fraction as the most obvious descriptor of stiffness. Yet, from the systematic deviation from the Gibson-Ashby relations, a measure of the networks' connectivity, is introduced as an additional microstructural descriptor. Connectivity is quantitatively parameterized by scaled topological genus, which represents the number of connections within a representative volume element of the microstructure. The nature of the dependency of Young's modulus on scaled genus is inspected using the implications of the existing database, from experiment and simulation, as well as further simulation data for random networks with various scaled genera. The observations are condensed into a scaling law that explicitly involves the scaled genus as a topological contribution. The results suggest a common scaling that is broadly comparable to the experimental observations on np Au.

The proposed scaling was then inspected for the case of np Nb, a nanoporous material fabricated by liquid metal dealloying. The universality and applicability are assessed from jointly considering mechanical stiffness and tomographic reconstruction of np Nb, with an emphasis on the dealloying methods and the resulting structural variation. For this purpose, millimeter-sized np Nb samples were fabricated by dealloying Nb-Ni alloy in a liquid Mg bath. The microstructure and mechanical behavior of np Nb are characterized by X-ray nanotomography and compression tests, respectively. Compared to aqueous-dealloyed np Au with similar φ as a benchmark, Young's modulus of np Nb is found to be substantially lower. The low stiffness is correlated to the reduced microstructural connectivity in np Nb. Yet, it is revealed that this effect, on its own, is not sufficient and that additional factors should contribute. A significant increase in the coefficient of ligament size variation is observed from np Nb during

coarsening, suggesting that the porosity evolution in LMD-made np Nb is considerably less ordered compared to conventional aqueous dealloyed network materials such as np Au.

Furthermore, the nanoporous metal is expanded to nanoporous metal hydride by introducing hydrogen as a reversibly dissolved solute. Hydrogen exhibits relatively high solubility in Pd, where it can be surface-adsorbed or absorbed into the bulk material and cause lattice expansion. This property enables the np Pd-H system to function as a hydrogen sensor and actuator. The objective of this part is to investigate the influence of geometry on the processes accompanying hydrogen charging, with a focus on identifying and characterizing the limiting factor of kinetics. Nanoporous Pd samples were synthesized via electrochemical dealloying, followed by thermal coarsening. This process yields np Pd with a tunable nanoscale network structure, ranging from approximately 20 to >200 nm, allowing for precise control over specific surface area and diffusion length. Hydrogen concentration within the np Pd was controlled by applying an electric potential in an acidic medium, with hydrogen solubility and interaction dynamics studied using chronoamperometry and electrochemical impedance spectroscopy. The results suggest that interfacial hydrogen injection process plays a critical role in determining hydrogen charging rate, thereby emphasizing ligament size as the key structural factor influencing this process. The injection process is further examined within a thermodynamic framework, specifically in the context of the Pd-H miscibility gap. It is discussed how the Butler-Volmer equation can be adapted to model the injection rate consistent with the equation of state for the composition-dependent chemical potential at equilibrium in an interacting solid solution. The proposed kinetic model explains observations on how the characteristic charging time in np Pd-H varies with the composition. These insights, combined with the preceding findings, offer guidance for designing more responsive nanoporous metal-based actuators and enhancing the performance of integrated nanomaterials for functional applications.

6.2 Outlook

The findings of this thesis demonstrate a strong correlation between the microstructural geometry, mechanical properties, and functional performance of nanoporous metals. These insights offer valuable perspectives for optimizing their structural design in cost-effective applications. Future work is thus called for to address the open questions raised by this study.

First, the concept of g^2 scaling for the stiffness of random network materials, presented in the first part of this thesis, is based fundamentally on the load-bearing fraction of the solid. That concept might hold for more general types of microstructures beyond aqueous-dealloyed np Au, with a relevant modification. For instance, the numerical value of $g_0 = 2.25$ clearly cannot be applied to np Nb, and the observations on np Nb structures confirms that the scaling may require additional descriptors. Morphological aspects have been proposed in the recent literature [204, 213], yet their link to the mechanics awaits clarification and confirmation by experiment.

This is connected to the second issue, the inherent differences between LMD and aqueous dealloying and their influence on porosity evolution. A deviation was observed when the scaling relation derived from np Au was applied to np Nb, and that suggests

that the microstructures of LMD differ significantly from those of nanoporous metals dealloyed in aqueous solutions. In this thesis, the focus was on the microstructural characteristics that are observed in the final samples, and the comparative analysis of mechanical performance was expanded based on that. These observed structural differences, such as the degree of structural dispersion, can be attributed to the fundamental distinctions between the dealloying mechanisms. The ratio of corrosion rate (first stage dealloying) to coarsening rate (second stage dealloying) in LMD may differ from that in aqueous dealloying–or may even be absent–potentially resulting in distinct structural outcomes. This provides an incentive for future research on the mechanisms driving the LMD microstructure evolution [99] and the resulting geometrical differences from aqueous dealloying. This will establish a generalized scaling relation that combines descriptors and mechanical properties across a wider variety of network nanomaterials.

The third issue is followed by the outcome of Sec. 5.3.3. The analysis reveals that the charging kinetics of np Pd-H is primarily constrained by interfacial hydrogen transfer, with hydrogen diffusion within the bulk Pd occurring sufficiently fast to assume diffusion time negligible. This underscores the need for an examination of the surface adsorption to absorption process in greater detail. The activated jump of hydrogen atoms from the electrolyte to the bulk involves several intermediate states: surface-adsorbed, co-planar surface-adsorbed, sub-surface adsorbed, and interstitial sites within the bulk Pd lattice, and it may depend on the occupancy of the adsorption sites. Thus, understanding the distribution of energy levels across these states, identifying the location and magnitude of the dominant energy barrier, and determining how it influences the overall transfer process are critical to fully comprehend the hydrogen atom's pathway from the environment into the metal lattice. Since the time scale of the injection process cannot be captured by typical impedance spectroscopy, alternative approaches, such as potential jump tests, should be employed to investigate this phenomenon experimentally.

Lastly, an unresolved issue reported in Sec. 4.2.3 should be revisited. From the dilatometer measurement, the maximum actuation strain of np Pd-H is found to be dependent on ligament size. While this size dependency can be partially attributed to differences in surface area–particularly if UPD H is dominant–the strain caused by interstitial hydrogen in the α and α' phases cannot be fully interpreted by solubility measurements alone. To address this issue, particularly the lower strain observed in np Pd with larger ligaments despite consistent solubility, one can first extend the measurement time scale of the phase transformation by one or more orders of magnitude. This will ensure equilibrium is reached within the ligament of a few hundred nanometers. Another important consideration is that strain is measured during absorption, while charge is measured during desorption. The desorption curve is used to minimize charge interference from the hydrogen evolution reaction during absorption. Therefore, to improve the accuracy of the comparison, the dilatometer strain measurement should also be performed during desorption, ideally simultaneously with the potentiostat charge measurement. If the difference originates from intrinsic properties, changes in defect density or facet orientation [245] during the thermal coarsening process should also be considered. Then, further investigation into the size effect–spatial distribution of the hydride phase within individual ligaments–would be necessary. This presents a compelling research question, where 3D microstructure and phase analysis could be

employed. Future research in this area will not only deepen our understanding of the underlying mechanisms in small-scale metal-hydrogen systems but also contribute to the development of hydrogen-based energy systems [160], where hydrogen serves as an energy carrier for storage and conversion.

References

[1] Gibson, L. J. Mechanical Behavior of Metallic Foams. *Annual Review of Materials Science* **2000**, *30*, 191–227.

[2] Jang, W.-Y.; Kraynik, A. M.; Kyriakides, S. On the microstructure of open-cell foams and its effect on elastic properties. *International Journal of Solids and Structures* **2008**, *45*, 1845–1875.

[3] Picu, R. C. Mechanics of random fiber networks—a review. *Soft Matter* **2011**, *7*, 6768–6785.

[4] Pritchard, R. H.; Shery Huang, Y. Y.; Terentjev, E. M. Mechanics of biological networks: from the cell cytoskeleton to connective tissue. *Soft Matter* **2014**, *10*, 1864–1884.

[5] Biener, J.; Hodge, A. M.; Hayes, J. R.; Volkert, C. A.; Zepeda-Ruiz, L. A.; Hamza, A. V.; Abraham, F. F. Size effects on the mechanical behavior of nanoporous Au. *Nano Letters* **2006**, *6*, 2379–2382.

[6] Volkert, C. A.; Lilleodden, E. T.; Kramer, D.; Weissmuller, J. Approaching the theoretical strength in nanoporous Au. *Applied Physics Letters* **2006**, *89*, –.

[7] Hodge, A. M.; Biener, J.; Hayes, J. R.; Bythrow, P. M.; Volkert, C. A.; Hamza, A. V. Scaling equation for yield strength of nanoporous open-cell foams. *Acta Materialia* **2007**, *55*, 1343–1349.

[8] Jin, H.-J.; Weissmüller, J.; Farkas, D. Mechanical response of nanoporous metals: A story of size, surface stress, and severed struts. *Mrs Bulletin* **2018**, *43*, 35–42.

[9] Bauer, J.; Meza, L. R.; Schaedler, T. A.; Schwaiger, R.; Zheng, X.; Valdevit, L. Nanolattices: an emerging class of mechanical metamaterials. *Advanced Materials* **2017**, *29*, 1701850.

[10] Biener, J.; Hodge, A. M.; Hayes, J. R.; Volkert, C. A.; Zepeda-Ruiz, L. A.; Hamza, A. V.; Abraham, F. F. Size effects on the mechanical behavior of nanoporous Au. *Nano letters* **2006**, *6*, 2379–2382.

[11] Hodge, A.; Biener, J.; Hayes, J.; Bythrow, P.; Volkert, C.; Hamza, A. Scaling equation for yield strength of nanoporous open-cell foams. *Acta Materialia* **2007**, *55*, 1343–1349.

[12] Schaedler, T. A.; Jacobsen, A. J.; Torrents, A.; Sorensen, A. E.; Lian, J.; Greer, J. R.; Valdevit, L.; Carter, W. B. Ultralight metallic microlattices. *Science* **2011**, *334*, 962–965.

[13] Schwaiger, R.; Meza, L. R.; Li, X. The extreme mechanics of micro- and nanoarchitected materials. *MRS Bulletin* **2019**, *44*, 758–765.

[14] Greer, J. R.; Deshpande, V. S. Three-dimensional architected materials and structures: Design, fabrication, and mechanical behavior. *MRS Bulletin* **2019**, *44*, 750–757.

[15] Shi, S.; Li, Y.; Ngo-Dinh, B.-N.; Markmann, J.; Weissmüller, J. Scaling behavior of stiffness and strength of hierarchical network nanomaterials. *Science* **2021**, *371*, 1026.

[16] Guell Izard, A.; Bauer, J.; Crook, C.; Turlo, V.; Valdevit, L. Ultrahigh energy absorption multifunctional spinodal nanoarchitectures. *Small* **2019**, *15*, 1903834.

[17] Lee, M. N.; Mohraz, A. Bicontinuous macroporous materials from bijel templates. *Advanced Materials* **2010**, *22*, 4836–4841.

[18] Hsieh, M.-T.; Endo, B.; Zhang, Y.; Bauer, J.; Valdevit, L. The mechanical response of cellular materials with spinodal topologies. *Journal of the Mechanics and Physics of Solids* **2019**, *125*, 401–419.

[19] McCue, I.; Karma, A.; Erlebacher, J. Pattern formation during electrochemical and liquid metal dealloying. *Mrs Bulletin* **2018**, *43*, 27–34.

[20] Erlebacher, J.; Aziz, M. J.; Karma, A.; Dimitrov, N.; Sieradzki, K. Evolution of nanoporosity in dealloying. *Nature* **2001**, *410*, 450–453.

[21] Wittstock, G.; Bäumer, M.; Dononelli, W.; Klüner, T.; Lührs, L.; Mahr, C.; Moskaleva, L. V.; Oezaslan, M.; Risse, T.; Rosenauer, A.; Staubitz, A.; Weissmüller, J.; Wittstock, A. Nanoporous Gold: From Structure Evolution to Functional Properties in Catalysis and Electrochemistry. *Chemical Reviews* **2023**, *123*, 6716–6792.

[22] Cahn, J. W. Phase Separation by Spinodal Decomposition in Isotropic Systems. *The Journal of Chemical Physics* **1965**, *42*, 93–99.

[23] Berk, N. F. Scattering properties of a model bicontinuous structure with a well defined length scale. *Phys Rev Lett* **1987**, *58*, 2718–2721.

[24] Teubner, M. Level Surfaces of Gaussian Random Fields and Microemulsions. *Europhysics Letters* **1991**, *14*, 403.

[25] Li, J. C.; Ross, D. K. Dynamical scaling for spinodal decomposition - a small-angle neutron scattering study of porous Vycor glass with fractal properties. *Journal of Physics: Condensed Matter* **1994**, *6*, 351–362.

[26] Roberts, A.; Garboczi, E. J. Computation of the linear elastic properties of random porous materials with a wide variety of microstructure. *Proceedings of the Royal Society of London A: Mathematical, Physical and Engineering Sciences* **2002**, *458*, 1033–1054.

[27] Roberts, A. P.; Garboczi, E. J. Elastic properties of model random three-dimensional open-cell solids. *Journal of the Mechanics and Physics of Solids* **2002**, *50*, 33–55.

[28] Gommes, C. J. Stochastic models of disordered mesoporous materials for small-angle scattering analysis and more. *Microporous and Mesoporous Materials* **2018**, *257*, 62–78.

[29] Jin, H. J.; Kurmanaeva, L.; Schmauch, J.; Rösner, H.; Ivanisenko, Y.; Weissmüller, J. Deforming nanoporous metal: Role of lattice coherency. *Acta Materialia* **2009**, *57*, 2665–2672.

[30] Briot, N. J.; Kennerknecht, T.; Eberl, C.; Balk, T. J. Mechanical properties of bulk single crystalline nanoporous gold investigated by millimetre-scale tension and compression testing. *Philosophical Magazine* **2014**, *94*, 847–866.

[31] Briot, N. J.; Balk, T. J. Developing scaling relations for the yield strength of nanoporous gold. *Philosophical Magazine* **2015**, *95*, 2955–2973.

[32] Mameka, N.; Wang, K.; Markmann, J.; Lilleodden, E.; Weissmüller, J. Nanoporous Gold—Testing Macro-scale Samples to Probe Small-scale Mechanical Behavior. *Materials Research Letters* **2016**, *4*, 27–36.

[33] Badwe, N.; Chen, X.; Sieradzki, K. Mechanical properties of nanoporous gold in tension. *Acta Materialia* **2017**, *129*, 251–258.

[34] McCue, I.; Benn, E.; Gaskey, B.; Erlebacher, J. Dealloying and dealloyed materials. *Annual review of materials research* **2016**, *46*, 263–286.

[35] Greer, J. R.; Deshpande, V. S. Three-dimensional architected materials and structures: Design, fabrication, and mechanical behavior. *MRS Bulletin* **2019**, *44*, 750–757.

[36] Shi, S.; Li, Y.; Ngo-Dinh, B.-N.; Markmann, J.; Weissmüller, J. Scaling behavior of stiffness and strength of hierarchical network nanomaterials. *Science* **2021**, *371*, 1026–1033.

[37] Ding, Y.; Chen, M. W. Nanoporous Metals for Catalytic and Optical Applications. *MRS Bulletin* **2009**, *34*, 569–576.

[38] Wittstock, G.; Bäumer, M.; Dononelli, W.; Kluüner, T.; Lührs, L.; Mahr, C.; Moskaleva, L. V.; Oezaslan, M.; Risse, T.; Rosenauer, A.; others Nanoporous gold: From structure evolution to functional properties in catalysis and electrochemistry. *Chemical Reviews* **2023**, *123*, 6716–6792.

[39] Zhang, J.; Bai, Q.; Zhang, Z. Dealloying-driven nanoporous palladium with superior electrochemical actuation performance. *Nanoscale* **2016**, *8*, 7287–95.

[40] Shi, S.; Markmann, J.; Weissmüller, J. Actuation by hydrogen electrosorption in hierarchical nanoporous palladium. *Philosophical Magazine* **2017**, *97*, 1571–1587.

[41] Jin, H.-J.; Wang, X.-L.; Parida, S.; Wang, K.; Seo, M.; Weissmüller, J. Nanoporous Au- Pt alloys as large strain electrochemical actuators. *Nano letters* **2010**, *10*, 187–194.

[42] Dietrich, L.; Oppermann, H.; Lopper, C.; Mackowiak, P. Fabrication and Characterization of Nanoporous Gold (NPG) Interconnects for Wafer Level Packaging. 2022 IEEE 72nd Electronic Components and Technology Conference (ECTC). 2022; pp 873–882.

[43] Kucheyev, S. O.; Hayes, J. R.; Biener, J.; Huser, T.; Talley, C. E.; Hamza, A. V. Surface-enhanced Raman scattering on nanoporous Au. *Applied Physics Letters* **2006**, *89*, –.

[44] Qian, L. H.; Yan, X. Q.; Fujita, T.; Inoue, A.; Chen, M. W. Surface enhanced Raman scattering of nanoporous gold: Smaller pore sizes stronger enhancements. *Applied Physics Letters* **2007**, *90*.

[45] Seker, E.; Shih, W.-C.; Stine, K. J. Nanoporous metals by alloy corrosion: Bioanalytical and biomedical applications. *MRS Bulletin* **2018**, *43*, 49–56.

[46] Stenner, C.; Shao, L.-H.; Mameka, N.; Weissmüller, J. Piezoelectric gold: strong charge-load response in a metal-based hybrid nanomaterial. *Advanced functional materials* **2016**, *26*, 5174–5181.

[47] Jin, H.-J.; Weissmüller, J. A material with electrically tunable strength and flow stress. *Science* **2011**, *332*, 1179–1182.

[48] Bringa, E. M.; Monk, J.; Caro, A.; Misra, A.; Zepeda-Ruiz, L.; Duchaineau, M.; Abraham, F.; Nastasi, M.; Picraux, S.; Wang, Y.; others Are nanoporous materials radiation resistant? *Nano letters* **2012**, *12*, 3351–3355.

[49] Li, R.; Sieradzki, K. Ductile-Brittle Transition in Random Porous Au. *Physical Review Letters* **1992**, *68*, 1168–1171.

[50] Senior, N. A.; Newman, R. C. Synthesis of tough nanoporous metals by controlled electrolytic dealloying. *Nanotechnology* **2006**, *17*, 2311–2316.

[51] Jin, H.-J.; Kurmanaeva, L.; Schmauch, J.; Rösner, H.; Ivanisenko, Y.; Weissmüller, J. Deforming nanoporous metal: Role of lattice coherency. *Acta Materialia* **2009**, *57*, 2665–2672.

[52] Briot, N. J.; Kennerknecht, T.; Eberl, C.; Balk, T. J. Mechanical properties of bulk single crystalline nanoporous gold investigated by millimetre-scale tension and compression testing. *Philosophical Magazine* **2014**, *94*, 847–866.

[53] Zandersons, B.; Lührs, L.; Li, Y.; Weissmüller, J. On factors defining the mechanical behavior of nanoporous gold. *Acta Materialia* **2021**, *215*, 116979.

[54] Volkert, C.; Lilleodden, E.; Kramer, D.; Weissmüller, J. Approaching the theoretical strength in nanoporous Au. *Applied Physics Letters* **2006**, *89*, 061920.

[55] Liu, R.; Antoniou, A. A relationship between the geometrical structure of a nanoporous metal foam and its modulus. *Acta Materialia* **2013**, *61*, 2390–2402.

[56] Briot, N. J.; Balk, T. J. Developing scaling relations for the yield strength of nanoporous gold. *Philosophical Magazine* **2015**, *95*, 2955–2973.

[57] Jeon, H.; Lee, S.; Kim, J.-Y. Tension-compression asymmetry in plasticity of nanoporous gold. *Acta Materialia* **2020**, *199*, 340–351.

[58] Wu, Y.; Markmann, J.; Lilleodden, E. T. On the consequences of intrinsic and extrinsic size effects on the mechanical response of nanoporous Au. *Materials & Design* **2023**, *232*, 112175.

[59] Gibson, L. J.; Ashby, M. F. The mechanics of three-dimensional cellular materials. *Proceedings of the Royal Society of London A: Mathematical, Physical and Engineering Sciences* **1982**, *382*, 43–59.

[60] Huber, N.; Viswanath, R. N.; Mameka, N.; Markmann, J.; Weissmüller, J. Scaling laws of nanoporous metals under uniaxial compression. *Acta Materialia* **2014**, *67*, 252–265.

[61] Liu, H.; Abdolrahim, N. A modified scaling law for stiffness of nanoporous materials based on gyroid cell model. *International Journal of Mechanical Sciences* **2020**, *166*, 105223.

[62] Liu, L.-Z.; Ye, X.-L.; Jin, H.-J. Interpreting anomalous low-strength and low-stiffness of nanoporous gold: Quantification of network connectivity. *Acta Materialia* **2016**, *118*, 77–87.

[63] Liu, L.-Z.; Jin, H.-J. Scaling equation for the elastic modulus of nanoporous gold with "fixed" network connectivity. *Applied Physics Letters* **2017**, *110*, 211902.

[64] Lilleodden, E. T.; Voorhees, P. W. On the topological, morphological, and microstructural characterization of nanoporous metals. *MRS bulletin* **2018**, *43*, 20–26.

[65] Huber, N. Connections between topology and macroscopic mechanical properties of three-dimensional open-pore materials. *Frontiers in Materials* **2018**,

[66] Soyarslan, C.; Bargmann, S.; Pradas, M.; Weissmüller, J. 3D stochastic bicontinuous microstructures: Generation, topology and elasticity. *Acta Materialia* **2018**, *149*, 326–340.

[67] Detsi, E.; Selles, M. S.; Onck, P. R.; De Hosson, J. T. M. Nanoporous silver as electrochemical actuator. *Scripta Materialia* **2013**, *69*, 195–198.

[68] Wang, C.; Chen, Q. Reduction-Induced Decomposition: Spontaneous Formation of Monolithic Nanoporous Metals of Tunable Structural Hierarchy and Porosity. *Chemistry of Materials* **2018**, *30*, 3894–3900.

[69] Jin, H.-J.; Kramer, D.; Ivanisenko, Y.; Weissmüller, J. Macroscopically strong nanoporous Pt prepared by dealloying. *Advanced Engineering Materials* **2007**, *9*, 849–854.

[70] Harrison, J. D.; Wagner, C. The attack of solid alloys by liquid metals and salt melts. *Acta Metallurgica* **1959**, *7*, 722–735.

[71] Wada, T.; Yubuta, K.; Inoue, A.; Kato, H. Dealloying by metallic melt. *Materials Letters* **2011**, *65*, 1076–1078.

[72] Okulov, I.; Weissmüller, J.; Markmann, J. Dealloying-based interpenetrating-phase nanocomposites matching the elastic behavior of human bone. *Scientific reports* **2017**, *7*, 1–7.

[73] Berger, S. A.; Okulov, I. V. Open porous $\alpha+\ \beta$ titanium alloy by liquid metal dealloying for biomedical applications. *Metals* **2020**, *10*, 1450.

[74] Xiang, Y.-H.; Liu, L.-Z.; Shao, J.-C.; Jin, H.-J. A universal scaling relationship between the strength and Young's modulus of dealloyed porous Fe0. 80Cr0. 20. *Acta Materialia* **2020**, *186*, 105–115.

[75] Mokhtari, M.; Wada, T.; Le Bourlot, C.; Mary, N.; Duchet-Rumeau, J.; Kato, H.; Maire, É. Low cost high specific surface architectured nanoporous metal with corrosion resistance produced by liquid metal dealloying from commercial nickel superalloy. *Scripta Materialia* **2019**, *163*, 5–8.

[76] Kim, J. W.; Wada, T.; Kim, S. G.; Kato, H. Enlarging the surface area of an electrolytic capacitor of porous niobium by MgCe eutectic liquid dealloying. *Scripta Materialia* **2016**, *122*, 68–71.

[77] Zhao, C.; Wada, T.; De Andrade, V.; Williams, G. J.; Gelb, J.; Li, L.; Thieme, J.; Kato, H.; Chen-Wiegart, Y.-c. K. Three-dimensional morphological and chemical evolution of nanoporous stainless steel by liquid metal dealloying. *ACS applied materials & interfaces* **2017**, *9*, 34172–34184.

[78] Okulov, A. V.; Joo, S.-H.; Kim, H. S.; Kato, H.; Okulov, I. V. Nanoporous high-entropy alloy by liquid metal dealloying. *Metals* **2020**, *10*, 1396.

[79] Veleckis, E.; Edwards, R. K. Thermodynamic properties in the systems vanadium-hydrogen, niobium-hydrogen, and tantalum-hydrogen. *The Journal of Physical Chemistry* **1969**, *73*, 683–692.

[80] Manchester, F.; San-Martin, A.; Pitre, J. The H-Pd (hydrogen-palladium) system. *Journal of phase equilibria* **1994**, *15*, 62–83.

[81] Erlebacher, J.; Seshadri, R. Hard materials with tunable porosity. *Mrs Bulletin* **2009**, *34*, 561–568.

[82] Mameka, N.; Wang, K.; Markmann, J.; Lilleodden, E. T.; Weissmüller, J. Nanoporous gold—testing macro-scale samples to probe small-scale mechanical behavior. *Materials Research Letters* **2016**, *4*, 27–36.

[83] Erlebacher, J.; Aziz, M. J.; Karma, A.; Dimitrov, N.; Sieradzki, K. Evolution of nanoporosity in dealloying. *nature* **2001**, *410*, 450–453.

[84] Ye, X.-L.; Lu, N.; Li, X.-J.; Du, K.; Tan, J.; Jin, H.-J. Primary and secondary dealloying of Au (Pt)-Ag: structural and compositional evolutions, and volume shrinkage. *Journal of The Electrochemical Society* **2014**, *161*, C517.

[85] Chen-Wiegart, Y.-c. K.; Wang, S.; Chu, Y. S.; Liu, W.; McNulty, I.; Voorhees, P. W.; Dunand, D. C. Structural evolution of nanoporous gold during thermal coarsening. *Acta Materialia* **2012**, *60*, 4972–4981.

[86] Graf, M.; Roschning, B.; Weissmüller, J. Nanoporous gold by alloy corrosion: Method-structure-property relationships. *Journal of The Electrochemical Society* **2017**, *164*, C194.

[87] Rouya, E.; Cattarin, S.; Reed, M.; Kelly, R.; Zangari, G. Electrochemical characterization of the surface area of nanoporous gold films. *Journal of The Electrochemical Society* **2012**, *159*, K97.

[88] Tan, Y. H.; Davis, J. A.; Fujikawa, K.; Ganesh, N. V.; Demchenko, A. V.; Stine, K. J. Surface area and pore size characteristics of nanoporous gold subjected to thermal, mechanical, or surface modification studied using gas adsorption isotherms, cyclic voltammetry, thermogravimetric analysis, and scanning electron microscopy. *Journal of materials chemistry* **2012**, *22*, 6733–6745.

[89] Li, J.; Markmann, J.; Weissmüller, J.; Mameka, N. Nanoporous gold-polypyrrole hybrid electrochemical actuators with tunable elasticity. *Acta materialia* **2021**, *212*, 116852.

[90] Wang, K.; Stenner, C.; Weissmüller, J. A nanoporous gold-polypyrrole hybrid nanomaterial for actuation. *Sensors and Actuators B: Chemical* **2017**, *248*, 622–629.

[91] Gnegel, S.; Li, J.; Mameka, N.; Huber, N.; Düster, A. Numerical investigation of polymer coated nanoporous gold. *Materials* **2019**, *12*, 2178.

[92] Roschning, B.; Weissmüller, J. Nanoporous-Gold-Polypyrrole Hybrid Materials for Millimeter-Sized Free Standing Actuators. *Advanced materials interfaces* **2020**, *7*, 2001415.

[93] Detsi, E.; Onck, P.; De Hosson, J. T. M. Metallic muscles at work: High rate actuation in nanoporous gold/polyaniline composites. *Acs Nano* **2013**, *7*, 4299–4306.

[94] Wang, K.; Kobler, A.; Kübel, C.; Jelitto, H.; Schneider, G.; Weissmüller, J. Nanoporous-gold-based composites: toward tensile ductility. *NPG Asia materials* **2015**, *7*, e187–e187.

[95] McCue, I.; Gaskey, B.; Geslin, P.-A.; Karma, A.; Erlebacher, J. Kinetics and morphological evolution of liquid metal dealloying. *Acta Materialia* **2016**, *115*, 10–23.

[96] Takeuchi, A.; Inoue, A. Classification of bulk metallic glasses by atomic size difference, heat of mixing and period of constituent elements and its application to characterization of the main alloying element. *Materials transactions* **2005**, *46*, 2817–2829.

[97] Kim, J. W.; Tsuda, M.; Wada, T.; Yubuta, K.; Kim, S. G.; Kato, H. Optimizing niobium dealloying with metallic melt to fabricate porous structure for electrolytic capacitors. *Acta Materialia* **2015**, *84*, 497–505.

[98] Zednicek, T.; Vrana, B.; Millman, W.; Reynolds, C. Tantalum and niobium technology roadmap. CARTS-CONFERENCE-. 2002; pp 142–147.

[99] Geslin, P.-A.; McCue, I.; Gaskey, B.; Erlebacher, J.; Karma, A. Topology-generating interfacial pattern formation during liquid metal dealloying. *Nature communications* **2015**, *6*, 1–8.

[100] Wada, T.; Kato, H. Three-dimensional open-cell macroporous iron, chromium and ferritic stainless steel. *Scripta Materialia* **2013**, *68*, 723–726.

[101] Erlebacher, J. Mechanism of coarsening and bubble formation in high-genus nanoporous metals. *Physical review letters* **2011**, *106*, 225504.

[102] Joo, S.-H.; Wada, T.; Kato, H. Development of porous FeCo by liquid metal dealloying: Evolution of porous morphology and effect of interaction between ligaments and melt. *Materials & Design* **2019**, *180*, 107908.

[103] Chen-Wiegart, Y.-c. K.; Wada, T.; Butakov, N.; Xiao, X.; De Carlo, F.; Kato, H.; Wang, J.; Dunand, D. C.; Maire, E. 3D morphological evolution of porous titanium by X-ray micro-and nano-tomography. *Journal of Materials Research* **2013**, *28*, 2444–2452.

[104] Ashby, M. F. The properties of foams and lattices. *Philosophical Transactions of the Royal Society A: Mathematical, Physical and Engineering Sciences* **2006**, *364*, 15–30.

[105] Gibson, L. J.; Ashby, M. F. *Cellular solids: structure and properties*; Cambridge university press, 1999.

[106] Gibson, L. J.; Ashby, M. F. The mechanics of three-dimensional cellular materials. *Proceedings of the Royal Society of London A: Mathematical, Physical and Engineering Sciences* **1982**, *382*, 43–59.

[107] Hodge, A.; Doucette, R.; Biener, M.; Biener, J.; Cervantes, O.; Hamza, A. Ag effects on the elastic modulus values of nanoporous Au foams. *Journal of Materials Research* **2009**, *24*, 1600–1606.

[108] Liu, L.-Z.; Jin, H.-J. Scaling equation for the elastic modulus of nanoporous gold with "fixed" network connectivity. *Applied Physics Letters* **2017**, *110*.

[109] Ngô, B.-N. D.; Stukowski, A.; Mameka, N.; Markmann, J.; Albe, K.; Weissmüller, J. Anomalous compliance and early yielding of nanoporous gold. *Acta Materialia* **2015**, *93*, 144–155.

[110] Roschning, B.; Huber, N. Scaling laws of nanoporous gold under uniaxial compression: Effects of structural disorder on the solid fraction, elastic Poisson's ratio, Young's modulus and yield strength. *Journal of the Mechanics and Physics of Solids* **2016**, *92*, 55–71.

[111] Sun, X.-Y.; Xu, G.-K.; Li, X.; Feng, X.-Q.; Gao, H. Mechanical properties and scaling laws of nanoporous gold. *Journal of Applied Physics* **2013**, *113*, 023505.

[112] Jiao, J.; Huber, N. Deformation mechanisms in nanoporous metals: Effect of ligament shape and disorder. *Computational Materials Science* **2017**, *127*, 194–203.

[113] Roberts, A. P.; Garboczi, E. J. Elastic moduli of model random three-dimensional closed-cell cellular solids. *Acta materialia* **2001**, *49*, 189–197.

[114] Mameka, N. Surface-controlled mechanical properties of bulk nanoporous gold. Ph.D. thesis, Technische Universität Hamburg-Harburg, 2016.

[115] Badwe, N.; Chen, X.; Sieradzki, K. Mechanical properties of nanoporous gold in tension. *Acta Materialia* **2017**, *129*, 251–258.

[116] Greer, J. R.; Nix, W. D. Size dependence of mechanical properties of gold at the sub-micron scale. *Applied Physics A* **2005**, *80*, 1625–1629.

[117] Lührs, L.; Weissmüller, J. Nanoporous Copper-Nickel–Macroscopic bodies of a strong and deformable nanoporous base metal by dealloying. *Scripta Materialia* **2018**, *155*, 119–123.

[118] Dou, R.; Derby, B. The strength of gold nanowire forests. *Scripta materialia* **2008**, *59*, 151–154.

[119] Volkert, C. A.; Lilleodden, E. T. Size effects in the deformation of sub-micron Au columns. *Philosophical Magazine* **2006**, *86*, 5567–5579.

[120] Ashby, M. The deformation of plastically non-homogeneous materials. *The Philosophical Magazine: A Journal of Theoretical Experimental and Applied Physics* **1970**, *21*, 399–424.

[121] Balint, D.; Deshpande, V.; Needleman, A.; Van der Giessen, E. A discrete dislocation plasticity analysis of grain-size strengthening. *Materials Science and Engineering: A* **2005**, *400*, 186–190.

[122] Nix, W. D.; Greer, J. R.; Feng, G.; Lilleodden, E. T. Deformation at the nanometer and micrometer length scales: Effects of strain gradients and dislocation starvation. *Thin Solid Films* **2007**, *515*, 3152–3157.

[123] Brenner, S. S. Tensile strength of whiskers. *Journal of applied physics* **1956**, *27*, 1484–1491.

[124] Huang, P.; Yu, Q. Dislocation multiplications in extremely small hexagonal-structured titanium nanopillars without dislocation starvation. *Scientific reports* **2017**, *7*, 1–5.

[125] Schneider, A.; Kaufmann, D.; Clark, B.; Frick, C.; Gruber, P.; Mönig, R.; Kraft, O.; Arzt, E. Correlation between critical temperature and strength of small-scale bcc pillars. *Physical review letters* **2009**, *103*, 105501.

[126] Suzuki, T.; Koizumi, H.; Kirchner, H. O. Plastic flow stress of bcc transition metals and the Peierls potential. *Acta metallurgica et materialia* **1995**, *43*, 2177–2187.

[127] Uchic, M. D.; Dimiduk, D. M.; Florando, J. N.; Nix, W. D. Sample dimensions influence strength and crystal plasticity. *Science* **2004**, *305*, 986–989.

[128] Frick, C.; Clark, B.; Orso, S.; Schneider, A.; Arzt, E. Size effect on strength and strain hardening of small-scale [1 1 1] nickel compression pillars. *Materials Science and Engineering: A* **2008**, *489*, 319–329.

[129] Brinckmann, S.; Kim, J.-Y.; Greer, J. R. Fundamental Differences in Mechanical Behavior between Two Types of Crystals<? format?> at the Nanoscale. *Physical review letters* **2008**, *100*, 155502.

[130] Schneider, A.; Clark, B.; Frick, C.; Gruber, P.; Arzt, E. Effect of orientation and loading rate on compression behavior of small-scale Mo pillars. *Materials Science and Engineering: A* **2009**, *508*, 241–246.

[131] Weiss, J.; Zhang, P.; Cheng, P.; Liu, G. Contrasting the nature of plastic fluctuations in small-sized systems of BCC and FCC materials. *Journal of Materials Science: Materials Theory* **2024**, *8*, 8.

[132] Seeger, A.; Wüthrich, C. Dislocation relaxation processes in body-centred cubic metals. *Il Nuovo Cimento B (1971-1996)* **1976**, *33*, 38–75.

[133] Vitek, V. Structure of dislocation cores in metallic materials and its impact on their plastic behaviour. *Progress in materials science* **1992**, *36*, 1–27.

[134] Woodward, C.; Rao, S. Flexible ab initio boundary conditions: Simulating isolated dislocations in bcc Mo and Ta. *Physical review letters* **2002**, *88*, 216402.

[135] Cai, W.; Bulatov, V. V.; Chang, J.; Li, J.; Yip, S. *Dislocations in solids*; Elsevier, 2004; Vol. 12; pp 1–80.

[136] Ziehmer, M.; Hu, K.; Wang, K.; Lilleodden, E. T. A principle curvatures analysis of the isothermal evolution of nanoporous gold: Quantifying the characteristic length-scales. *Acta materialia* **2016**, *120*, 24–31.

[137] Mangipudi, K. R.; Epler, E.; Volkert, C. A. Topology-dependent scaling laws for the stiffness and strength of nanoporous gold. *Acta Materialia* **2016**, *119*, 115–122.

[138] Kwon, Y.; Thornton, K.; Voorhees, P. Morphology and topology in coarsening of domains via non-conserved and conserved dynamics. *Philosophical Magazine* **2010**, *90*, 317–335.

[139] Hu, K.; Ziehmer, M.; Wang, K.; Lilleodden, E. T. Nanoporous gold: 3D structural analyses of representative volumes and their implications on scaling relations of mechanical behaviour. *Philosophical Magazine* **2016**, 1–14.

[140] Li, Y.; Ngô, B.-N. D.; Markmann, J.; Weissmüller, J. Topology evolution during coarsening of nanoscale metal network structures. *Physical review materials* **2019**, *3*, 076001.

[141] Fukai, Y. *The metal-hydrogen system: basic bulk properties*; Springer Science & Business Media, 2006; Vol. 21.

[142] Berlinguette, C. P.; Chiang, Y.-M.; Munday, J. N.; Schenkel, T.; Fork, D. K.; Koningstein, R.; Trevithick, M. D. Revisiting the cold case of cold fusion. *Nature* **2019**, *570*, 45–51.

[143] Wicke, E.; Brodowsky, H.; Züchner, H. Hydrogen in palladium and palladium alloys. *Hydrogen in Metals II: Application-Oriented Properties* **2005**, 73–155.

[144] Adams, B. D.; Chen, A. The role of palladium in a hydrogen economy. *Materials today* **2011**, *14*, 282–289.

[145] Yang, T.-h.; Pyun, S.-i. Hydrogen absorption and diffusion into and in palladium: ac-impedance analysis under impermeable boundary conditions. *Electrochimica acta* **1996**, *41*, 843–848.

[146] Fukai, Y.; Ōkuma, N. Formation of superabundant vacancies in Pd hydride under high hydrogen pressures. *Physical review letters* **1994**, *73*, 1640.

[147] Peisl, H. Lattice strains due to hydrogen in metals. *Hydrogen in metals I: Basic properties* **2005**, 53–74.

[148] Gong, J.; Wang, Z.; Tang, Y.; Sun, J.; Wei, X.; Zhang, Q.; Tian, G.; Wang, H. MEMS-based resistive hydrogen sensor with high performance using a palladium-gold alloy thin film. *Journal of Alloys and Compounds* **2023**, *930*, 167398.

[149] RaviPrakash, J.; McDaniel, A.; Horn, M.; Pilione, L.; Sunal, P.; Messier, R.; McGrath, R.; Schweighardt, F. Hydrogen sensors: Role of palladium thin film morphology. *Sensors and Actuators B: Chemical* **2007**, *120*, 439–446.

[150] Durst, J.; Siebel, A.; Simon, C.; Hasché, F.; Herranz, J.; Gasteiger, H. New insights into the electrochemical hydrogen oxidation and evolution reaction mechanism. *Energy & Environmental Science* **2014**, *7*, 2255–2260.

[151] Chan, C. T.; Louie, S. G. Electronic structure of subsurface and surface chemisorption for hydrogen on the Pd (111) surface. *Solid state communications* **1983**, *48*, 417–420.

[152] Eberhardt, W.; Greuter, F.; Plummer, E. Bonding of H to Ni, Pd, and Pt surfaces. *Physical Review Letters* **1981**, *46*, 1085.

[153] Santos, E.; Hindelang, P.; Quaino, P.; Schmickler, W. A model for the Heyrovsky reaction as the second step in hydrogen evolution. *Physical Chemistry Chemical Physics* **2011**, *13*, 6992–7000.

[154] Jerkiewicz, G. Hydrogen sorption ATIN electrodes. *Progress in surface science* **1998**, *57*, 137–186.

[155] Breiter, M. Comparative electrochemical study of hydrogen and deuterium adsorption on platinum. *Transactions of the Faraday Society* **1964**, *60*, 1445–1449.

[156] Jerkiewicz, G.; Zolfaghari, A. Comparison of hydrogen electroadsorption from the electrolyte with hydrogen adsorption from the gas phase. *Journal of The Electrochemical Society* **1996**, *143*, 1240.

[157] Protopopoff, E.; Marcus, P. Effects of chemisorbed sulphur on the hydrogen adsorption and evolution on metal single crystal surfaces. *Journal de chimie physique* **1991**, *88*, 1423–1452.

[158] Sung, Y.-E.; Chrzanowski, W.; Zolfaghari, A.; Jerkiewicz, G.; Wieckowski, A. Structure of chemisorbed sulfur on a Pt (111) electrode. *Journal of the American Chemical Society* **1997**, *119*, 194–200.

[159] Johnson, N. J.; Lam, B.; MacLeod, B. P.; Sherbo, R. S.; Moreno-Gonzalez, M.; Fork, D. K.; Berlinguette, C. P. Facets and vertices regulate hydrogen uptake and release in palladium nanocrystals. *Nature materials* **2019**, *18*, 454–458.

[160] Jerkiewicz, G. Electrochemical hydrogen adsorption and absorption. Part 1: Under-potential deposition of hydrogen. *Electrocatalysis* **2010**, *1*, 179–199.

[161] Dickinson, E. J.; Wain, A. J. The Butler-Volmer equation in electrochemical theory: Origins, value, and practical application. *Journal of Electroanalytical Chemistry* **2020**, *872*, 114145.

[162] White, R. E.; Lorimer, S.; Darby, R. Prediction of the current density at an electrode at which multiple electrode reactions occur under potentiostatic control. *Journal of The Electrochemical Society* **1983**, 1123.

[163] Simhofer, M.; Brunner, P.; Weissmüller, J.; Würschum, R. Diffusion–reaction modelling of modulated hydrogen loading. *Philosophical Magazine* **2024**, 1–34.

[164] Nash, P.; Nash, A. The Nb- Ni (niobium-nickel) system. *Bulletin of Alloy Phase Diagrams* **1986**, *7*, 124–130.

[165] Okamoto, H. Nb-Ni (niobium-nickel). *Journal of phase equilibria and diffusion* **1998**, *19*, 289.

[166] Subramanian, P.; Laughlin, D. Cu-Pd (copper-palladium). *Journal of phase equilibria* **1991**, *12*, 231–243.

[167] Shi, S. Chemo-mechanical coupling in nanoporous palladium-hydrogen. Ph.D. thesis, 2019.

[168] Mameka, N.; Markmann, J.; Jin, H.-J.; Weissmüller, J. Electrical stiffness modulation—confirming the impact of surface excess elasticity on the mechanics of nanomaterials. *Acta materialia* **2014**, *76*, 272–280.

[169] Pia, G.; Delogu, F. Coarsening of nanoporous Au: Relationship between structure and mechanical properties. *Acta Materialia* **2015**, *99*, 29–38.

[170] Kuwano-Nakatani, S.; Fujita, T.; Uchisawa, K.; Umetsu, D.; Kase, Y.; Kowata, Y.; Chiba, K.; Tokunaga, T.; Arai, S.; Yamamoto, Y.; others Environment-sensitive thermal coarsening of nanoporous gold. *Materials Transactions* **2015**, *56*, 468–472.

[171] Stuckner, J.; Frei, K.; McCue, I.; Demkowicz, M. J.; Murayama, M. AQUAMI: An open source Python package and GUI for the automatic quantitative analysis of morphologically complex multiphase materials. *Computational Materials Science* **2017**, *139*, 320–329.

[172] Bapari, S.; Lührs, L.; Weissmüller, J. Metrics for the characteristic length scale in the random bicontinuous microstructure of nanoporous gold. *Acta materialia* **2023**, *260*, 119333.

[173] Hu, K.; Ziehmer, M.; Wang, K.; Lilleodden, E. T. Nanoporous gold: 3D structural analyses of representative volumes and their implications on scaling relations of mechanical behaviour. *Philosophical Magazine* **2016**, *96*, 3322–3335.

[174] Schneider, C. A.; Rasband, W. S.; Eliceiri, K. W. NIH Image to ImageJ: 25 years of image analysis. *Nature methods* **2012**, *9*, 671–675.

[175] Ostu, N. A threshold selection method from gray-level histograms. *IEEE Trans SMC* **1979**, *9*, 62.

[176] Doube, M.; Kłosowski, M. M.; Arganda-Carreras, I.; Cordelières, F. P.; Dougherty, R. P.; Jackson, J. S.; Schmid, B.; Hutchinson, J. R.; Shefelbine, S. J. BoneJ: free and extensible bone image analysis in ImageJ. *Bone* **2010**, *47*, 1076–1079.

[177] Odgaard, A.; Gundersen, H. Quantification of connectivity in cancellous bone, with special emphasis on 3-D reconstructions. *Bone* **1993**, *14*, 173–182.

[178] Toriwaki, J.; Yonekura, T. Euler number and connectivity indexes of a three dimensional digital picture. *Forma-Tokyo-* **2002**, *17*, 183–209.

[179] Lazanas, A. C.; Prodromidis, M. I. Electrochemical impedance spectroscopy- a tutorial. *ACS Measurement Science Au* **2023**, *3*, 162–193.

[180] Duncan, H.; Lasia, A. Mechanism of hydrogen adsorption/absorption at thin Pd layers on Au (1 1 1). *Electrochimica acta* **2007**, *52*, 6195–6205.

[181] Stenzel, O.; others *The physics of thin film optical spectra*; Springer, 2015; Vol. 366.

[182] Wang, S.; Zhang, J.; Gharbi, O.; Vivier, V.; Gao, M.; Orazem, M. E. Electrochemical impedance spectroscopy. *Nature Reviews Methods Primers* **2021**, *1*, 41.

[183] Richert, C. Data-based analysis of nanoporous metals: from microstructural features to structure-property relationships. Ph.D. thesis, 2023.

[184] Sohn, S.; Richert, C.; Shi, S.; Weissmüller, J.; Huber, N. Scaling between elasticity and topological genus for random network nanomaterials. *Extreme Mechanics Letters* **2024**, *68*, 102147.

[185] Miller, R. E.; Shenoy, V. B. Size-dependent elastic properties of nanosized structural elements. *Nanotechnology* **2000**, *11*, 139–147.

[186] Mathesan, S.; Mordehai, D. Size-dependent elastic modulus of nanoporous Au nanopillars. *Acta Materialia* **2020**, *185*, 441–452.

[187] Elsner, B. A. M.; Müller, S.; Bargmann, S.; Weissmüller, J. Surface excess elasticity of gold: Ab initio coefficients and impact on the effective elastic response of nanowires. *Acta Materialia* **2017**, *124*, 468–477.

[188] Richert, C.; Odermatt, A.; Huber, N. Computation of Thickness and Mechanical Properties of Interconnected Structures: Accuracy, Deviations, and Approaches for Correction. *Frontiers in Materials* **2019**, *6*.

[189] Biener, J.; Hodge, A. M.; Hamza, A. V.; Hsiung, L. M.; Satcher Jr, J. H. Nanoporous Au: A high yield strength material. *Journal of applied physics* **2005**, *97*, 024301.

[190] Bürckert, M.; Briot, N. J.; Balk, T. J. Uniaxial compression testing of bulk nanoporous gold. *Philosophical Magazine* **2017**, *97*, 1157–1178.

[191] Balk, T. J.; Eberl, C.; Sun, Y.; Hemker, K. J.; Gianola, D. S. Tensile and compressive microspecimen testing of bulk nanoporous gold. *Jom* **2009**, *61*, 26–31.

[192] Jeon, H.; Kang, N.-R.; Gwak, E.-J.; Jang, J.-i.; Han, H. N.; Hwang, J. Y.; Lee, S.; Kim, J.-Y. Self-similarity in the structure of coarsened nanoporous gold. *Scripta Materialia* **2017**, *137*, 46–49.

[193] Li, Y.; Dinh Ngô, B.-N.; Markmann, J.; Weissmüller, J. Datasets for the microstructure of nanoscale metal network structures and for its evolution during coarsening. *Data in Brief* **2020**, *29*, 105030.

[194] Grundner, M.; Halbritter, J. XPS and AES studies on oxide growth and oxide coatings on niobium. *Journal of Applied Physics* **1980**, *51*, 397–405.

[195] Ross, R. B. *Metallic materials specification handbook*; Springer Science & Business Media, 2013.

[196] Trasatti, S.; Petrii, O. Real surface area measurements in electrochemistry. *Journal of electroanalytical chemistry* **1992**, *327*, 353–376.

[197] Rezaei, B.; Havakeshian, E.; Ensafi, A. A. Fabrication of a porous Pd film on nanoporous stainless steel using galvanic replacement as a novel electrocatalyst/electrode design for glycerol oxidation. *Electrochimica Acta* **2014**, *136*, 89–96.

[198] Mann, H. B.; Whitney, D. R. On a test of whether one of two random variables is stochastically larger than the other. *The annals of mathematical statistics* **1947**, 50–60.

[199] Viswanath, R.; Weissmüller, J. Electrocapillary coupling coefficients for hydrogen electrosorption on palladium. *Acta materialia* **2013**, *61*, 6301–6309.

[200] Boukamp, B. A. A nonlinear least squares fit procedure for analysis of immittance data of electrochemical systems. *Solid state ionics* **1986**, *20*, 31–44.

[201] Jacobsen, A. J.; Barvosa-Carter, W.; Nutt, S. Micro-scale Truss Structures formed from Self-Propagating Photopolymer Waveguides. *Advanced Materials* **2007**, *19*, 3892–3896.

[202] Kadic, M.; Bückmann, T.; Stenger, N.; Thiel, M.; Wegener, M. On the practicability of pentamode mechanical metamaterials. *Applied Physics Letters* **2012**, *100*, 191901.

[203] Tancogne-Dejean, T.; Spierings, A. B.; Mohr, D. Additively-manufactured metallic micro-lattice materials for high specific energy absorption under static and dynamic loading. *Acta Materialia* **2016**, *116*, 14–28.

[204] Richert, C.; Huber, N. Skeletonization, geometrical analysis, and finite element modeling of nanoporous gold based on 3D tomography data. *Metals* **2018**, *8*, 282.

[205] Richert, C.; Huber, N. A comparison of ligament geometries in real and computer-generated nanoporous gold based on cross-section descriptors. *Computational Materials Science* **2023**, *229*, 112423.

[206] Stukowski, A. Computational analysis methods in atomistic modeling of crystals. *Jom* **2014**, *66*, 399–407.

[207] Joo, S.-H.; Jeong, Y.; Wada, T.; Okulov, I.; Kato, H. Inhomogeneous dealloying kinetics along grain boundaries during liquid metal dealloying. *Journal of Materials Science & Technology* **2022**, *106*, 41–48.

[208] Ye, X.-L.; Lu, N.; Li, X.-J.; Du, K.; Tan, J.; Jin, H.-J. Primary and Secondary Dealloying of Au(Pt)-Ag: Structural and Compositional Evolutions, and Volume Shrinkage. *Journal of The Electrochemical Society* **2014**, *161*, C517–C526.

[209] Li, Y.; Ngo-Dinh, B.-N.; Markmann, J.; Weissmüller, J. Evolution of length scales and of chemical heterogeneity during primary and secondary dealloying. *Acta Materialia* **2022**, *222*, 117424.

[210] Shi, S.; Markmann, J.; Weissmüller, J. Synthesis of uniform bulk nanoporous palladium with tunable structure. *Electrochimica Acta* **2018**, *285*, 60–69.

[211] Lai, L.; Gaskey, B.; Chuang, A.; Erlebacher, J.; Karma, A. Topological control of liquid-metal-dealloyed structures. *Nature communications* **2022**, *13*, 1–10.

[212] Elsner, B. A.; Müller, S.; Bargmann, S.; Weissmüller, J. Surface excess elasticity of gold: Ab initio coefficients and impact on the effective elastic response of nanowires. *Acta Materialia* **2017**, *124*, 468–477.

[213] Zou, L.; Shao, J.-C.; Jin, H.-J. Ligament morphology and elastic modulus of porous structure formed by liquid metal dealloying. *Journal of Materials Research and Technology* **2024**, *31*, 3914–3920.

[214] Ziehmer, M.; Lilleodden, E. T. The isothermal evolution of nanoporous gold from the ring perspective - an application of graph theory. *Acta Materialia* **2020**,

[215] Delheusy, M.; Stierle, A.; Kasper, N.; Kurta, R.; Vlad, A.; Dosch, H.; Antoine, C.; Resta, A.; Lundgren, E.; Andersen, J. X-ray investigation of subsurface interstitial oxygen at Nb/oxide interfaces. *Applied Physics Letters* **2008**, *92*.

[216] Lemier, C.; Weissmüller, J. Grain boundary segregation, stress and stretch: Effects on hydrogen absorption in nanocrystalline palladium. *Acta materialia* **2007**, *55*, 1241–1254.

[217] Grahame, D. C. The electrical double layer and the theory of electrocapillarity. *Chemical reviews* **1947**, *41*, 441–501.

[218] Riedel, L.; Markmann, J.; Weissmüller, J.; Shi, S. Tailoring hierarchical nanoporous gold on dual length scales. *Physical Review Materials* **2023**, *7*, 116001.

[219] Rice, C. L.; Whitehead, R. Electrokinetic flow in a narrow cylindrical capillary. *The Journal of Physical Chemistry* **1965**, *69*, 4017–4024.

[220] Shi, S.; Markmann, J.; Weissmüller, J. Verifying Larché–Cahn elasticity, a milestone of 20th-century thermodynamics. *Proceedings of the National Academy of Sciences* **2018**, *115*, 10914–10919.

[221] Oldenburger, M.; Beduerftig, B.; Gruhle, A.; Grimsmann, F.; Richter, E.; Findeisen, R.; Hintennach, A. Investigation of the low frequency Warburg impedance of Li-ion cells by frequency domain measurements. *Journal of Energy Storage* **2019**, *21*, 272–280.

[222] Wang, J. Realizations of generalized Warburg impedance with RC ladder networks and transmission lines. *Journal of the Electrochemical Society* **1987**, *134*, 1915.

[223] Bisquert, J. Influence of the boundaries in the impedance of porous film electrodes. *Physical Chemistry Chemical Physics* **2000**, *2*, 4185–4192.

[224] Sluyters-Rehbach, M. Impedances of electrochemical systems: Terminology, nomenclature and representation-Part I: Cells with metal electrodes and liquid solutions (IUPAC Recommendations 1994). *Pure and applied chemistry* **1994**, *66*, 1831–1891.

[225] Breiter, M. Dissolution and adsorption of hydrogen at smooth Pd wires at potentials of the alpha phase in sulfuric acid solution. *Journal of Electroanalytical Chemistry and Interfacial Electrochemistry* **1977**, *81*, 275–284.

[226] Fang, L.-l.; Tao, Q.; Li, M.-f.; Liao, L.-w.; Chen, D.; Chen, Y.-x. Determination of the real surface area of palladium electrode. *Chinese Journal of Chemical Physics* **2010**, *23*, 543–548.

[227] Gubanova, E.; Schmidt, T. O.; Watzele, S.; Alexandrov, V.; Bandarenka, A. S. Structure-dependent electrical double-layer capacitances of the basal plane Pd (hkl) electrodes in HClO4. *The Journal of Physical Chemistry C* **2022**, *126*, 11414–11420.

[228] Conway, B.; Bai, L. State of adsorption and coverage by overpotential-deposited H in the H2 evolution reaction at Au and Pt. *Electrochimica Acta* **1986**, *31*, 1013–1024.

[229] Agmon, N. The grotthuss mechanism. *Chemical Physics Letters* **1995**, *244*, 456–462.

[230] Alefeld, G.; Völkl, J. Hydrogen in metals I-Basic properties. *Berlin and New York* **1978**, *28*.

[231] Völkl, J.; Wollenweber, G.; Klatt, K.-H.; Alefeld, G. Reversed isotope dependence for hydrogen diffusion in palladium. *Zeitschrift für Naturforschung A* **1971**, *26*, 922–923.

[232] Cattarin, S.; Kramer, D.; Lui, A.; Musiani, M. M. Preparation and characterization of gold nanostructures of controlled dimension by electrochemical techniques. *The Journal of Physical Chemistry C* **2007**, *111*, 12643–12649.

[233] Zhong, Y.; Markmann, J.; Jin, H.-J.; Ivanisenko, Y.; Kurmanaeva, L.; Weissmüller, J. Crack Mitigation during Dealloying of Au25 C u75. *Advanced Engineering Materials* **2014**, *16*, 389–398.

[234] Deng, Q.; Smetanin, M.; Weissmüller, J. Mechanical modulation of reaction rates in electrocatalysis. *Journal of catalysis* **2014**, *309*, 351–361.

[235] Viswanath, R.; Kramer, D.; Weissmüller, J. Adsorbate effects on the surface stress–charge response of platinum electrodes. *Electrochimica Acta* **2008**, *53*, 2757–2767.

[236] Weissmüller, J. Coherent Phase Change in Interstitial Solutions: A Hierarchy of Instabilities. *Advanced Science* **2024**, 2308554.

[237] Montella, C. Comments on the review 'Anomalous behaviour of hydrogen extraction from hydride-forming metals and alloys under impermeable boundary conditions', by J.-W. Lee, S.-I. Pyun, Electrochim. Acta 50 (2005) 1777–1805. *Electrochimica acta* **2005**, *51*, 361–373.

[238] Montella, C. Discussion of the potential step method for the determination of the diffusion coefficients of guest species in host materials: Part I. Influence of charge transfer kinetics and ohmic potential drop. *Journal of Electroanalytical Chemistry* **2002**, *518*, 61–83.

[239] Loiseau, A. The role of interfaces and domain boundaries in order—7disorder transitions. *Current Opinion in Solid State and Materials Science* **1996**, *1*, 369–377.

[240] Cahn, J. W.; Hilliard, J. E. Free energy of a nonuniform system. I. Interfacial free energy. *The Journal of chemical physics* **1958**, *28*, 258–267.

[241] Li, Y.; Weissmüller, J. Size-dependent phase change in energy storage materials: Comparing the impact of solid-state wetting and of coherency stress. *The Journal of Chemical Physics* **2025**, *162*.

[242] Benck, J. D.; Jackson, A.; Young, D.; Rettenwander, D.; Chiang, Y.-M. Producing high concentrations of hydrogen in palladium via electrochemical insertion from aqueous and solid electrolytes. *Chemistry of Materials* **2019**, *31*, 4234–4245.

[243] Wang, Q.; Zhang, S.; Guo, J.; Chen, P. Advances in highly hydrided palladium. *Frontiers in Materials* **2024**, *11*, 1365526.

[244] Switendick, A. Metal hydrides—structure and band structure. *International Journal of Quantum Chemistry* **1971**, *5*, 459–470.

[245] Li, G.; Kobayashi, H.; Dekura, S.; Ikeda, R.; Kubota, Y.; Kato, K.; Takata, M.; Yamamoto, T.; Matsumura, S.; Kitagawa, H. Shape-dependent hydrogen-storage properties in Pd nanocrystals: which does hydrogen prefer, octahedron (111) or cube (100)? *Journal of the American Chemical Society* **2014**, *136*, 10222–10225.